Erbacher, J., Mosher, D.C., Malone, M.J., et al., 2004
Proceedings of the Ocean Drilling Program, Initial Reports Volume 207

4. SITE 1257[1]

Shipboard Scientific Party[2]

BACKGROUND AND OBJECTIVES

Site 1257 is located at 2951 meters below sea level (mbsl) on a terrace above the steep northern slope (>10°) of northwest Demerara Rise, which is ~400 km north of Suriname. As the second deepest location of the cruise, Site 1257 serves as an intermediate member of the paleoceanographic depth transect across Demerara Rise. It was promoted to recore Deep Sea Drilling Project (DSDP) Site 144, which was spot cored during Leg 144 in 1970. The major objectives were the following:

1. Core and log an Albian–Oligocene section to evaluate paleoceanographic and paleoclimatic changes during the Paleogene and Cretaceous, with an emphasis on major and abrupt events during this interval (e.g., the Eocene/Oligocene [E/O] boundary, the Paleocene/Eocene [P/E] boundary, and the Cretaceous oceanic anoxic events [OAEs]).
2. Reconstruct the history of the opening of the Equatorial Atlantic Gateway by obtaining benthic foraminifer proxy data. These data will help us to understand changes in bottom water circulation over Demerara Rise during the gradual opening of the seaway.
3. Define the depth of key seismic reflectors in the seismic stratigraphy compilation in order to create a detailed drilling and sampling plan for the remaining sites along the Demerara Rise depth transect.

The steep northwestern slope indicated in Figure F1 of Demerara Rise, where Site 1257 is located, is part of the southern transform fault that separated South America and West Africa during the rift phase of the southern central Atlantic in the Late Jurassic–Early Cretaceous. Al-

F1. Seismic reflection line M49-4, p. 38.

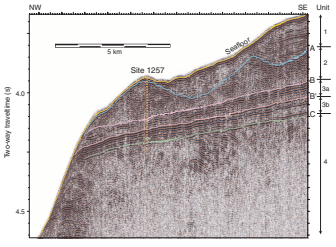

[1]Examples of how to reference the whole or part of this volume.
[2]Shipboard Scientific Party addresses.

Ms 207IR-104

though spot cored, results from Site 144 demonstrated the potential for the presence of all the target sediments.

Seismic Stratigraphy

The seismic stratigraphy of Site 1257 is demonstrated in Figure F1. Within 2.5 km northwest and 1.5 km north-northeast of the drill site, the seafloor begins to fall off at a 10° angle, from the site elevation of 2951 mbsl to 4400 mbsl on the abyssal plain. The site itself is on a slight mound that appears to be an erosional remnant. Reflector "A," representing the top of this erosional unconformity, crops out at the seafloor at the site (within the resolution of the survey data). Between Reflector A (the seafloor in this case) and Reflector "B" is seismic Unit 2; seismic Unit 1 is missing from this site. Unit 2 is 173 ms thick (144 m two-way traveltime) at this location using checkshot and downhole logging velocity information (see "Downhole Logging," p. 29). Seismic Unit 2 shows an incoherent reflection character here, describing a disturbed sediment package or the effect of side echoes from local complex topography. A high-amplitude reflection event of short lateral duration occurs at 110 ms subbottom (90 meters below seafloor [mbsf]) at the site.

Reflector B at 173 ms subbottom (144 mbsf) marks the top of seismic Unit 3. It is a flat-lying sequence at this site that dips gently to the northeast at an angle of 1.7°. Reflector B is hummocky on a local scale, probably cut by channels, and is underlain by several high-amplitude reflections and then a short transparent zone to the top of Reflector "B'" at 217 ms subbottom (181 mbsf). This section is described as Subunit 3a in "Seismic Unit 3," p. 3, in Shipboard Scientific Party ["Site Survey and Underway Geophysics"], this volume. Subunit 3b underlies Subunit 3a and is the sequence between Reflector B′ and the Reflector "C," which occurs at 272 ms subbottom (232 mbsf).

Most acoustic energy is lost below Reflector C in the survey data, and the section is difficult to describe. A few hyperbolic reflections in this interval are visible. Industry line C2206 crosses in a northeast–southwest direction just 1 km northeast of the drill site (Fig. F1, p. 5, in Shipboard Scientific Party ["Site Survey and Underway Geophysics"], this volume). In this profile, the sequence of reflectors below Horizon C appears folded into a possible small anticline below the drill site and contacts Reflector C as an angular unconformity.

OPERATIONS

Leg 207 officially began with the first line ashore at Bridgetown, Barbados, at 2255 hr on 11 January 2003. After two days of port call activities, the last line was released and the ship maneuvered into the harbor.

Transit to Site 1257

The transit to the Leg 207 operational area was uneventful, and at 0730 hr on 15 January, the ship's speed was reduced in preparation for a short seismic survey to produce a crossing line at Site 1258 (see "*JOIDES Resolution* Underway Geophysics (Leg 207)," p. 2, in Shipboard Scientific Party ["Site Survey and Underway Geophysics"], this volume). The survey was completed by 1200 hr, and we proceeded to Site 1257. Upon arriving at the coordinates for the site, the thrusters

and hydrophones were lowered, followed by deployment of a positioning beacon at 1533 hr on 15 January, which initiated operations at Site 1257.

Hole 1257A

Once the ship settled on location, an advanced piston corer (APC)/extended core barrel (XCB) bottom-hole assembly (BHA) was constructed and tripped close to the seafloor. With the bit positioned at 2955 meters below rig floor (mbrf), the first APC core recovered 2.59 m of sediment. Based on the recovery in this mudline core, the water depth was calculated to be 2961.9 mbrf (2951.0 mbsl). Beginning with Core 3H, APC cores were oriented. Core 3H also initiated the deployment of the APC temperature (APCT) tool. APC coring continued through Core 5H to 40.6 mbsf (recovery = 104%), where APC coring was terminated because excessive overpull forces (up to 140,000 lb) were required to extract the last three cores. After recovery of Core 5H, it was discovered that one of the three 10-ft APC nonmagnetic core barrel sections was bent. With no replacement nonmagnetic APC core barrels on board, a standard steel barrel assembly was placed in service and alternated with the other remaining nonmagnetic core barrels thereafter.

Coring continued with the XCB from 40.6 to 284.7 mbsf (recovery = 71.1%) and was terminated when the target depth was reached. Much of the lower part of the cored interval was penetrated at a slower than anticipated rate of ~10 m/hr. Core 21X (179.0–188.6 mbsf) recovered 1.22 m of black shale with a strong petroliferous odor, which registered 15 ppm using the handheld H_2S gas detectors. The cutting shoe used to recover Core 21X was twisted and discolored from friction-induced heating and probably contributed to the strong odor from the organic-rich sediment. No similar concerns were encountered during subsequent coring.

At 0930 hr on 18 January, with the target depth reached in Hole 1257A (Table T1), coring operations ceased and the hole was prepared for logging with a 30-bbl sepiolite mud sweep and a wiper trip. The wiper trip indicated that the hole was in excellent condition, with only 1 m of fill on bottom. The hole was displaced with another 125 bbl of mud, and the bit was positioned at 82 mbsf for logging.

T1. Coring summary, p. 78.

The first logging run was made with the triple combination (triple combo) tool string (see "Downhole Logging," p. 29, for details on the individual sensors on the logging tools), which was deployed to ~284 mbsf and logged to the seafloor (the upper 60 mbsf through the pipe) in two passes. The second logging run included two passes with the Formation MicroScanner (FMS)-sonic tool string from 284 mbsf to the base of the drill string at 60 mbsf. The third and final logging run was made with the Well Seismic Tool (WST) from 284 to 60 mbsf, recording clean data at eight stations. After completion of the logging operations, the drill string was retrieved, clearing the rig floor at 2245 hr on 19 January and ending Hole 1257A.

Hole 1257B

The ship was offset 30 m southeast of Hole 1257A, and a rotary core barrel (RCB) BHA with a center bit assembly was deployed. Hole 1257B was spudded at 0630 hr on 19 January and drilled to 40 mbsf. The center bit was retrieved, an RCB core barrel deployed, and coring advanced

to 227.3 mbsf, taking 27 cores (recovery = 62.1%) (Table T1). The hole was terminated when the depth objectives were reached. After filling the hole with sepiolite mud, the drill string was pulled out of the hole, ending Hole 1257B at 1320 hr on 21 January.

Hole 1257C

The ship was offset another 30 m to the southeast, and Hole 1257C was spudded with the center bit in place at 1415 hr on 21 January. The hole was advanced to 82 mbsf, and the center bit was retrieved. With the RCB, coring deepened the hole to 235.9 mbsf, taking 16 cores (recovery = 62.8%) (Table T1). With the depth objective met, the hole was filled with sepiolite mud and the drill string was retracted, clearing the rotary table at 1530 hr on 22 January and ending operations at Site 1257. After recovery of the beacon and retraction of the thrusters and hydrophones, the ship began the transit to Site 1258.

LITHOSTRATIGRAPHY

Site 1257 is a reoccupation of DSDP Site 144 and represents an intermediate-depth site (current water depth = 2951 mbsl) of the Leg 207 Demerara Rise depth transect. Among the three holes at Site 1257, we recovered >90% of the ~285 m drilled—a far more complete sample of the stratigraphic record at this site than recovered in earlier drilling (Fig. F2).

Five lithostratigraphic units were recognized at Site 1257 (Table T2). The oldest unit recovered (Unit V) is dominated by calcareous silty claystones to clayey calcareous siltstones. The superjacent unit (Unit IV) is composed dominantly of laminated, organic-rich calcareous claystones and laminated limestone. The youngest three units (Units I–III) recognized are pelagic and dominantly composed of calcareous microfossils, siliceous microfossils, and clay. These pelagic sediments are pervasively bioturbated; pyrite and other iron sulfides are found throughout the pelagic interval but are most abundant in Unit III. Clay and zeolite are also relatively abundant in Unit III, whereas Unit II contains a relatively high abundance of siliceous microfossils. Unit I is carbonate poor. Sediments and sedimentary rocks recovered at Site 1257 range in age from Albian to Miocene (see "Biostratigraphy," p. 11), but the record is interrupted by at least eight hiatuses and/or mass flow deposits.

Lithostratigraphic units recognized at Site 1257 generally parallel those reported for Site 144 (Hayes, Pimm, et al., 1972). There is an offset between unit numbers herein and those used at Site 144 because we recognized a thin upper unit that was not recovered during earlier drilling (Fig. F2). Most other differences between the lithostratigraphic divisions at Sites 144 and 1257 represent differences in the level at which unit boundaries were placed and can be attributed to uncertainty regarding the lithologies in coring gaps at Site 144. However, we recognized an increase in clay and zeolite content (the Unit II–III transition herein) higher in the section than the Unit I/II division at Site 144. Finally, we apparently did not penetrate the lowest unit drilled at Site 144.

F2. Comparison Sites 144 and 1257, p. 39.

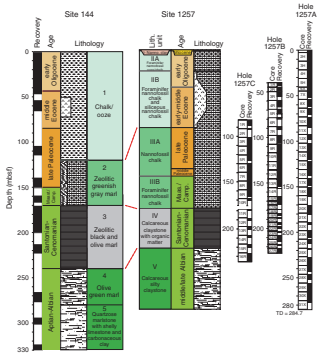

T2. Summary of lithology, p. 80.

Lithostratigraphic Units

Unit I

Interval: 207-1257A-1H-1, 0 cm, through 1H-2, 7 cm
Depth: 0.00–1.57 mbsf
Thickness: 1.57 m
Age: late Neogene
Lithology: nannofossil clay

Unit I is predominantly a nannofossil clay that exhibits a gradual change downhole from pale brown to pale olive (Fig. F3). The unit was only recovered in Hole 1257A. It is burrow mottled, and iron sulfide is present both in discrete burrows and as isolated blebs throughout the unit. The base of Unit I is placed at a sharp color change from pale olive to pale yellow.

F3. Lithologies from Units I and II, p. 40.

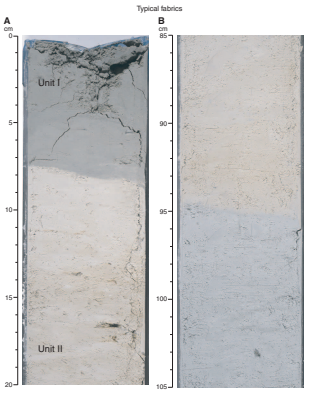

Unit II

Intervals: 207-1257A-1H-1, 7 cm, through 10X-3, 55 cm; 207-1257B-1R-1, 0 cm, though 6R-1, 0 cm; and 207-1257C-1R-1, 0 cm, through 1R-3, 95 cm
Depths: Hole 1257A: 1.57–76.85 mbsf; Hole 1257B: <40.00–78.70 mbsf; and Hole 1257C: <82.00–85.95 mbsf
Thickness: 75.28 m
Age: early Oligocene–early Eocene
Lithology: nannofossil ooze with foraminifers, nannofossil chalk with foraminifers, and siliceous nannofossil chalk with foraminifers

This unit consists of light greenish gray to greenish gray chalk and ooze containing 40–80 wt% carbonate in dominant lithologies (Fig. F4). Oozes are restricted to the upper 20 m of Unit I. *Zoophycos* and *Chondrites* are found throughout. The unit is divided into two subunits based on biogenic silica content. Subunit IIA contains only traces of radiolarians, whereas siliceous microfossils make up 10%–40% of material in smear slides from Subunit IIB. The upper contact of Unit II is placed at sharp color change that corresponds to an increase in carbonate content, whereas the bottom contact is gradational and corresponds to a downhole decrease in the abundance of siliceous microfossils and an increase in clay and zeolite abundance. It is placed at the base of a gravity flow deposit (Fig. F3) that falls near the P/E boundary, but recovery problems and the gradational nature of the lithologic transition makes precise correlation uncertain.

F4. Carbonate and organic carbon, p. 42.

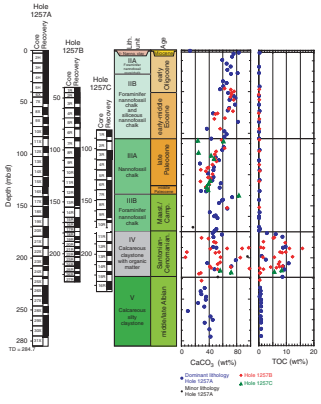

Subunit IIA

Interval: 207-1257A-1H-1, 7 cm, through 4H-2, 75 cm
Depth: 1.57–23.85 mbsf
Thickness: 22.28 m
Age: early Oligocene
Lithology: nannofossil ooze with foraminifers and nannofossil chalk with foraminifers

Subunit IIA is composed of carbonate-rich (foraminifers and nannofossils) pelagic sediments near the chalk–ooze transition; these lithologies alternate on a 10- to 20-cm scale through most of Subunit IIA. The top of this subunit is placed at a sharp color change from pale olive to

pale yellow at 1.57 mbsf (Hole 1257A). The color change coincides with an increase in carbonate content from 15 to 80 wt% and an increase in the degree of induration. There is also a sharp color change from pale yellow to greenish gray at 5.05 mbsf in Hole 1257A. However, neither sediment composition nor sediment fabric changes noticeably at this boundary and it is interpreted as a late diagenetic redox boundary that propagated down from the seafloor. Below this color change, the sediments are light greenish gray with only subtle variations. Dark bands are present (e.g., Sample 207-1257A-3H-4, 58–60 cm [17.13–17.15 mbsf]) and are often associated with burrows. These bands are interpreted as redox boundaries or other chemical gradients from early diagenesis. Black mottles, streaks, and blebs are found throughout the unit and are often concentrated in burrows. Sediments range from homogeneous to burrow mottled, and the number of discrete traces increases downhole. The base of Subunit IIA is placed at the first consistent downhole occurrence of siliceous microfossils.

Subunit IIB

Intervals: 207-1257A-4H-2, 75 cm, through 10X-3, 55 cm; 207-1257B-1R-1, 0 cm, through 6R-1, 0 cm; and 207-1257C-1R-1, 0 cm, through 1R-3, 95 cm
Depths: Hole 1257A: 23.85–76.85 mbsf; Hole 1257B: <40.00–78.70 mbsf; and Hole 1257C: <82.00–85.95 mbsf
Thickness: 53.00 m
Age: early Oligocene–early Eocene
Lithology: siliceous nannofossil chalk with foraminifers to nannofossil chalk with siliceous microfossils and foraminifers

Subunit IIB is composed of a carbonate-rich (foraminifers and nannofossils) chalk containing common to abundant siliceous microfossils. Most of the subunit is pelagic, but there are at least four ~1-m-thick gravity flow deposits (Fig. **F3C**). Both the top and the bottom contacts of Subunit IIB are gradational. The top of the subunit is placed at the first consistent downhole occurrence of siliceous microfossils. Siliceous microfossils increase in abundance downhole from Sections 207-1257A-6X-1 through 9X-4 and 207-1257B-1R-1 through 4R-4 in both the dominant and minor lithologies; they compose ≤40% of material in some smear slides. Below these levels, the abundance of siliceous microfossils drops and that of zeolites and clay content increase. The boundary between Subunits IIB and III is placed at the base of a gravity flow deposit below which clay content increases (Fig. **F4**) and zeolites are more common than siliceous microfossils. The gravity flow also falls near the P/E boundary, but redeposited material and one subjacent sample (Hole 1257C) contain Eocene microfossils, demonstrating that the flow deposit is unrelated to the Paleocene/Eocene Thermal Maximum (PETM).

As in Subunit IIA, the color of Subunit IIB varies between light greenish gray and greenish gray. Subhorizontal millimeter-scale dark green bands are present and are interpreted as early diagenetic redox fronts. Black layers, blebs, and streaks are common and seem to be associated with burrows. Bioturbation is heavy to pervasive throughout Subunit IIB. Material filling discrete burrows varies only slightly from the background lithology. Tan burrow fill contains a relatively high abundance of larger microfossils, whereas light burrow fill contains a relatively high abundance of nannofossils. Finally, in those samples checked, the material in *Zoophycos* and *Chondrites* traces contains more siliceous microfossils than material outside the burrows.

Unit III

Intervals: 207-1257A-10X-3, 55 cm, through 20X-4, 52 cm; 207-1257B-6R-1, 0 cm, through 17R-1, 17 cm; and 207-1257C-1R-3, 95 cm, through 11R-1, 3 cm
Depths: Hole 1257A: 76.85–174.50 mbsf; Hole 1257B: 78.70–174.40 mbsf; and Hole 1257C: 85.95–178.00 mbsf
Thickness: 97.65 m
Age: late Paleocene–early Campanian
Lithology: nannofossil chalk and foraminifer nannofossil chalk

This unit is mainly composed of nannofossil chalk with variable amounts of planktonic foraminifers and clay. Zeolite is common in the deposits, and siliceous microfossils are rare to absent. The upper contact is placed at the base of a gravity flow deposit at the P/E contact, which approximates the level below which clay content increases and zeolites are more common than siliceous microfossils (see **"Site 1257 Smear Slides"**). The base of Unit III is placed at the upper surface of a 5-cm-thick laminated limestone that overlies the organic-rich claystones and siltstones of Unit IV. Unit III is subdivided into two subunits based on differences in the abundance of foraminifers and carbonate content. The contact is placed at the level of a slump that coincides with a hiatus that represents much of the Maastrichtian and Paleocene.

Subunit IIIA

Intervals: 207-1257A-10X-3, 55 cm, through 16X-CC, 60 cm; 207-1257B-6R-1, 0 cm, through 12R-7, 60 cm; and 207-1257C-1R-3, 95 cm, through 7R-5, 15 cm
Depths: Hole 1257A: 76.85–140.70 mbsf; Hole 1257B: 78.70–145.50 mbsf; and Hole 1257C: 85.95–145.15
Thickness: 66.8 m
Age: late Paleocene–middle Paleocene
Lithology: nannofossil chalk and redeposited nannofossil chalk and limestone

Subunit IIIA mainly consists of light greenish gray to greenish gray mottled to homogeneous nannofossil chalk (Fig. **F5**). Carbonate content generally ranges between 30 and 50 wt% (Fig. **F4**). The carbonate fraction is dominated by nannofossils, with planktonic foraminifers representing a relatively minor component. Zeolites are consistently present, and siliceous microfossils (radiolarians and sponge spicules) were observed only near the contact with Unit II. Fish debris was observed in trace amounts in several samples.

The P/E boundary falls in the upper portion of Subunit IIIA. It is constrained to within a ~2.5-m interval in Sections 207-1257C-1R-3, 125 cm, through 1R-CC (see **"Biostratigraphy,"** p. 11). A 3-cm-thick green clay layer in Sample 207-1257C-1R-5, 48–51 cm, is the most likely candidate for a lithologic expression of events at the boundary. Unfortunately, this interval was not recovered in Holes 1257A or 1257B. Further, although a mottled fabric is still apparent, drilling disturbance seems to have shattered the rocks below the putative boundary. Otherwise, burrow mottling is present throughout Subunit IIIA and discrete traces assigned to *Zoophycos* and *Chondrites* are common. Most discrete traces are darker than surrounding sediments, but lighter white and tan traces are also present. A high abundance of *Chondrites* and *Zoophycos*

F5. Lithology of pelagic sediments in Unit III, p. 43.

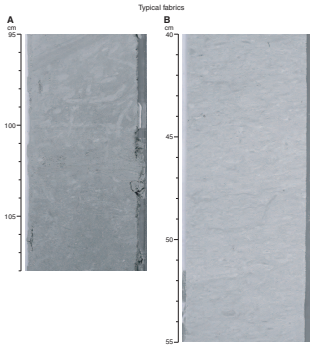

traces filled with darker material is seen in Cores 207-1257A-14X and 207-1257B-11R.

The upper contact of Subunit IIIA is gradational and is placed at the base of a slump (Fig. F3) that approximates the level where the abundance of siliceous microfossils decreases and zeolites appear in smear slides. The lower contact of Subunit IIIA is placed at the base of a gravity flow deposit in Hole 1257A that corresponds to the contact between early Maastrichtian and middle Paleocene deposits (Fig. F5). The latter deposit is clast supported and contains angular pieces of greenish gray chalk and white limestone up to 75 cm across. The clasts exhibit internal burrowing, but no burrows seem to penetrate matrix and clasts in the deposit. The clasts and matrix examined in this interval contain Paleocene microfossils, as does the superjacent pelagic chalk. Pelagic chalk below the slump, on the other hand, contains only Cretaceous fossils (see "Biostratigraphy," p. 11).

Subunit IIIB

Intervals: 207-1257A-16X-CC, 60 cm, through 20X-4, 52 cm; 207-1257B-12R-7, 60 cm, through 17R-1, 17 cm; and 207-1257C-7R-5, 15 cm, through 11R-1, 3 cm
Depths: Hole 1257A: 140.70–174.50 mbsf; Hole 1257B: 145.50–174.40 mbsf; and Hole 1257C: 145.15–178.00 mbsf
Thickness: 33.8 m
Age: early Maastrichtian–early Campanian
Lithology: foraminifer nannofossil chalk

Subunit IIIB mainly consists of light greenish gray to greenish gray nannofossil chalk, with carbonate content ranging from 40 to 60 wt% (Fig. F4). The top of Subunit IIIB is placed at the base of the gravity flow deposit containing Tertiary microfossils that rests unconformably on early Maastrichtian rocks. The base of Subunit IIIB is placed at the upper surface of a 55-cm-thick laminated limestone that overlies the organic-rich claystones and siltstones of Unit IV. The basal contact of Unit III is sharp, and the limestone is included in Unit IV because it is laminated.

Subunit IIIB is similar to Subunit IIIA, but is, on average, more carbonate rich and contains more foraminifers. Bioturbation is pervasive throughout and varies between darker intervals with a subhorizontal fabric dominated by *Zoophycos* and lighter intervals with a more uniform and subtle mottling. The lowest meter of Subunit IIIB (Sections 207-1257A-20X-3, 75 cm, through 20X-4, 52 cm, and 207-1257C-10R-CC) is rich in glauconite. The abundances of both foraminifers and nannofossils decrease in the lower portions of Subunit IIIB. On the other hand, pyrite, both disseminated and concentrated in burrows, increases in abundance in the lower portions of Subunit IIIB. On shorter length scales, changes in pyrite abundance seem to be correlated with changes in the style of bioturbation. Pyrite is most abundant in darker intervals with subhorizontal burrows and less abundant in lighter intervals that are pervasively mottled. Alterations on a 20- to 30-cm scale between these two fabrics occur throughout. Siliceous microfossils are absent except in the middle part of the subunit.

Unit IV

Intervals: 207-1257A-20X-4, 52 cm, through 26X-1, 0 cm; 207-1257B-17R-1, 17 cm, through 25R-2, 112 cm; and 207-1257C-11R-1, 3 cm, through 15R-CC, 39 cm

Depths: Hole 1257A: 174.50–226.80 mbsf; Hole 1257B: 174.40–217.60 mbsf; and Hole 1257C: 178.00–226.20 mbsf
Thickness: 52.3 m
Age: Santonian–middle Cenomanian
Lithology: calcareous claystone with organic matter, clayey chalk with organic matter, and limestone

Unit IV primarily consists of dark olive-gray to black (5Y 3/2 to 5Y 3/2) finely laminated calcareous claystone with organic matter and clayey chalk with organic matter (Fig. F4). The unit shows well-developed submillimeter-scale laminations and has a strong petroliferous odor. There are decimeter-scale rhythmic color variations between dark olive gray and black throughout (Fig. F6A). Carbonate content ranges from 40 to 60 wt% in dominant lithologies and as high as 78 wt% in individual carbonate-rich layers (Fig. F4). Carbonate constituents include nannofossils, foraminifers, and shell fragments. Total organic carbon (TOC) ranges from 1.5 to 15.7 wt% in dominant lithologies. Rock-Eval pyrolysis analyses indicate Type II organic matter, which is consistent with a marine origin. Sample 207-1257C-14R-1, 33 cm, contains fish scales. Inoceramids and other macrofossils are present, especially in lighter-colored intervals. Olive (5Y 4/2) laminated limestone up to 30 cm in thickness, gray (5Y 5/1) and black (N2) chert nodules, and phosphatic and calcareous nodules with foraminifers and nannofossils occur in minor amounts. The phosphatic and calcareous nodules are seen as millimeter- to centimeter-scale white blebs on core surfaces.

F6. Lithologies of Units IV and V, p. 45.

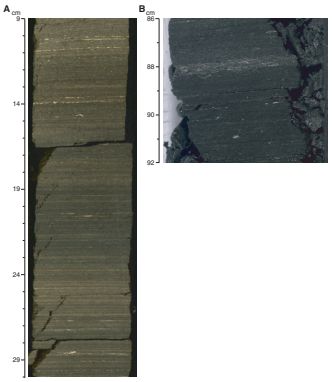

Unit V

Intervals: 207-1257A-26X-1, 0 cm, through 31X-CC, 57 cm; 207-1257B-25R-2, 112 cm, through 27R-CC, 22 cm; and 207-1257C-15R-CC, 39 cm, through 16R-CC, 18 cm
Depths: Hole 1257A: 226.80–284.70 mbsf; Hole 1257B: 217.60–227.30 mbsf; and Hole 1257C: 226.20–235.90 mbsf
Thickness: 57.90 m
Age: middle–late Albian
Lithology: silty calcareous claystone to clayey carbonate siltstone

Unit V consists of dark greenish gray (5G 4/1) silty calcareous claystone to clayey carbonate siltstone. The rocks of Unit V exhibit a discontinuous, subhorizontal wavy fabric defined by millimeter-scale calcite-rich and calcite-poor layers (Fig. F6C). This fabric is tentatively attributed to dissolution of primary carbonate, mobilization, and preferential recrystallization into more carbonate-rich intervals. Carbonate content ranges from 24 to 45 wt%, with most being undifferentiated calcite crystals in the thin undulatory layers. Quartz, shell material, pyrite nodules (Fig. F6E), and trace amounts of nannofossils are minor constituents. TOC ranges between 0.4 and 0.8 wt%. Gray calcareous sandstone intervals are found in Core 207-1257B-26R and Sections 207-1257C-15R-CC and 16R-1. Thin section analyses show subangular detrital quartz grains surrounded by sparry calcite cement. Drilling disturbance (biscuiting) is common in all holes but is pervasive in Hole 1257A.

Summary

The oldest interval recovered at Site 1257 is a unit dominated by silty calcareous claystone and clayey calcareous siltstones (Unit V) of mid-

dle–late Albian age. These rocks lie below Reflector C (see "Seismic Stratigraphy," p. 2, in "Background and Objectives"), which represents the trace of an angular unconformity on Demerara Rise, and, thus, Unit V is interpreted as a synrift depositional sequence. The lithology is quite homogeneous. Shells are common but trace fossils are rare, and no physical sedimentary structures were observed. The abundance of terrigenous material and common shells and the presence of subangular quartz sandstones in this interval suggests a relatively proximal, shallow-water setting. However, the site was apparently deep and/or sheltered enough that physical sedimentary structures were not formed. Alternatively, diagenetic overprinting may have obscured subtle depositional features. Regardless, the relatively high organic carbon content and the absence of lamination or fossil indicators of high productivity suggest high sedimentation rates.

From the late Cenomanian to Santonian, high productivity and low bottom water oxygen levels prevailed at Site 1257. This phase of deposition is recorded by the ~50 m of sediment dominated by the dark laminated calcareous claystones and laminated limestones of Unit IV. Unfortunately, the contact with Unit V was poorly recovered, but it seems to correspond to a hiatus. Organic carbon concentrations in Unit IV approach 15 wt% (Fig. F4), and abundant zeolites suggest siliceous microfossils were a common component of the sediment. Carbonate values average ~50 wt% (Fig. F4) through the interval and include nannofossils, foraminifers, shells, and carbonate debris. Despite the virtual lack of bioturbation and benthic microfossils, inoceramids are common, especially in the lower portions of the unit, attesting to this taxon's tolerance for marginal habitats. Layers of nonprismatic shells (i.e., not inoceramids) may represent other similarly tolerant taxa, brief oxygenation events, or pelagic taxa (e.g., ammonites) that lived in the overlying water column. Phosphatic lenses may represent coprolites. If this identification is correct, their high abundance, coupled with the high abundance of fish remains, suggests some combination of low sedimentation rates, high preservation potential for phosphatic material, and many fish.

Open-marine conditions and oxic bottom waters were established by the early Campanian, as indicated by the bioturbated pelagic marls of Unit III. The sharp contact between the bioturbated marls of Unit III and the laminated shales and limestones of Unit IV at Site 1257 may reflect a hiatus, but the glauconite-rich interval in the lowermost portion of Subunit IIIB is consistent with the transition being recorded by a highly condensed interval. Further, the trace fossils and abundance of pyrite may indicate that bottom waters were relatively dysoxic in the late Campanian and early Maastrichtian. However, variations in sedimentary fabric and minor sedimentary components suggest that conditions at the seafloor and/or overlying water column fluctuated on geologically short timescales.

The P/E boundary seems to be relatively complete in Hole 1257A. As noted above, a 3-cm-thick clay layer in Hole 1257C falls within an interval that contains the P/E boundary (see "Biostratigraphy," p. 11). The lack of carbonate in this layer is consistent with sedimentary changes expected at the PETM. Recovery of this boundary in Hole 1257C is fortuitous, as a gravity flow deposit is present ~2.5 m above the clay layer and the interval was not recovered in either Hole 1257A or 1257B.

Gravity flow deposits and temporal gaps are common in the pelagic record at Site 1257. In addition to the mass flow deposit above the P/E

boundary, the Cretaceous/Tertiary (K/T) and E/O boundaries are represented by hiatuses and/or gravity flow deposits. The dominance of Paleocene fossils in the matrix and clasts of the flow deposit between Cretaceous and Tertiary pelagic intervals demonstrates that this deposit is not a direct manifestation of events occurring at the K/T boundary. At least five other mass flow deposits were recognized at Site 1257. The apparent instability of the slope may reflect local conditions related to the steep topography and its position near the edge of Demerara Rise. Recovery of more complete sections at other Demerara Rise sites would support the interpretation that failures at Site 1257 are local features.

BIOSTRATIGRAPHY

In the three holes at Site 1257, we recovered primarily Paleogene–mid-Cretaceous marine sediments that contain calcareous nannofossils, planktonic foraminifers, and radiolarians in abundances and states of preservation that vary widely with lithology and sediment induration. Shipboard examination of these microfossil groups in core catcher samples, supplemented as necessary by additional samples from the cores, permitted zonal or stage assignments to be made for the entire sequence. Datum levels are summarized in Figure **F7** and in Tables **T3, T4, T5, T6, T7,** and **T8.**

A veneer of Pleistocene and upper Miocene ooze at the top of the section overlies an expanded lower Oligocene calcareous ooze rich in diatoms and radiolarians. All microfossil groups are abundant and well preserved. About 20 m of middle Eocene biosiliceous chalk disconformably overlies a 15-m-thick lower Eocene chalk. Core 207-1257C-1R contains the P/E boundary (see Fig. **F9,** p. 66, in the "Leg 207 Summary" chapter). Radiolarians cannot be identified to the species level in the Paleocene section, where the conspicuous presence of zeolites and occasional porcellanites indicates that these and other siliceous microfossils have been largely destroyed by sediment diagenesis.

The K/T boundary sequence is incomplete, as the lower Danian and upper Maastrichtian are missing in all holes and a slump is evident in the lower Paleocene of Hole 1257A. The lower Maastrichtian–lower Campanian zeolitic chalk (lithostratigraphic Subunit IIIB) is similar to the Paleocene, but radiolarians could be zoned in only a few samples and disappear from the section completely below this level. A condensed glauconite-rich horizon in Core 207-1257A-20X separates the Campanian chalk from the ~57 m of black shale below (lithostratigraphic Unit IV) that comprises OAEs 3 and 2. Calcareous microfossils are generally present throughout this unit, although preservation of foraminifers varies from often poorly preserved to pristine ("glassy"). The diversity of foraminifers is low. Cenomanian planktonic foraminifers near the base of the black shale indicate an environment shallower than that noted upsection; calcareous nannofossils are too few to yield an age. A sharp contact between the laminated black shales and the underlying clayey carbonate siltstone (lithostratigraphic Unit V) was recovered in Core 207-1257C-15R. Calcareous microfossils provide a middle–late Albian age for the bottom of the drilled section.

Calcareous Nannofossils

In the three holes at Site 1257, we recovered primarily Paleogene–mid-Cretaceous sediments that contain generally common to abundant

F7. Microfossil biozonation, p. 48.

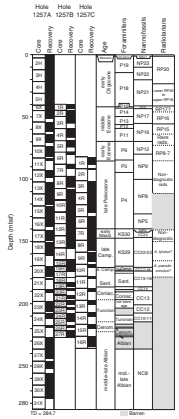

T3. Calcareous nannofossil datums, p. 81.

T4. Planktonic foraminifer species, p. 82.

T5. Planktonic foraminifer datums, p. 83.

T6. Calcareous nannofossils, p. 84.

T7. Planktonic foraminifer species, p. 86.

T8. Planktonic foraminifer species, p. 89.

calcareous nannofossils of moderate to good preservation, thereby permitting zonal or stage assignments to be made as summarized in Figure F7 and Tables T3 and T6. Core catcher samples were examined for all holes and supplemented by samples from the cores to further refine the zonal assignments. The following description is based on Hole 1257A, which was sampled in the most detail.

Samples 207-1257A-1H-1, 26 cm, to 1H-2, 45 cm, yielded a nannofossil assemblage of late Miocene age (Zone NN11 of the Martini, 1971, zonal compilation) that included *Discoaster brouweri, Discoaster braarudii, Discoaster quinqueramus,* and *Amaurolithus delicatus*. Samples 207-1257A-2H-1, 24 cm, to 2H-7, 23 cm, are of early Oligocene age (Zone NP23), as indicated by the presence of *Dictyococcites bisectus, Sphenolithus distentus,* and *Sphenolithus predistentus*. Samples 207-1257A-2H-CC to 3H-7, 25 cm, contain an early Oligocene–age assemblage (Zone NP22), including *Reticulofenestra umbilica* and *S. predistentus*. Samples that follow downhole from Samples 207-1257A-3H-CC to 6H-2, 65 cm, are earliest Oligocene age (Zone NP21), yielding *D. bisectus, R. umbilica, Ericsonia formosa, Sphenolithus pseudoradians,* and *Reticulofenstra oamaruensis*. Based on the presence of *Discoaster tanii* ssp. *nodifer, Discoaster saipanensis, Reticulofenestra reticulata,* and *Coccolithus eopelagicus,* Samples 207-1257A-6X-2, 104 cm, to 6X-2, 143 cm, were assigned a late Eocene age (Zone NP20). An interesting taxon found in this interval in Hole 1257B was *Isthmolithus recurvus,* a "cool-water" species seldom reported from the low latitudes. Its presence may indicate the upwelling of cooler waters. Also noted in this interval in Hole 1257B were slumps with darker-colored clasts relative to the matrix; the zonal age of these clasts and matrix, however, were all the same, indicating that the slump was intraformational.

A sharp disconformity at Section 207-1257A-6X-2, 137 cm, marked by a change from light to darker green sediment, separates the upper from the middle Eocene. The middle Eocene spans the interval from Samples 207-1257A-6X-3, 24 cm, to 9X-5, 25 cm, and comprises Zones NP17 and NP16, based on the presence of *Chiasmolithus grandis, S. distentus, D. tanii* ssp. *nodifer, Sphenolithus radians, R. umbilica,* and *D. bisectus*. Subjacent samples from Samples 207-1257A-9X-CC to 10X-CC contain *Chiasmolithus solitus, Discoaster kueperi, Chiasmolithus consuetus, Discoaster multiradiatus, Discoaster diastypus, Zygrhablithus bijugatus,* and *S. radians* and are thus of early Eocene age (Zone NP11).

A nannofossil assemblage consisting of *D. multiradiatus, Toweius pertusus,* and *Fasciculithus tympaniformis* characterizes Sections 207-1257A-11X-2 (bottom) to 12X-CC, which have a late Paleocene–early Eocene age (Zone NP9). A late Paleocene age (Zone NP8) is assigned to Sections 207-1257A-13X-CC to 15X-CC, based on the presence of *Heliolithus riedelii, Discoaster mohleri, D. multiradiatus,* and *Discoaster nobilis*. *Chiasmolithus bidens, Fasciculithus ulii, Ericsonia subpertusa,* and *Cruciplacolithus tenuis* in Sample 207-1257A-16X-CC indicate the presence of the early late Paleocene nannofossil Zone NP5.

Samples 207-1257A-17X-1, 25 cm, to 17X-1, 102 cm, yielded a nannofossil assemblage of mid-Maastrichtian age (Zone CC24 of the Sissingh, 1977, zonal scheme), including *Reinhardtites levis, Arkhangelskiella cymbiformis,* and *Ceratolithoides aculeus* (internal angle of the horns = <90°). The interval from Samples 207-1257A-17X-5, 102 cm, to 20X-2, 102 cm, is mid-Campanian–early Maastrichtian in age (Zones CC22–CC23), as indicated by the presence of *Uniplanarius trifidum, R. levis,* and *A. cymbiformis*. Sections 207-1257A-20X-3 to 22X-CC contain a Coniacian–early Campanian assemblage (Zones CC13–CC18), includ-

ing *Quadrum gartneri* and *Marthasterites furcatus*. The subjacent Samples 207-1257A-23X-CC to 24X-CC yielded an impoverished nannoflora presumably of Turonian age (Zones CC10–CC12) with *Eprolithus floralis, Lithastrinus septentrionalis,* and *Eiffellithus eximius*.

Based on the absence of *Eiffellithus turriseifelii* and the presence of *Tranolithus orionatus, Rhagodiscus asper, Rhagodiscus angustus,* and *Corollithion achylostaurion* in Samples 207-1257A-27X-4, 143 cm, to 31X-CC, they were assigned an Albian age (Zone NC8).

Planktonic Foraminifers

Planktonic foraminifer biostratigraphy at Site 1257 was based upon a combination of core catchers from all three holes and samples taken in every section in Hole 1257A. Zonal assignments are summarized in Figure **F7** and Tables **T4, T5, T7,** and **T8.** Planktonic foraminifer Zone M14/M13b through Albian Zone KS13 were identified in Hole 1257A, along with significant breaks in the biozonation of the lower Oligocene–upper Miocene, the lower–middle Eocene, the lower Maastrichtian–Danian, and the Albian–Cenomanian. Planktonic foraminifers were present in nearly all samples but varied widely in preservation and abundance. Preservation was best in clay-rich parts of the Cenomanian–Santonian sequence, although foraminifers were difficult to extract and completely clean in the organic-rich calcareous claystones (black shales). Foraminifers in the light-colored bands in the black shales were frequently filled with calcite spar. Good preservation was found in the Miocene, Oligocene, middle Eocene, and Paleocene, whereas preservation was moderate or poor in the hard chalk of the lower Eocene, Campanian–Maastrichtian sequence, and Albian marls.

Sample 207-1257A-1H-1, 0–2 cm, contains Pleistocene planktonic foraminifers, including *Globorotalia menardii, Globigerinoides ruber,* and *Globigerinoides sacculifer.* Brown and green calcareous ooze in Section 207-1257A-1H-1 contains an upper Miocene assemblage of *Globigerinoides siegliei, Globorotalia plesiotumida,* and *Globorotalia juani,* which suggests uppermost Miocene Zone M14. Sample 207-1257A-1H-1, 50–52 cm, contains reworked middle Miocene *Fohsella fohsi,* which represents Zones M8–M9. A lower Oligocene Zone P19 assemblage, including *Turborotalia ampliapertura* without *Pseudohastigerina* sp., is present in the light yellow nannofossil ooze in Sample 207-1257A-1H-2, 50–52 cm. Typical species belonging to lower Oligocene Zone P19 include common *T. ampliapertura, Subbotina galavisi, Subbotina globularis, Subbotina euapertura,* and *Globorotaloides suteri* in the >150-µm fraction. *Cassigerinella chipolensis, Tenuitella gemma, Tenuitella munda, Chiloguembelina cubensis,* and *Globigerina praebulloides* are common constituents of the <150-µm fraction. The boundary between Zones P18 and P19 is located between Samples 207-1257A-3H-2, 50–54 cm, and 3H-1, 50–54 cm, and is marked by the last occurrences of *Pseudohastigerina micra* and *Pseudohastigerina naguewichiensis*.

The E/O boundary is present between Samples 207-1257A-6X-1, 46–48 cm, and 7X-1, 52–54 cm, recording the contact between the lowermost Zone P18 and upper Zone P14. A more complete boundary section was recovered from Hole 1257B between Samples 207-1257B-1R-2, 1–2 cm (Zone P18), and 1R-2, 47–48 cm (Zone P16–P15). Upper Eocene foraminifers include well-preserved *Turborotalia pseudoampliapertura, Hantkenina alabamensis, Subbotina yeguaensis, Subbotina gortani,* and *Turborotalia cerroazulensis* without *Globigerinatheka* sp. The absence of *Globigerinatheka index* or *Globigerinatheka semiinvoluta* suggests a latest

Eocene age for this sample, but the absence of *Cribrohantkenina inflata* or *Turborotalia cunielensis* suggests the sample is from Zone P15. Hantkeninids include strongly inflated *H. alabamensis* that closely resemble the holotype of this species and are ancestral to *Cribrohantkenina* in the upper part of Zone P15. Assemblages in Hole 1257A representing Zone P14 include *Globigerinatheka tropicalis,* which evolved late in Zone P14, as well as typical upper middle and upper Eocene species such as *Turborotalia cerraozulensis, Acarinina rohri,* and *Morozovella spinulosa*. The presence of morozovellids and acarininids below Sample 207-1257A-7X-1, 52–54 cm, shows that the fauna predates the extinction of these groups in the lower part of Zone P15.

A regular succession of middle Eocene biozones is present between Cores 207-1257A-7X and 9X. The P14/P13 boundary occurs between Samples 207-1257A-7X-3, 49–52 cm, and 7X-4, 47–51 cm, based upon the last occurrence of *Orbulinoides beckmanni*. Zone P13 assemblages are species rich and include *Acarinina praetopilensis, Turborotalia pomeroli, P. micra, M. spinulosa, Muricoglobigerina senni,* and *A. rohri*. The boundary between Zones P12 and P13 is located between Samples 207-1257A-8X-2, 47–48 cm, and 8X-3, 51–53 cm, based on the first occurrence of *O. beckmanni*. The evolution of *O. beckmanni* involves the gradual envelopment of the test by the last two chambers of the final whorl, which eventually results in a spherical shell completely enclosed by the last chamber. This evolutionary transition is well represented at Site 1257. The last appearance of *Morozovella aragonensis* between Samples 207-1257A-8X-CC and 9X-5, 50–54 cm, marks the Zone P11/P12 boundary. Typical assemblages from Zone P11 include *Acarinina bullbrooki, M. aragonensis, Igorina broedermanni, Acarinina topilensis,* and *Turborotalia griffinae*. Specimens of *Clavigerinella akersi* were found in Sample 207-1257A-9X-4, 50–54 cm.

The lower/middle Eocene boundary is present between Samples 207-1257A-9X-5, 50–54 cm, and 9X-CC, juxtaposing faunas of Zone P11 (or possibly Zone P10) and Subzone P6b. The base of Zone P6 was not found in Hole 1257A but has been located between Samples 207-1257C-1R-3, 123–125 cm, and 1R-CC. These samples span a green clay bed in interval 207-1257C-1R-5, 48–51 cm, which may represent the P/E boundary. Sample 207-1257C-1R-CC contains a typical Zone P5 assemblage with *Morozovella velascoensis, Morozovella subbotinae, Morozovella occulsa, Igorina albeari, Globonomalina planoconica, Acarinina coalingensis,* and *Subbotina velascoensis*. Unusual elements include *Igorina broadermanni, Acarinina wilcoxensis,* and *Chiloguembelina wilcoxensis,* all of which appear just above to the P/E boundary. A latest Paleocene age for Sample 207-1257C-1R-CC is further suggested by the very rare occurrence of the benthic foraminifer *Gavelinella beccariiformis,* which becomes extinct at the onset of the $\delta^{13}C$ event associated with the P/E boundary. The P/E boundary is difficult to define precisely in Hole 1257A, owing to very poor preservation in Sample 207-1257A-11X-CC, but is known to occur between Samples 207-1257A-11X-2, 27–32 cm, and 12X-1, 50–54 cm, most likely in the core break.

A thick Paleocene succession is found between Cores 207-1257A-11X and 16X. These cores contain a typical assemblage from Zone P4 that includes *M. velascoensis, Morozovella aequa, Morozovella occlusa, Globanomalina pseudomenardii,* and *Acarinina mckannai*. Zone P4 faunas are partly contaminated by foraminifers from Zones P2 and P3 as well as Maastrichtian foraminifers in Core 207-1257A-16X, where species such as *Morozovella conicotruncata* (Zones P3–P4), *Praemurica inconstans* (Zones P2–P3), and *Pseudoguembelina costulata* (Cretaceous) are mixed

into faunas containing *G. pseudomenardii* (index species for Zone P4). In Core 207-1257A-16X, a slumped interval includes white limestone containing *P. inconstans* from Zone P2 and lower Maastrichtian chalk belonging to Zone KS30.

Beginning in Sample 207-1257A-17X-1, 50–54 cm, and continuing to the base of the hole, the succession of planktonic foraminifers indicates a series of biozones between lower Maastrichtian Zone KS30 and middle Albian Zone KS13. Campanian–lower Maastrichtian Zone KS30 (*Gansserina gansseri*) extends from Samples 207-1257A-17X-1, 50–54 cm, to 18X-CC. The Maastrichtian assemblages contain common to few *Rugotruncana subcircumnodifer, Globigerinelloides prairiehillensis, P. costulata, Heterohelix puncticulata,* and *Rugoglobigerina macrocephala,* with occasional *Abathomphalus intermedius, Globotruncanella pschadae, Rosita fornicata,* and *Globotruncana aegyptiaca*. *Gansserina gansseri* is absent, so differentiation of the Maastrichtian part of Zone KS30 from the subadjacent Campanian part of Zone KS30 relies on a combination of the foraminifer data with nannofossil datums (see **"Calcareous Nannofossils,"** p. 11). Between Sample 207-1257A-19X-CC and the base of the glauconitic calcareous chalk in Core 20X, planktonic foraminifers are absent and the faunas are represented by diverse benthic foraminifer assemblages.

Dark black shales in Sample 207-1257A-20X-CC contain a low-diversity assemblage of *Heterohelix globulosa, Hedbergella delrioensis, Hedbergella planispira,* and *Dicarinella canaliculata*. This foraminifer fauna, together with nannofossil data (see **"Calcareous Nannofossils,"** p. 11), suggest a Coniacian–Santonian age (Zones KS23–KS24). Samples between 207-1257A-21X-CC and 25X-2, 45–47 cm, could not be dated precisely, owing to the absence of marker species. These samples were mostly dominated by small foraminifers representing only four to five species, none of which are useful in differentiating between Cenomanian and Santonian ages. However, Sample 207-1257A-25X-CC contains *Whiteinella inornata* and *Rotalipora greenhornensis,* suggesting that the fauna dates from the late Cenomanian.

Preservation varies markedly through the organic marl sequence. Foraminifers are typically larger and more likely to be filled with sparry calcite in the lighter-colored interbeds and are typically better preserved, even with glassy shells, in the darker, more clay-rich interbeds. Benthic foraminifers are nearly absent, but both the abundance of benthic foraminifers and species diversity of planktonic foraminifers are highest in the Coniacian–Santonian interval and decrease toward the upper Cenomanian interval.

The green silty calcareous claystone in Samples 207-1257A-26X-2, 96–98 cm, to 36X-CC contain only rare foraminifers, when they are present at all. All foraminifers are recrystallized and filled with calcite spar. Sample 207-1257A-27X-CC contains a few specimens of *Ticinella raynaudi,* along with fragments of fish bones and echinoderm debris. Sample 207-1257A-29X-CC contained the highest-diversity fauna of any samples examined in the claystone, with *Favusella washitensis, H. delrioensis, H. planispira,* and *Ticinella* sp. The assemblage broadly suggests an age of middle–late Albian. The low species diversity and abundance in most claystone samples suggests that the depositional environment was not favorable to planktonic foraminifers, perhaps because the waters were shallow or of unusually high salinity. The paleogeography of Demerara Rise in the Albian suggests the region was part of a large epicontinental sea between Africa and South America (Gouyet et al., 1994; Benkhelil et al., 1995) and supports the hypothesis that the

low taxonomic diversity of Albian species at Site 1257 is related to shallow-water habitats.

Radiolarians

Site 1257 radiolarians were found in most of the recovered Tertiary material as well as in the uppermost Cretaceous (lower Maastrichtian–Campanian). Core catcher samples were examined systematically from Hole 1257A. A limited number of samples were also taken from Holes 1257B and 1257C to examine radiolarian presence/absence in the Upper Cretaceous black shales or to better constrain the age of some cores.

The radiolarian fauna is well preserved and abundant in the Oligocene and Eocene parts of the site. Samples 207-1257A-2H-CC and 3H-CC are considered to have an early Oligocene age, as they can be assigned with confidence to Zone RP20 based on the presence of *Lithocyclia crux*.

Radiolarian preservation is relatively poor in Samples 207-1257A-4H-CC and 5H-CC. Based on the presence of *Theocyrtis tuberosa* and *Dictyoprora mongolfieri,* these samples can be assigned to an interval between the lower part of Zone RP20 and the upper part of Zone RP18. Radiolarian preservation greatly improves in Sample 207-1257A-6X-CC, in which the abundant presence of *Podocyrtis goetheana* and *Eusyringium fistuligerum* suggests an age between the lower part of Zone RP18 and the base of Zone RP16.

Sample 207-1257A-7X-CC is assigned to Zone RP16, as *P. goetheana* (marker species of the base of this zone) co-occurs with *Spongatractus pachystylus*. This is younger than calcareous nannofossil and foraminiferal datums of this interval, which suggest lower Zones NP17 and P13, respectively. The absence of *S. pachystylus* in Sample 207-1257A-6X-CC (containing an abundant and well-preserved radiolarian fauna) implies that the boundary between Zones RP16 and RP17 may be placed in Core 207-1257A-7X. The abundant presence of *Podocyrtis chalara* in Sample 207-1257A-8X-CC (largely outnumbering the few specimens of *Podocyrtis mitra*) suggests that the boundary between Zones RP16 and RP15 can be placed in Core 207-1257A-8X.

Finally, Samples 207-1257A-10X-CC to 11X-1, 49–54 cm, can be assigned to Zone RP7 or RP8, based on the presence of *Podocyrtis papalis* and *Pterocodon ampla*. Further below, poor preservation prevented identification of any age-diagnostic radiolarians.

Cretaceous radiolarians were observed in Cores 207-1257A-17X, 18X, and 20X as well as in Core 207-1257C-10R. Preliminary identifications were made on board on the basis of observations with a stereoscopic microscope, but they will need to be confirmed with the use of a scanning electron microscope. Sample 207-1257A-18X-CC may be assigned to the upper Campanian–Maastrichtian *Amphipyndax tylotus* Zone and Sample 207-1257C-20R-CC to the Campanian *Amphipyndax pseudoconulus* Zone, based on the presence of their respective marker species. No radiolarians were identified from the Albian–Santonian interval.

PALEOMAGNETISM

The sedimentary record of Site 1257 is in packets separated by major hiatuses; therefore, the assignments of polarity chrons to interpret magnetostratigraphic zones rely on biostratigraphic constraints. The magnetostratigraphy of the combined holes is interpreted to resolve por-

tions of Chrons upper C33n–C31r spanning a thick Campanian/Maastrichtian boundary interval, portions of Chrons C20r–C17n in a relatively condensed middle Eocene interval, and Chrons C26n–C24r in an expanded upper Paleocene section.

Shipboard and Shore-Based Procedures and Data Filters

Details are given in "Paleomagnetism," p. 16, in the "Explanatory Notes" chapter of the standard shipboard analysis using the pass-through cryogenic magnetometer, the filtering and polarity interpretation procedures of these data, and the shore-based progressive demagnetization of discrete minicores. Shipboard measurements of each section were at natural remanent magnetization (NRM) 10- and 15-mT alternating-field (AF) demagnetization steps, with an additional 20-mT step applied if core flow permitted (Table T9). The 10-mT step appeared to be effective in removing extraneous overprints induced during the drilling process. In general, the additional 20-mT demagnetization step did not significantly alter the magnetic directions obtained at the prior 15-mT step for the majority of the sediment types. The black shale intervals of the Cenomanian–Santonian displayed magnetizations near the background noise level of the shipboard cryogenic magnetometer, are commonly highly fractured or biscuited, and are within the Long Cretaceous Normal Polarity Superchron C34n. We decided to leave the majority of the black shale cores intact rather than partially demagnetize the sediments without the prospect of obtaining useful shipboard information.

T9. Shipboard paleomagnetic analyses, p. 91.

Oriented paleomagnetic cylinders were drill-pressed at one-per-section spacing in the entire Campanian–middle Eocene in Hole 1257B for combined progressive AF and thermal demagnetization at the magnetic-shielded room facility at the University of Munich, Germany. These shore-based measurements enabled resolution of removed and characteristic components of magnetization and significantly modified the tentative shipboard polarity interpretations from all facies. The magnetic polarity of each minicore was interpreted from an examination of the movement of its magnetic vector during progressive demagnetization (see "Paleomagnetism," p. 16, in the "Explanatory Notes" chapter) (Table T10). In addition, revisions to the initial shipboard biostratigraphy necessitated revisions of assignments of polarity chrons in portions of this succession that are interrupted by several hiatuses.

T10. Polarity interpretations and ChRM, p. 92.

Paleomagnetic Behavior and Interpretations of Magnetostratigraphy

Upper Miocene and Lower Oligocene

The uppermost 40 m of Hole 1257A was APC cored. The lower three of these five cores were oriented with the Tensor tool. The initial 10-mT step of AF demagnetization of the Oligocene foraminifer nannofossil oozes removed a component with positive inclination. The progressive 15- and 20-mT steps generally shifted the inclinations to low positive or negative values but with a high degree of scatter. No significant intervals of sustained positive inclination were observed. Magnetic intensity after 20 mT was generally in the range of 10^{-4} to 10^{-2} A/m and displayed an artifact of higher intensity in the top section of each core (right-hand column in Fig. F8). The removed component is probably a com-

F8. Shipboard paleomagnetic data, p. 49.

posite overprint from drilling-induced magnetization and from shear remagnetization near the margins of the piston core liner (e.g., review by Acton et al., 2002) and the present-day normal polarity field. NRM declinations and inclinations were generally random, and although the progressive AF demagnetization resulted in a relatively stable direction for each independent sample, this scatter in sample groups was not improved (inclination column for Hole 1257A in Fig. F8).

Our preferred explanation for this abundance of negative inclinations and scattered declinations is that these Oligocene oozes have variable and semipersistent overprints of present-day normal polarity superimposed on a primary reversed polarity component. This interpretation is supported by the earliest Oligocene paleontological age (Zones NP21–NP23 and P18–P19); therefore, we assign the entire set of lower Oligocene sediments to Chron C12r. No discrete minicores were analyzed from the Oligocene facies at any site; therefore, the interpretation of Chron C12r assumes that Site 1257 was located significantly north of the Oligocene paleoequator. The recovered Oligocene interval of the reversed polarity Chron C12r zone apparently did not include either of the bounding normal polarity zones (base of Chron C12n or top of Chron C13n).

The uppermost 1.5 m of Hole 1257A (Section 207-1257A-1H-1 to Sample 1H-2, 10 cm) is a Miocene reddish brown to greenish brown clayey carbonate ooze. A sharp polarity transition at Sample 207-1257A-1H-1, 100 cm, indicated by both declination and inclination shifts, separates an upper interval dominated by normal polarity and an underlying reversed polarity zone. It was not possible to unambiguously make a polarity chron assignment from the broad shipboard paleontology of this capping sediment unit.

Eocene

The Eocene greenish white foraminifer nannofossil chalk yielded a relatively well defined suite of polarity zones. Intensities of characteristic magnetization averaged 1×10^{-3} A/m. However, assignments of polarity chrons to these zones are inhibited by the biostratigraphic resolution and discrepancies between preliminary foraminifer and calcareous nannofossil zonal assignments compared to the reference biomagnetic polarity timescale (e.g., lower middle Eocene–lower Eocene foraminifer and nannofossil biostratigraphic zonation scales in Fig. F9 compared to those of Fig. F5, p. 59, in the "Explanatory Notes" chapter).

A thin upper Eocene unit (foraminifer Zone P16) is bounded by disconformities at the overlying lower Oligocene (Zone P18) and underlying middle Eocene (Zone P16). Minicores from this upper Eocene zone yielded normal polarity, but the biostratigraphic constraints are not adequate to determine whether this normal polarity zone corresponds to Chron C15n or C16n.

The biostratigraphy of the hiatus-delimited 25-m-thick middle Eocene unit indicates a span of nearly 5 m.y. that should encompass Chrons C17–C20. Shipboard clusters of negative inclination were originally interpreted as reversed polarity zones (Fig. F8), but progressive thermal demagnetization of discrete minicores indicated that inclinations are not reliable guides to the polarities of these near-equatorial samples. Comparison between the polarity interpretations of the minicores to the generalized biostratigraphy suggests that the normal polarity interval at the top of this middle Eocene segment may correspond to the base of Chron C17n and that the reversed polarity interval at the

F9. Shore-based paleomagnetic data, p. 50.

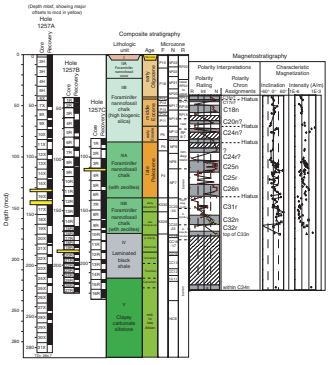

base of this segment might correspond to Chron C20r. However, the ambiguity of these assignments and those of the intervening polarity zones merits caution (if fully resolved by our sample spacing in this compact unit, which is doubtful).

A hiatus spanning foraminifer Zones at least P7–P10 separates the lower Eocene unit from the middle Eocene unit. The behavior of magnetic vectors during progressive thermal demagnetization of minicores suggested that the lower Eocene unit is dominated by normal polarity, which we tentatively assign to Chron C24n.

Upper Paleocene

In contrast to the compact Eocene, the upper Paleocene is relatively expanded. The array of minicores yielded two main pairs of normal and reversed polarity zones plus a possible thin normal polarity interval in the uppermost Paleocene.

Biostratigraphic constraints suggest that these polarity zones are Chrons C24r–C25n–C25r–C26n. The base of the Paleocene section is a massive slump deposit, and its magnetization appears to have been acquired during redeposition in a normal polarity field, which is also interpreted as Chron C26n.

Cenomanian–Maastrichtian

The upper Campanian and lower Maastrichtian chalks have relatively weak magnetizations that were less reliable for magnetic polarity assignments (see the "Polarity Rating" column in Fig. F9). Minicores were collected across the Campanian–Maastrichtian boundary interval from all three Site 1257 holes to improve the resolution of the magnetostratigraphy. When these sets are merged using the composite depth offsets, a consistent and simple pattern of polarity zones emerges. The upper half of the succession is a single reversed polarity zone, and the early Maastrichtian age implies an assignment of Chron C31r. The upper Campanian interval is constrained by the foraminifer age span to be Chrons C32n–C32r–uppermost C33n.

Albian–Santonian

The underlying black shale of the Cenomanian–Santonian displays the highest intensity magnetization (10^{-2} to 10^{-1} A/m after 20-mT AF demagnetization) of any facies at Site 1257 (Fig. F9). In contrast, the black shale unit at Site 1258 has magnetic intensities near the background noise limit of the shipboard magnetometer. Positive inclinations dominate the magnetization of this black shale, and these are interpreted as an incomplete removal of a steeper normal polarity overprint of the present day (20° dipole inclination) on the predicted Cretaceous Normal Polarity Superchron C34n.

The Albian clayey carbonate siltstone displayed a relatively weak magnetization (Fig. F9). The Albian stage is entirely within Cretaceous Superchron C34n; therefore, we expected low-angle positive polarity (if a present-day normal polarity overprint is present) or low-angle negative polarity (near-equatorial Cretaceous paleolatitude). The single minicore yielded a normal polarity with positive inclination (base of magnetostratigraphy columns of Fig. F9). This is consistent with paleomagnetic results from Albian–Cenomanian sediments at other Leg 207 sites, which suggests a mid-Cretaceous paleolatitude at ~10°–15°N.

COMPOSITE DEPTHS

Site 1257 extended to a total depth of 284.7 mbsf (Core 207-1257A-31X). A good composite section was established for the upper Paleocene (~100–150 meters composite depth [mcd]), but it was not possible to construct a complete composite depth scale for the remainder of the section. The severe biscuiting in the XCB section of Hole 1257A combined with poor recovery in parts of both the XCB- (Hole 1257A) and RCB- (Holes 1257B and 1257C) cored sections precluded rigorous correlation among holes (see "Lithostratigraphy," p. 4).

At Site 1257, magnetic susceptibility, gamma ray attenuation (GRA) bulk density, and noncontact resistivity (NCR) data were collected with the multisensor track (MST) at 2.5-cm intervals on all core sections. Compressional (*P*)-wave velocity data were collected at 2.5-cm intervals on APC cores. Natural gamma ray (NGR) data were collected at 15-cm intervals on XCB cores from Hole 1257A and at 7.5-cm intervals on all cores from Holes 1257B and 1257C. In addition, color spectral reflectance data were collected at 2.5-cm intervals on all split cores from Holes 1257A, 1257B, and 1257C. Magnetic susceptibility data provided the primary data set that we used to correlate among holes in the interval between 100 and 150 mcd, where core recovery and quality were sufficient in each of the holes to allow core-to-core comparisons. NGR data, although collected at a lower resolution than magnetic susceptibility, provided additional verification of the hole-to-hole ties.

The biscuited and fractured nature of the XCB and RCB cores resulted in low signal-to-noise ratios for the MST sensors (e.g., GRA bulk density and spectral reflectance) that analyze small portions (i.e., ~1 cm) of the core. These sensors recorded data in individual biscuits and the slurry between the biscuits. In addition, the XCB and RCB core diameter is less consistent than APC sections, thus increasing the variability in data recorded using these high-resolution sensors. The magnetic susceptibility and NGR systems, however, sense a larger portion of the core (~5–15 cm). The data recorded by these types of sensors tend to average out some of the core-diameter variability as well as the signal variability resulting from biscuiting.

Composite Section

The poor recovery in much of the drilled section at Site 1257 combined with a low signal-to-noise ratio seen in much of the MST sensor data precluded placing many of the Site 1257 cores into a composite depth framework. The composite depth table (Table **T11;** Fig. **F10**) identifies the cores that could be correlated (i.e., depth adjusted) among holes and lists the offsets applied to each core. In many cases, the poor core quality (i.e., biscuited cores) resulted in only short intervals in a single core having a high-quality signal for correlation. Thus, correlated cores may only have 1- to 2-m of section with similar MST signals. The few ties, therefore, that could be made outside of the upper Paleocene interval (discussed below) are tenuous, at best.

Paleocene Composite Record

Good core recovery and minimal drilling disturbance in the interval from ~100 to 150 mcd (Cores 207-1257B-9R through 12R and 207-1257C-3R through 7R) allowed us to construct a high-quality upper Paleocene composite section (Figs. **F11, F12**). The RCB cores from Holes

T11. Composite depth offsets, p. 95.

F10. Magnetic susceptibility, p. 51.

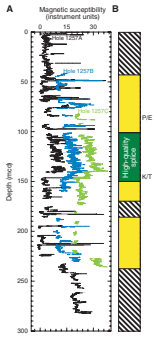

F11. Upper Paleocene magnetic susceptibility, p. 52.

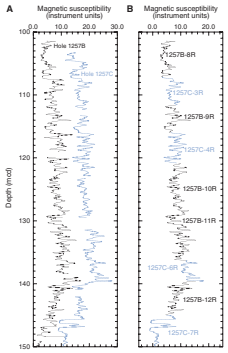

F12. NGR and spliced magnetic susceptibility, p. 53.

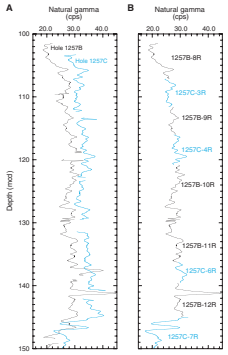

1257B and 1257C have excellent magnetic susceptibility and NGR records with high signal-to-noise ratios. In contrast, the XCB cores in Hole 1257A suffer from a greater degree of core disturbance (biscuiting) and are not useful for composite section construction. The composite interval from 100 to 150 mcd is nearly complete, with only one core gap (between Cores 207-1257B-10R and 11R).

The periodic variability in the magnetic susceptibility data will provide a good basis for postcruise cyclostratigraphic studies. Age control is excellent, with two well-defined paleomagnetic datums (top of Chron C26n and the top and base of Chron C25n) in the section (see **"Paleomagnetism,"** p. 16). Preliminary investigation suggests the dominant periodicities of the magnetic susceptibility data are Milankovitch in nature.

Splice Record

Following construction of the composite depth section for the upper Paleocene interval at Site 1257, a single spliced record was assembled for the aligned cores over the interval from 102 to 151 mcd by patching across cores with data primarily from Holes 1257B and 1257C (Table **T12;** Figs. **F11, F12**). Only one core gap could not be bridged (the interval between Cores 207-1257B-10R and 11R).

Intervals having significant disturbance or distortion were avoided when making the splice. The Site 1257 splice can be used as a sampling guide to recover a nearly continuous upper Paleocene sedimentary sequence. When utilizing this splice as a sampling guide, it is advisable to overlap a few decimeters from different holes when sampling to accommodate anticipated ongoing development of the depth scale. The reason for this approach is that distortion of the cored sequence can lead to stretching or compression of sedimentary features. Because much of the distortion occurs in individual cores on depth scales of <9 m, it was not possible to align every feature in the MST and color reflectance records. However, at crossover points along the splice (Table **T12**), care was taken to align highly identifiable features from cores in each hole. Postcruise work will establish a detailed correlation between holes by establishing a revised meters composite depth (rmcd) scale that allows differential stretching and squeezing in cores.

T12. Upper Paleocene splice tie points, p. 96.

SEDIMENTATION RATES

Age-Depth Model

An age-depth model for Site 1257 was established by combining all available biostratigraphic and magnetostratigraphic datums of Hole 1257A (Fig. **F13**). The diagram was constructed by plotting highest and lowest possible ages for selected paleontological samples examined shipboard against the depth of those samples (Table **T13**). In addition, the age and depth of magnetic reversals recognized on board ship (Table **T14**) are also plotted. Poor preservation or absence of microfossils limits lithologic dating in parts of the succession. In particular, the Turonian–Albian interval was difficult to date with shipboard samples.

F13. Age-depth plot, p. 54.

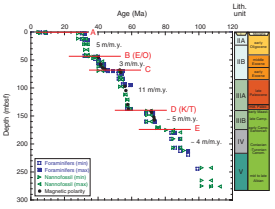

T13. Calcareous nannofossil and planktonic foraminifer datums, p. 97.

T14. Magnetostratigraphic datums, p. 99.

Sedimentation Rates

Calculated linear sedimentation rates (LSRs) for Hole 1257A vary between 5 and 10 m/m.y. (Table T15). These rates are typical for pelagic oozes and chalks, which are the dominant lithology of lithostratigraphic Units II and III (see "Lithostratigraphy," p. 4). Based on significant changes in sedimentation rates, it is possible to differentiate the following six intervals with approximately constant sedimentation rates:

1. Neogene (0.0–2.5 mbsf): poor and ambiguous biostratigraphic data. This interval is not discussed further.
2. Oligocene (2.5–43.5 mbsf): LSR = ~9 m/m.y.
3. Middle Eocene (43.5–70.0 mbsf): LSR = ~5 m/m.y.
4. Early Eocene–late Paleocene (70–140 mbsf): LSR = ~10 m/m.y.
5. Maastrichtian–Campanian (140–175 mbsf): LSR = ~5 m/m.y.
6. Santonian–Cenomanian (175–220 mbsf): LSR = ~4 m/m.y.

Mass accumulation rate (MAR) calculations, using the above LSRs and averaged dry bulk density of the major lithologies (see "Physical Properties," p. 27), are given in Table T15. These calculations may better reflect sedimentation processes because the calculation corrects for the influence of sediment compaction. Oligocene MARs are relatively high, reaching values of 0.8 g/cm²/k.y. The middle Eocene exhibits values of 0.4 g/cm²/k.y. Highest overall values of ~1.2 g/cm²/k.y. were calculated for the lower Eocene–upper Paleocene interval. Rates of 0.7–0.9 g/cm²/k.y. were observed for the Upper Cretaceous intervals, including the black shale facies (Unit IV [175–220 mbsf]).

Hiatuses

The six intervals described above are bounded by abrupt changes in sediment ages, clearly suggesting four distinct hiatuses. Each of these hiatuses (see letters A–D in Fig. F13) spans several million years, based on biostratigraphic dating (see "Biostratigraphy," p. 11):

1. Hiatus A = ~20 m.y. (late Pliocene–early Oligocene),
2. Hiatus B = ~2–3 m.y. (early Oligocene–middle Eocene),
3. Hiatus C = ~10 m.y. (middle Eocene–early Eocene), and
4. Hiatus D = ~10 m.y. (late Paleocene–mid-Maastrichtian; K/T boundary).

These hiatuses may reflect periods of nondeposition or erosional events or a combination of both. Slump and debris flow deposits observed in sediment cores of Holes 1257B and 1257C (see "Lithostratigraphy," p. 4) closely correlate to these hiatuses and may argue for erosional events.

ORGANIC GEOCHEMISTRY

Concentrations of inorganic carbon (IC) and TOC were determined on sediments from Holes 1257A, 1257B, and 1257C. Organic matter atomic carbon/nitrogen (C/N) ratios and Rock-Eval pyrolysis analyses were employed to assess the type of organic matter contained in the sediments. Routine monitoring of interstitial gas contents of Hole

T15. LSRs and MARs, p. 100.

1257A was performed for drilling safety, and possible microbial activity was determined from headspace gas contents of this hole.

Inorganic and Organic Carbon Concentrations

Concentrations of IC vary from 1 to 11.9 wt% at Site 1257 (Table T16). These concentrations are equivalent to 9–99 wt% sedimentary $CaCO_3$, assuming that all of the carbonate is present as calcite or aragonite. Carbonate concentrations of the five lithostratigraphic units (see "Lithostratigraphy," p. 4) generally decrease with greater depth. However, the black shales that compose most of Unit IV still contain ~50 wt% carbonate, largely because calcite laminae were interspersed among the black shale laminae.

TOC concentrations of the five lithostratigraphic units have a wide range. The sediments of Units I, II, and III contain <0.1 wt% TOC (Table T16). In marked contrast, the black shales in Unit IV have TOC concentrations between 1 and 15.8 wt%. The calcareous siltstones that compose Unit V have TOC values that cluster closely around 0.6 wt%, which is twice that of the average deep-sea value of 0.3 wt% compiled by McIver (1975) from DSDP Legs 1–33.

T16. Carbon and nitrogen results, p. 101.

Organic Matter Source Characterization

Atomic C/N ratios were employed to help identify the origins of organic matter in Site 1257 sediments. C/N values in organic-lean Units I–III are low, commonly below the range typical of fresh algal organic matter (4–10) (Meyers, 1997). These values are probably an artifact of the low TOC concentrations, combined with the tendency of clay minerals to sorb ammonium ions generated during degradation of organic matter (Müller, 1977).

The C/N ratios of the black shales in Unit IV average 27, which is a value typical of land-plant organic matter but also common to Cretaceous black shales (Meyers, 1997). A van Krevelen–type plot of hydrogen index (HI) and oxygen index (OI) values (Fig. F14) indicates that the black shales in Unit IV contain Type II (algal) organic matter. High HI and low T_{max} values, like those found in the black shales (Table T17), are characteristic of thermally immature, relatively well preserved marine organic matter (Espitalié et al., 1977; Peters, 1986). Consequently, the elevated C/N values that mimic those of land-derived organic matter are likely to be the result of partial alteration of marine organic matter. A likely scenario is that nitrogen-rich components are preferentially degraded during sinking of organic matter to the seafloor, thereby elevating the C/N ratio of the surviving organic matter (Twichell et al., 2002).

Based on its low HI values, elevated OI values, and marine C/N values, organic matter in the calcareous siltstones of Unit V appears to be composed of Type IV kerogen. This type of kerogen represents marine organic matter that has experienced substantial degradation and oxidation. The presence of relatively uniform and elevated concentrations (TOC = 0.6 wt%) of detrital organic matter in these middle–upper Albian siltstones represents unusual conditions of deposition.

F14. Rock-Eval pyrolysis, p. 55.

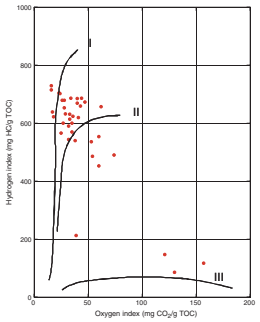

T17. Rock-Eval pyrolysis, p. 104.

Interstitial Gas Contents

Sediments at Site 1257 have fairly low interstitial gas concentrations. Neither gas voids nor other evidence of gas release from cores was ob-

served. A faint odor of hydrogen sulfide was noticeable in cores from the black shale in lithostratigraphic Unit IV (174–227 mbsf), but the natural gas analyzer, which has a sensitivity of ~1 ppmv, did not detect this gas in headspace samples.

Headspace gas results from routine safety monitoring and the special microbial gas study are very similar (Fig. F15). Methane first appears at 107 mbsf. Concentrations rapidly increase to reach a broad maximum between 180 and 218 mbsf before decreasing with greater depth in the core. High C_1/C_2 ratios and the absence of measurable amounts of higher molecular weight volatile hydrocarbons indicate that the methane is biogenic rather than thermogenic in origin (Table T18). A biogenic origin is also supported by the disappearance of interstitial sulfate at the same subbottom depth where methane concentrations begin to rise (see "Inorganic Geochemistry," p. 24); interstitial sulfate generally inhibits microbial methanogenesis (Claypool and Kvenvolden, 1983).

F15. Headspace gas methane concentrations, p. 56.

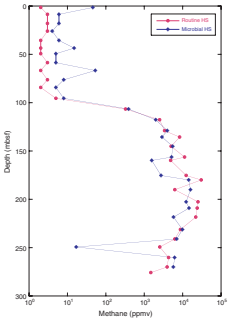

T18. Headspace analyses, p. 105.

INORGANIC GEOCHEMISTRY

We collected interstitial water from 30 samples at Site 1257: 12 from Hole 1257A (1.45–275.81 mbsf), 11 from Hole 1257B (52.75–225.30 mbsf), and 7 from Hole 1257C (157.50–233.87 mbsf). The samples from all three holes were taken to constitute a single depth profile. However, slight differences in lithology may cause minor breaks in concentration-depth gradients of some chemical parameters. Alkalinity was not determined in three samples because of low interstitial water yields.

Alkalinity, chloride, ammonium, and silica were determined by standard shipboard procedures (see "Inorganic Geochemistry," p. 31, in the "Explanatory Notes" chapter). The major ions Na, K, Mg, and Ca were analyzed by inductively coupled plasma–atomic emission spectroscopy (ICP-AES) after 50-fold sample dilution with deionized water. The minor components Li, B, Si, Fe, Mn, and Sr were determined by ICP-AES from 10-fold diluted interstitial water samples. From the minor component dilution, we determined sulfate as total sulfur by ICP-AES. Details of the methods, including the emission lines used for analysis, are given in "Inorganic Geochemistry," p. 31, in the "Explanatory Notes" chapter. Results of the chemical analyses are presented in Table T19 and in Figure F16.

T19. Interstitial water analyses, p. 106.

F16. Interstitial water profiles, p. 57.

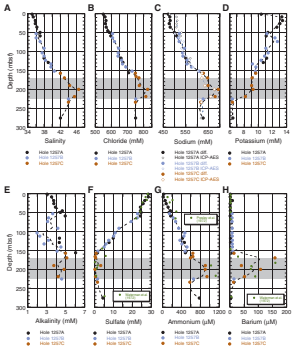

Black Shales as a Diagenesis Bioreactor

Interstitial water chemistry at Site 1257 is dominated by the presence of Santonian–Cenomanian black shales and associated organic matter–rich sediments (lithostratigraphic Unit IV [~270–320 mbsf]). The downhole dissolved sulfate concentration profile at the site approaches zero at the top of Unit IV (see Fig. F16F), suggesting that this organic matter–rich unit provides a suitable substrate for ongoing microbial activity at depth. The sulfate gradient from the top of Unit IV to the sediment/water interface is almost linear, suggesting that sulfate reduction is of minor importance at shallower depths. We interpret this observation to reflect minimal accumulation of sediments younger than middle Eocene age (see Fig. F7). A faint smell of hydrogen sulfide was noticeable in lithostratigraphic Unit III (above the black shales and associated organic matter–rich sediments). It is possible that pyrite formation in these sediments is triggered by hydrogen sulfide diffusion upward from the sediments in Unit IV, which are most likely iron limited. Shore-

based sulfur isotopic studies will help to test this hypothesis. The reducing character of the sedimentary column is also seen in slightly elevated manganese concentrations (Fig. F16P). Nevertheless, only very low concentrations (<1 µM) are attained in Unit IV. Presumably these sediments lost most of their manganese during or shortly after they were deposited, an interpretation that would indicate deposition under conditions of severe oxygen depletion. Alternatively, the low interstitial water manganese concentrations observed in Unit IV reflect the formation of manganese-rich carbonate phases (e.g., ankerite/rhodochrosite), which are common in organic matter–rich sediments. Shore-based chemical analysis of the interstitial water "squeeze cakes" will provide a definitive test of these two competing hypotheses.

Significantly, sulfate concentrations in lithostratigraphic Unit V (claystones and siltstones of Albian age) are slightly higher than those in the overlying black shale sequence, suggesting that Unit IV is the main "microbial bioreactor" influencing interstitial water sulfate, which is supplied from both above and below. Sulfate depletion is accompanied by increases in ammonium (Fig. F16G), a common respiration product of organic matter consumption. Ammonium concentrations peak in lithostratigraphic Unit IV and decrease almost linearly toward the sediment/seawater interface. In the very shallow subsurface, ammonium must be oxidized because concentrations are close to the detection limit in the two uppermost interstitial water samples taken. In lithostratigraphic Unit V (claystones and siltstones of Albian age), ammonium concentrations still remain at high levels, reflecting ongoing organic matter metabolization.

The complete absence of sulfate in Unit IV most probably promotes the occurrence of two other phenomena typically seen in organic matter–rich sediments: (1) mobilization of barium and (2) formation of dolomite. Increases in barium concentrations (Fig. F16H) are governed by barite solubility (Church and Wolgemuth, 1972) and are prone to even slight contamination by seawater sulfate. All cores from below ~60 mbsf were taken using RCB drilling technology, so minor seawater contamination cannot be completely excluded. However, sedimentological evidence points toward intense barium mobilization in the sedimentary sequence at Site 1257. Authigenic millimeter- to centimeter-scale barite crystals are frequently observed in the overlying Upper Cretaceous chalks (lithostratigraphic Unit III) (see "Lithostratigraphy," p. 4). Similar sedimentological and mineralogical relationships are reported elsewhere (Brumsack, 1986; Torres et al., 1996).

The downhole interstitial water concentration profile for magnesium is linear from the sediment/water interface to the middle of lithostratigraphic Unit IV, where concentrations reach their minimum before increasing to significantly higher values in the underlying Albian sediments (Fig. F16I, F16K) (~200 mbsf). In direct contrast, the downhole interstitial water calcium profile is nonlinear and calcium concentrations peak in the middle of Unit IV before decreasing to significantly lower values in the underlying Albian sediments (Fig. F16I). These observations indicate the existence of a significant sink for magnesium and source for calcium in the sulfate-depleted black shale interval, more likely formation of dolomite rather than alteration of volcanogenic ash.

The nonlinearity of the calcium profile from the top of Unit IV to the sediment/water interface indicates calcite precipitation in Paleogene sediments, as deduced from the associated consumption of alkalinity. This interpretation is consistent with reports of poor preservation of calcareous planktonic foraminifers and nannofossils of early Eocene age

(see "Biostratigraphy," p. 11). The downhole interstitial water strontium profile at Site 1257 shows a near-linear increase from the sediment/water interface to high values (>1000 µM) that are maintained from the middle of lithostratigraphic Unit IV (~200 mbsf) to the deepest sample analyzed (~275 mbsf) (Fig. F16J). The shape of this strontium profile contrasts with the typical ooze–chalk transition "mid-depth maximum" (Baker et al., 1982) and suggests that carbonate diagenesis in the Paleogene strata, as inferred from the calcium and alkalinity profiles, is dominated by calcite precipitation rather than dissolution or in situ recrystallization. We interpret this observation to result from minimal accumulation of sediments younger than middle Eocene age (see Fig. F7). Similar findings have been reported from Blake Nose, where post-Eocene sedimentation is also absent (Rudnicki et al., 2001). Instead, carbonate dissolution and recrystallization reactions appear to be focused in sediments from the middle of Unit IV and possibly below. In fact, the relatively high strontium values and steep downhole gradients observed (>10 times seawater values and ~5 µM/m, respectively) suggest a sediment source (possibly aragonite-rich shallow-water carbonate sediments) may underlie the drilled section and continue to exert significant control on the Site 1257 interstitial water strontium profile. In this context, the pronounced negative linear relationship between magnesium and strontium is noteworthy (Fig. F17A). The maxima in lithium and boron (Fig. F16L, F16M) may be associated with this process, even though neither element is significantly enriched in carbonate sediments.

Dissolved silica concentrations increase with depth, reflecting the presence of biogenic silica (Fig. F16N). At greater depth, decreases in dissolved silica may also be associated with zeolite and, possibly, chert formation. Below the black shale unit, low silica concentrations may be attributed either to the absence of such material or to transformation of biogenic silica into opal-CT or even quartz (Gieskes, 1983; Dixit et al., 2001). The clay-rich unit below the black shales also serves as a sink for potassium (Fig. F16D), which is taken up by clay minerals during later diagenesis.

F17. Sr vs. Mg and Cl vs. Li, p. 59.

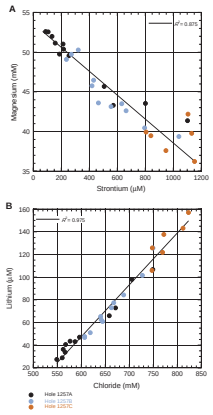

Lithostratigraphic Unit IV as an Aquifer for Brines

Another very prominent feature of the interstitial water chemistry at Site 1257 is the increase in chloride concentration with depth (Fig. F16A–F16C). This increase is paralleled by sodium, leading to an average Na/Cl ratio of 0.85, which is very close to the International Association for the Physical Sciences of the Oceans (IAPSO) seawater value of 0.86. It is important to note that the maximum in salt content is located at ~200 mbsf in lithostratigraphic Unit IV. The decrease in chloride below the black shale sequence indicates that the brine is not sourced from below the section drilled at Site 1257. Instead, the brine appears to be confined to Unit IV, which we thereby interpret to act as an aquifer for brine derived elsewhere. We cannot exclude the possibility that a fraction of the lithium and boron (Fig. F16L, F16M) is also associated with this brine. The very pronounced correlation of lithium and chloride (Fig. F17B) indicates a close association of these two parameters.

The interstitial water profiles from this site primarily reflect ongoing organic matter diagenesis in the black shales, carbonate diagenesis, and the dissolution of biogenic silica. In contrast to the previous interpretation of the existence of an underlying deep-seated evaporite sequence

at Site 144 (Waterman et al., 1972), we believe that lithostratigraphic Unit IV may act as an aquifer for relatively high salinity fluids that are sourced elsewhere.

PHYSICAL PROPERTIES

Physical property measurements at Site 1257 were conducted on whole cores, split cores, and discrete samples. GRA bulk density, magnetic susceptibility, resistivity, and NGR were measured on whole cores with the MST. Split-core analysis included *P*-wave velocity, and discrete samples were analyzed for moisture and density (MAD) (index) properties. A full description of the various measurement techniques can be found in **"Physical Properties,"** p. 33, in the "Explanatory Notes" chapter. Three acoustic velocity measurements per section were made, whereas one MAD sample per section was taken for cores from Holes 1257A and 1257C and one per core through most of Hole 1257B. Physical property sampling was minimal through the Cretaceous shale sequence (170–230 mbsf) and across critical boundaries.

Density and Porosity

The index properties determined on discrete samples include bulk density, dry bulk density, porosity, grain density, water content, and void ratio (Table **T20**). Downhole trends in these parameters reflect consolidation and lithologies, with divisions between lithostratigraphic units and subunits delineated by obvious offsets in physical property curves (Fig. **F18**). An increase in variability of the data set at 45 mbsf coincides with a change in coring technique from APC to XCB coring. It is difficult to discern whether this increase in variability is real or an artifact from (1) drilling-induced disturbance, (2) disturbance from the splitting saw used on XCB cores, or (3) accidental inclusion of drilling slurry in discrete samples.

Good agreement exists between density and porosity determined on discrete samples (MAD) and those derived from the MST GRA measurements for all holes (Fig. **F19**). GRA estimates, however, are consistently lower than the MAD determinations in Holes 1257B and 1257C as a result of the smaller-diameter cores associated with RCB drilling. XCB coring in Hole 1257A induced intense biscuiting that affected GRA density data, making correlation with Holes 1257B and 1257C relatively uncertain. Additionally, instrument problems caused a systematic error in the GRA bulk density measurements throughout Hole 1257A. The error was estimated as the best-fit equation of the difference between MAD and GRA bulk density (error = 0.18849 + 0.000287 mbsf). The plotted GRA bulk density was corrected accordingly (Figs. **F18, F19**).

At Site 1257, bulk density generally increases downhole, with noticeable offsets at contacts between lithostratigraphic units (Fig. **F19**). The thin veneer of upper Neogene sediments, classified as Unit I, is represented by a single bulk density measurement of 1.59 g/cm³ and a corresponding porosity of 65.5%. Similarly, the nannofossil ooze of Subunit IIA has an average bulk density of 1.59 g/cm³ and an average porosity of 65.2%. An average bulk density of 1.61 g/cm³ and a porosity of 63.7% characterizes a gradual transition into Subunit IIB. A maximum in bulk density and a minimum in porosity toward the base of Subunit IIB (60–85 mbsf) mark a gravity flow. Subunits IIIA and IIIB have average bulk densities of 1.76 and 1.80 g/cm³ and porosities of 54.9% and 50.8%, re-

T20. Index properties of discrete samples, p. 107.

F18. Bulk density, grain density, and porosity, p. 60.

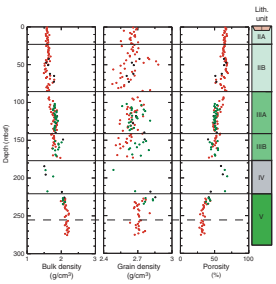

F19. MAD vs. MST GRA density, p. 61.

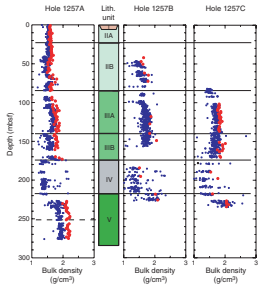

spectively. Unit IV, representing the interval of Cretaceous shale, was poorly sampled in all holes. Six MAD samples were taken through this highly variable interval, with bulk densities ranging from 1.5 to 1.9 g/cm³ and porosities from 40% to 70%. The deepest lithologic division (Unit V) has an average bulk density of 2.14 g/cm³ and a corresponding average porosity of 33.6%. Although Unit V is classified as a single unit, the index property trends clearly change at ~255 mbsf, passing from gradually increasing density and decreasing porosity to an interval of relatively constant values.

The grain density trend is relatively flat in Unit I through Subunit IIIB; however, variability in these units is quite high (Fig. F18). The largest offset in grain density occurs across the Subunit IIB/IIIA boundary, which represents the division between the Eocene and Paleocene. Grain density decreases with depth across the Subunit IIA/IIB and IIIA/IIIB and Unit IV/V boundaries. Unit IV has characteristically low grain densities typical of organic-rich material, with three of the six samples between 2.2 and 2.4 g/cm³. Unit V has the highest grain density, with an average of 2.71 g/cm³. Grain density decreases at the top of Unit V and remains constant to the bottom of the hole.

Acoustic Velocity

P-wave velocity was measured on split cores using the modified Hamilton Frame apparatus. Acoustic velocities tend to increase downhole with peaks occurring in overconsolidated or lithified intervals, especially throughout Unit IV (Fig. F20A). The highly fractured and porous shale sequences tended to be drained of water, which prevented successful measurement of velocity.

Laboratory measurements of velocity (Table T21) show a high degree of alignment with downhole logging data, with residual offsets indicating some degree of rebound in the core (Fig. F20B). The largest systematic offset after correction is found in the upper part of Unit V. A distinct change in acoustic velocity occurs between the upper and lower parts of Unit V and coincides with changes in density and porosity profiles (Fig. F18). The paucity of measurements through the upper portion of Unit V results from partially saturated sediments, which prevents successful acquisition of velocity measurements.

F20. Velocity measurements, p. 62.

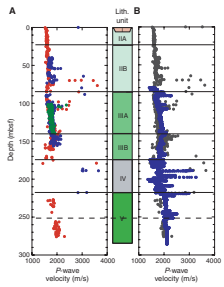

T21. Velocity measurements, p. 110.

Whole-Core Multisensor Track Data

The MST data set was successfully correlated between Holes 1257B and 1257C. Correlation of MST data between these two holes and Hole 1257A was more difficult because XCB coring in Hole 1257A caused intense biscuiting, resulting in a degraded data set (see "Composite Depths," p. 20). However, in all three holes, magnetic susceptibility, resistivity, and NGR measurements tend to reflect the larger lithologic divisions (Fig. F21).

The most pronounced changes in MST data for Holes 1257B and 1257C occur across the K/T boundary (Subunit IIIA/IIIB), where a large hiatus exists. A gradual increase in magnetic susceptibility is observed throughout Subunit IIIA, culminating in a peak at the boundary with Subunit IIIB. The increase in magnetic susceptibility is mirrored by a less pronounced rise in NGR emissions and a subsequent drop at the same boundary.

A similar trend in the MST data is observed in Hole 1257A, with the exception that the highest sustained magnetic susceptibility readings

F21. MST data, p. 63.

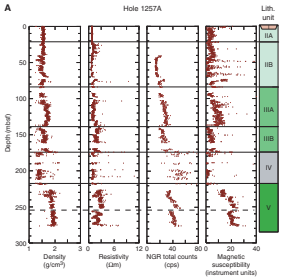

occur at 250 mbsf. This change is matched by a rise in NGR values and is coincident with a drop in carbonate content (see "Lithostratigraphy," p. 4).

Low recovery in Unit IV precludes the tracking of any systematic changes throughout the shale interval. However, the low-density, high-NGR, and low-susceptibility signature of the sequence is quite pronounced. Average GRA densities are <1.5 g/cm^3, with NGR readings >80 cps near the top of the unit and ~40 cps near the bottom.

DOWNHOLE LOGGING

Following completion of APC and XCB coring operations in Hole 1257A, the hole was conditioned with a wiper trip and pumped with sepiolite mud. The drill pipe was initially set at 84 mbsf and pulled for all logging passes to 74 mbsf. The following three tool strings were run:

1. The triple combo, with the Lamont-Doherty Earth Observatory Temperature/Acceleration/Pressure (TAP) tool and Multi-Sensor Spectral Gamma Ray Tool (MGT),
2. The FMS-sonic, and
3. The WST for a checkshot survey.

See "Downhole Logging," p. 39, in the "Explanatory Notes" chapter, for further tool specifications.

The wireline heave compensator (WHC) was used on all passes, with heave varying between 1.2 and 1.3 m throughout the operation. The first tool string run was the triple combo, which was successfully lowered to the bottom of the hole at 288 mbsf logging depth (drillers depth = 284.7 mbsf). Two full upward passes were made with the triple combo tool string. Following the trips, control of the wireline passed to the downhole measurements laboratory (DHML) and the MGT was powered up and stabilized in the pipe. Two full passes (the bottom of the hole was reached during both) were made with the MGT. The second tool string, the FMS-sonic, was successfully run to the bottom of the hole, although pump pressure was required for the tool to exit the pipe on both passes. Two full passes were made with the tool string. Because of the reduced telemetry requirements of the Long Spacing Sonic (LSS) tool, it is possible to run this tool string at 548.6 m/hr (normal logging speed when running the FMS with the Dipole Sonic Imager [DSI] is 274 m/hr). To check data quality, the first pass of the tool string was at 274 m/hr and the second was at 548.6 m/hr, which is the maximum for the FMS. The final tool string, the WST, was also successfully run to the bottom of the hole. Eight checkshot stations were acquired at a spacing of ~30 m, except for the top interval, which was shorter because of pipe proximity.

In summary, three tool strings were run during the logging operation, with seven separate logging passes. All passes were from total depth into pipe, providing a logged section of 210 m (Fig. F22). The wireline depth to seafloor was set at 2962 mbsl, determined from the step increase in gamma ray counts found at the sediment/seafloor interface recorded on the first pass of the triple combo. The drillers depth to seafloor was 2951 mbsl. A discrepancy exists between the drillers pipe and total depths (70 and 284.7 mbsf, respectively) and the wireline depths (taken here as 74 mbsf for the pipe and 288 mbsf for total depth).

F22. Summary of logging runs, p. 66.

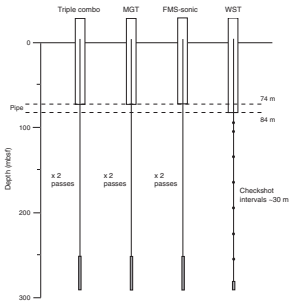

Data Quality

Borehole diameter can affect the response of some tools, for example, the Hostile Environment Litho-Density Tool (HLDT) and Accelerator Porosity Sonde (APS), and so the size and shape of the borehole is important for interpreting the quality of logging data. The caliper logs from the triple combo (one per pass) and the FMS-sonic (two per pass) tool strings provide information on the borehole size. These logs are presented in Figure F23. From the pipe (74 mbsf) down to 110 mbsf, the hole diameter is variable but always less than the maximum extension of the FMS calipers (15.5 in). From 110 down to 170 mbsf, the borehole is elliptical, extending to just under the maximum extension width of the FMS caliper arms. The FMS caliper-2 data from both passes (FMS C2 in Fig. F23) indicates hole enlargements at 83, 92.6, 102.2, 111.8, 121.5, 131.1, 140.7, and 150.3 mbsf, which correspond to the bottom of Cores 207-1257A-10X to 17X. These data indicate borehole enlargement resulting from incomplete active heave compensation of the drill pipe, which is exacerbated during core barrel recovery and reload. Any time-series analysis on logging data through this interval that shows cycles corresponding to 9- to 10-m wavelengths should be suspect. At 170 mbsf, the borehole narrows and maintains a uniform diameter, punctuated only by a few minor washouts/breakouts. Below 245 mbsf, the hole narrows further to just beyond bit size. The borehole conditions, as indicated by the caliper logs, were very good. The WHC was run on all the passes, except for the WST tool, when it is not required.

Data from the triple combo tools are good, with excellent repeatability and only minor depth mismatches between passes. Gamma ray data from the Hostile Environment Gamma Ray Sonde (HNGS), MGT, and Scintillation Gamma Ray Tool (SGT) are also well matched in depth and magnitude, providing easy depth shifting for the MGT and FMS logging passes. FMS-sonic data are good for the logged sections, showing excellent repeatability between passes.

Core physical property data provide a rapid method for visualization of the core-log correlation (Fig. F24). The depth match between logging mbsf and core (drillers) mbsf is good. Elastic rebound and temperature changes following drilling and recovery of the core can affect the core index properties of density and porosity and, thus, velocity (Hamilton, 1976). A small offset of density and velocity values observed in core measurements vs. logging values may be related to this effect. No consistent pattern is observed in the resistivity data. Core-measured gamma ray values underestimate the in situ values. Overall, the patterns observed in the core physical properties are well matched to the logging data, suggesting postcruise core-log depth matching should be straightforward.

Logging Stratigraphy

Four logging units were defined for Hole 1257A.

Unit 1 (base of pipe [74 mbsf]–87 mbsf)

This unit is best defined in the porosity and velocity logs and, to a minor degree, in the density logs. Porosities are higher than the unit below and fluctuate rapidly (Figs. F24, F25). The velocity logs show a step increase of 250 m/s across the lower boundary of the unit (Figs. F24, F25). Density increases through the short section recorded by the

F23. Borehole caliper logs, p. 67.

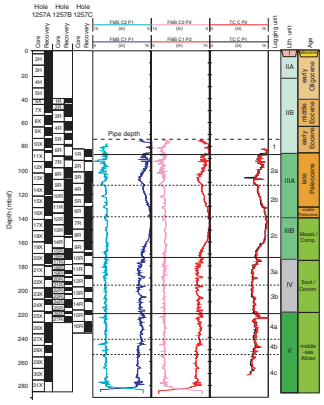

F24. Geophysical logs and physical properties, p. 68.

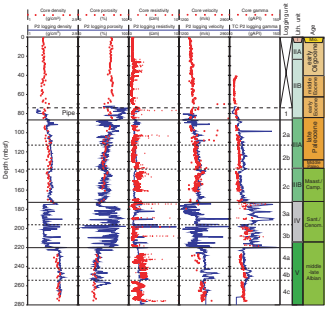

F25. Geophysical logs, caliper data, and logging units, p. 69.

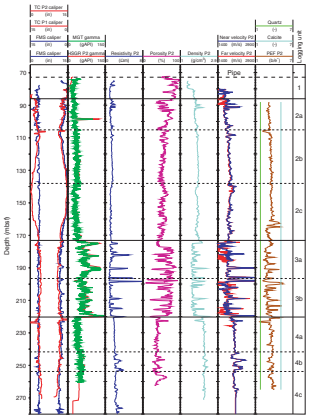

HLDT. This logging unit corresponds to the lowest part of lithostratigraphic Subunit IIB (see "Lithostratigraphy," p. 4) and the early Eocene (see "Biostratigraphy," p. 11).

Unit 2 (87–173 mbsf)

Overall, this unit is characterized by low-amplitude cyclic fluctuations in gamma ray, resistivity, porosity, density, and velocity (Fig. F25) and has been further subdivided into three subunits based on downhole gradient changes in physical properties.

Subunit 2a (87–112.5 mbsf)

The top of this unit is clearly defined by a change in the resistivity, porosity, density, and velocity logs. High-amplitude variation in the data characterizes the unit. A shallow, increasing-downhole gradient in gamma ray, resistivity, density (covaries with porosity), and velocity is apparent (Fig. F26). This trend is interpreted to represent decreasing carbonate content (see "Organic Geochemistry," p. 22, and "Lithostratigraphy," p. 4) and increasing clay content downhole in the unit. The downhole increase in density is also indicated by the caliper logs (Fig. F23) as a narrowing of the hole diameter, presumably resulting from the increase in strength of the formation.

Subunit 2b (112.5–138 mbsf)

Logging Subunit 2b is characterized by lower-amplitude, shorter (depth)-period cycles in porosity, density, velocity, and resistivity but is best seen in the gamma ray logs. Increasing-downhole trends in density (covarying with porosity) resistivity, velocity (Fig. F26), and gamma ray (Fig. F25) values continue, but the gradient is slightly reduced. The caliper logs show the borehole widening downhole throughout this unit, suggesting that despite increasing density the sediment may be softer with depth. This trend may be explained by a small increase in clay content with depth combined with consolidation effects producing a density increase, but the higher clay content mechanically weakens the formation.

Subunit 2c (138–173 mbsf)

The top of this unit is defined by a peak, followed by a decline in the gamma ray and density (covarying with porosity) logs, and a velocity peak is observed just below the boundary (Figs. F25, F26). After the minimum is reached, values increase slowly toward the bottom of the unit, regaining the levels they had at the top. The logging Subunit 2b/3c boundary correlates with the lower Paleocene/lower Maastrichtian hiatus (see "Biostratigraphy," p. 11) and lithostratigraphic Subunits IIIA and IIIB (see "Lithostratigraphy," p. 4). Despite the drop in density at the top of the unit, the caliper logs indicate the borehole narrowing downhole, suggesting increasing strength resulting from cementation with depth.

Unit 3 (173–220 mbsf)

Logging Unit 3 is characterized by a large step increase in the gamma ray, resistivity, and porosity logs, with a concomitant decrease in the density and velocity logs. The gamma ray spectrum (Fig. F27) reveals the source of increased gamma ray emission to be potassium (clay) and uranium (organic matter). Large-amplitude fluctuations are observed in all the logs. These fluctuations are interpreted to result from the peri-

F26. Logging Units 1 and 2, p. 70.

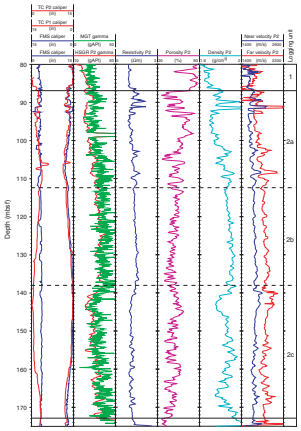

F27. High-resolution MGT gamma ray logs, p. 71.

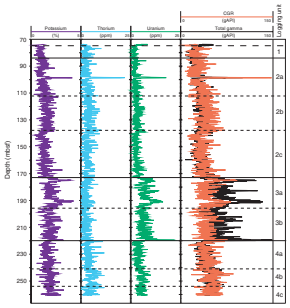

odic presence of cemented layers, giving peaks in density (troughs in porosity), resistivity, and velocity, and are highlighted in the FMS resistivity images (Fig. F28). The photoelectric effect (PEF) log indicates that the cement in these layers is calcite (photoelectric absorption cross-section index [*Pe*] = 5.08 b/e⁻ for calcite) (Fig. F28). The high organic content indicated by the uranium contribution to the gamma ray spectrum is corroborated by correlation of logging Unit 3 with lithostratigraphic Unit IV, black shale (see "Lithostratigraphy," p. 4, and "Organic Geochemistry," p. 22). The unit is further subdivided into two subunits based on the gamma ray logs (Fig. F27).

F28. Geophysical logs and FMS imagery, p. 72.

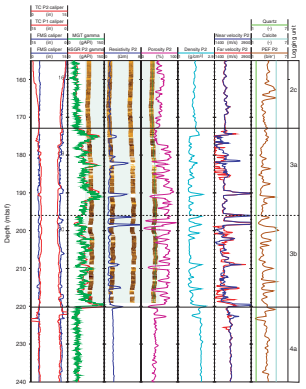

Subunit 3a (173–196 mbsf)

Logging Subunit 3a is characterized by three well-defined high-amplitude cycles in the gamma ray logs. The cyclic fluctuations are the result of synchronously varying potassium and uranium contributions (Fig. F27).

Subunit 3b (196–220 mbsf)

Uranium and potassium and, thus, total gamma ray counts decrease in logging Subunit 3b. Cycles in this subunit have a higher frequency (smaller depth range) and lower amplitude than cycles in logging Subunit 3a above. The base of the unit is defined by a sharp peak in total gamma ray counts that is dominated by uranium contribution, indicating a very organic-rich horizon (Fig. F27).

Unit 4 (220 mbsf–total depth [288 mbsf])

Logging Unit 4 is characterized by consistently high density (low porosity), resistivity, and velocity values recorded through the formation (Fig. F25), discounting the carbonate-cemented layers highlighted in logging Subunit 3a above. The unit has been subdivided into three subunits.

Subunit 4a (220–241.5 mbsf)

Density, resistivity, and velocity increase gradually in this unit, with only small-amplitude variations recorded. However, a spike in the PEF log, correlated with porosity and velocity peaks and a density trough, indicates a concentration of quartz at 223 mbsf. This horizon correlates with a calcareous sandstone layer identified in Holes 1257B and 1257C (see "Lithostratigraphy," p. 4). The PEF log indicates another calcareous sandstone layer at 237.5 mbsf (Fig. F25).

Subunit 4b (241.5–254 mbsf)

Three distinct peaks in resistivity and velocity combined with a step to higher gamma ray values characterize this subunit. The two lower peaks correlate with peaks in the density, porosity, and PEF logs and the FMS images and probably represent calcareous cemented sandstone layers. Total gamma ray counts are higher due to an increased contribution from both thorium and uranium.

Subunit 4c (254–288 mbsf)

Only short intervals of data from most tools are available for this subunit. Resistivity, density, and velocity values return to levels similar to logging Subunit 4a above. Gamma ray counts, however, remain similar to the levels in logging Subunit 4b, indicating the continuing presence of organic material (see "Organic Geochemistry," p. 22). Two peaks at the bottom of the resistivity log (Fig. F25) correspond to bright

resistive layers in the FMS imagery and are interpreted to represent cemented layers, probably comprising calcareous-cemented sandstone similar to that found in logging Subunits 4a and 4b, described above.

Discussion

Good hole conditions combined with low heave led to the acquisition of excellent logging data. For the most part, the logging units described above correlate well with the designated lithostratigraphic units (see "Lithostratigraphy," p. 4). However, a few further points of interest shall now be addressed.

Black Shale

The continuous data derived from the logs through the black shale interval (logging Unit 3) provides the opportunity for estimation of the TOC content in this unit. The result is only approximate because the shale porosity is assumed to equate to that of the sediments above and values for some densities (e.g., organic matter) that are not well constrained are also assumed. Following Rider (1996), the following three equations are used to calculate the TOC:

$$\phi_{fl} = (\rho_{bk} - \rho_{ma})/(\rho_{fl} - \rho_{ma}),$$

$$\phi_{om} = (\rho_{bs} - \rho_{bk})/(\rho_{om} - \rho_{ma}), \text{ and}$$

$$\text{TOC (wt\%)} = ([0.85 \times \rho_{om} \times \phi_{om}]/[(\rho_{om} \times \phi_{om}) + \rho_{ma}(1 - \phi_{om} - \phi_{fl})]) \times 100\%,$$

where

- ρ_{bk} = density of the background sediment taken from the density log (1.88 g/cm³).
- ρ_{bs} = density of the black shale interval taken from the density log.
- ρ_{om} = density of the organic matter (assumed) (1.15 g/cm³).
- ρ_{ma} = density of the matrix (grain density) averaged from five MAD measurements (2.52 g/cm³).
- ρ_{fl} = density of seawater (1.05 g/cm³).
- ϕ_{fl} = water-filled porosity.
- ϕ_{om} = volume fraction of organic matter.

The results are plotted along with values measured from core samples (see "Organic Geochemistry," p. 22) in Figure F29. Despite the fact that the measured values are from Holes 1257A, 1257B, and 1257C and are not depth matched to the logging mbsf depths, the results are very satisfactory.

Gamma Ray Peak (98.5 mbsf)

Both MGT and SGT passes and the second pass of the HNGS gamma ray tools all identified a major peak at 98.5 mbsf (Figs. F24, F25, F27). The other logs do not show evidence of a major change in physical properties. The gamma spectrum over the interval shows an increase in potassium, thorium, and uranium spectra, indicating contributions from both clay and organic matter (Fig. F30). The FMS image in Figure F30 suggests a higher-resistivity layer may be the source for the gamma

F29. Core-measured vs. log-calculated TOC, p. 73.

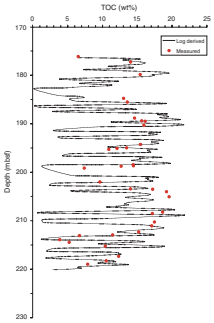

F30. MGT gamma ray logs and FMS imagery, p. 74.

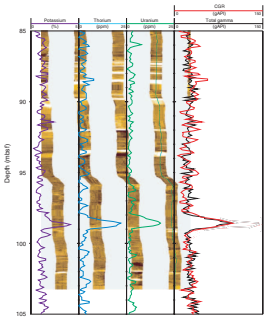

ray spike. Core was only recovered across this interval in Hole 1257B. Given the poor core recovery and slumping activity associated with the top of lithostratigraphic Subunit IIIA at 85 mbsf (see "Lithostratigraphy," p. 4), it is possible that the gamma ray spike indicates slumping extending deeper into the section, bringing allochthonous material to the site from upslope.

Hole Enlargement in Logging Unit 2

During the description of logging Subunit 2b, mention was made of the counter-intuitive borehole widening as formation density increased. The gamma ray spectrum through this interval (Fig. F27) indicates that the increased gamma count results from a higher level of potassium. The step change in total gamma at the base of the unit and concomitant borehole narrowing is matched by a reduction in potassium counts. The uranium and thorium spectra show little change between logging Subunits 2b and 2c. One possible explanation for the formation softening is higher levels of illite (highest in potassium of the clays) in logging Subunit 2b, with a step change into logging Subunit 2c. Despite the decrease in density at the top of logging Subunit 2c, the borehole begins to narrow, suggesting perhaps better cementation associated with the hiatus between the lower Maastrichtian and lower Paleocene represented by the logging Subunit 2b/2c boundary.

Temperature Perturbation

The temperature record from the TAP tool must be interpreted with caution because the borehole has probably not reached thermal equilibrium following circulation of the drilling fluid. Nevertheless, abrupt temperature changes representing localized fluid flow into the borehole may be identified. The borehole temperature profile recorded on the first logging-downhole pass of the TAP tool (it is located on the bottom of the triple combo tool string) is shown in Figure F31. Pipe effects are clearly obvious to 90 mbsf. From 90 to 128 mbsf, there is a steep temperature gradient, indicating mixing between the cold pipe and warmer borehole fluids. What is interpreted to represent a more realistic formation borehole temperature begins at 138 mbsf and extends to the bottom of the hole. There is a clear perturbation (inflow of cooler fluid) in the temperature profile between 162 and 212 mbsf. This temperature perturbation is closely related to, and suggestive of, fluid flow through the black shale interval (Fig. F31). This observation provides direct supporting evidence for results from the pore water geochemistry studies (see "Inorganic Geochemistry," p. 24).

F31. Borehole temperature, p. 75.

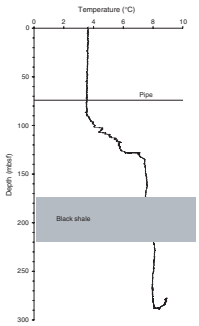

Checkshot Survey and Synthetic Seismograms

A checkshot survey was conducted during logging operations in Hole 1257A, and eight stations were collected using a series of stacked shots at 30-m intervals up the borehole (Fig. F22). The checkshot survey provides a direct measurement of root mean square (rms) acoustic traveltime (Table T22) and, thus, formation velocity. Conversion of these rms values to interval velocities allows the checkshot data to calibrate the velocity log. For most sites, the logging velocity is higher than the measured interval velocity (Fig. F32), so a correction factor of –100 m/s was applied to the velocity log. Downhole impedance (velocity × density) was calculated, and the impedance contrast between successive layers

T22. Checkshot data, p. 111.

F32. Density, velocity, impedance, and reflection profiles, p. 76.

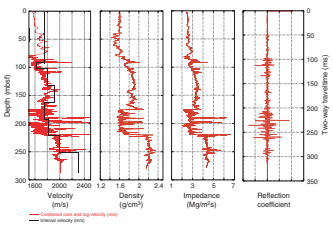

gave the reflection coefficient series. An Ormsby wavelet was convolved with the reflection coefficient series to generate the synthetic seismograms (Fig. **F33**).

The synthetic seismogram accurately matches the seismic data, which allowed the regional B, B′, and C reflectors to be reinterpreted. Contrary to previous interpretations of the seismic data, Reflector C represents the base of the black shales, unconformably overlying the middle–upper Albian synrift sediments. Reflector B′ is the top of the black shales (173 mbsf), and Reflector B is the density and velocity step at 138 mbsf (the logging Subunit 2b/2c boundary), probably representing the lower Paleocene hiatus (see **"Biostratigraphy,"** p. 11) and the contact between lithostratigraphic Subunits IIIA and IIIB (see **"Lithostratigraphy,"** p. 4).

F33. Synthetic seismogram, p. 77.

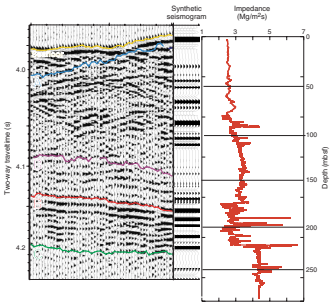

REFERENCES

Acton, G.D., Okada, M., Clement, B.M., Lund, S.P., and Williams, T., 2002. Paleomagnetic overprints in ocean sediment cores and their relationship to shear deformation caused by piston cores. *J. Geophys. Res.,* 107:10.1029/2001JB000518.

Baker, P.A., Gieskes, J.M., and Elderfield, H., 1982. Diagenesis of carbonates in deep-sea sediments—evidence from Sr^{2+}/Ca^{2+} ratios and interstitial dissolved Sr^{2+} data. *J. Sediment. Petrol.,* 52:71–82.

Benkhelil, J., Mascle, J., and Tricart, P., 1995. The Guinea continental margin: an example of a structurally complex transform margin. *Tectonophysics,* 248:117–137.

Brumsack, H.-J., 1986. The inorganic geochemistry of Cretaceous black shales (DSDP Leg 41) in comparison to modern upwelling sediments from the Gulf of California. *In* Summerhayes, C.P., and Shackleton, N.J. (Eds.), *North Atlantic Palaeoceanography.* Geol. Soc. Spec. Publ., 21:447–462.

Church, T.M., and Wolgemuth, K., 1972. Marine barite saturation. *Earth Planet. Sci. Lett.,* 15:35–44.

Claypool, G.E., and Kvenvolden, K.A., 1983. Methane and other hydrocarbon gases in marine sediment. *Annu. Rev. Earth Planet. Sci.,* 11:299–327.

Dixit, S., van Cappellen, P., and van Bennekom, A.J., 2001. Processes controlling solubility of biogenic silica and pore water buildup of silicic acid in marine sediments. *Mar. Chem.* 73:333–352.

Espitalié, J., Laporte, J.L., Madec, M., Marquis, F., Leplat, P., Paulet, J., and Boutefeu, A., 1977. Méthode rapide de caractérisation des roches mères, de leur potentiel pétrolier et de leur degré d'évolution. *Rev. Inst. Fr. Pet.,* 32:23–42.

Gieskes, J.M., 1983. The chemistry of interstitial waters of deep-sea sediments: interpretation of deep-sea drilling data. *In* Riley, J.P., and Chester, R. (Eds.), *Chemical Oceanography* (Vol. 8): London (Academic), 221–269.

Gouyet, S., Unternehr, P., and Mascle, A., 1994. The French Guyana margin and the Demerara Plateau: geologic history and petroleum plays. *In* Mascle, A. (Ed.), *Hydrocarbon and Petroleum Geology of France*. Spec. Publ.—Eur. Assoc. Pet. Geosci., 4:411–422.

Hamilton, E.L., 1976. Variations of density and porosity with depth in deep-sea sediments. *J. Sediment. Petrol.,* 46:280–300.

Hayes, D.E., Pimm, A.C., et al., 1972. *Init. Repts. DSDP,* 14: Washington (U.S. Govt. Printing Office).

Martini, E., 1971. Standard Tertiary and Quaternary calcareous nannoplankton zonation. *In* Farinacci, A. (Ed.), *Proc. 2nd Int. Conf. Planktonic Microfossils Roma:* Rome (Ed. Tecnosci.), 2:739–785.

McIver, R.D., 1975. Hydrocarbon occurrences from *JOIDES* Deep Sea Drilling Project. *Proc. Ninth Petrol. Congr.,* 269–280.

Meyers, P.A., 1997. Organic geochemical proxies of paleoceanographic, paleolimnologic, and paleoclimatic processes. *Org. Geochem.,* 27:213–250.

Müller, P.J., 1977. C/N ratios in Pacific deep sea sediments: effect of inorganic ammonium and organic nitrogen compounds sorbed by clays. *Geochim. Cosmochim. Acta,* 41:765–776.

Peters, K.E., 1986. Guidelines for evaluating petroleum source rock using programmed pyrolysis. *AAPG Bull.,* 70:318–329.

Presley, B.J., Petrowski, C., and Kaplan, I.R., 1973. Interstitial water chemistry, Deep Sea Drilling Project, Leg 10. *In* Worzel, J.L., Bryant, W., et al., *Init. Repts. DSDP,* 10: Washington (U.S. Govt. Printing Office), 613–614.

Rider, M.H., 1996. *The Geological Interpretation of Well Logs* (2nd ed.): Caithness (Whittles Publishing).

Rudnicki, M.D., Wilson, P.A., and Anderson, W.T., 2001. Numerical models of diagenesis, sediment properties and pore fluid chemistry on a paleoceanographic transect: Blake Nose, Ocean Drilling Program Leg 171B. *Paleoceanography,* 16:561–573.

Sissingh, W., 1977. Biostratigraphy of Cretaceous calcareous nannoplankton. *Geol. Mijnbouw,* 56:37–65.

Torres, M.E., Brumsack, H.-J., Bohrmann, G., and Emeis, K.C., 1996. Barite fronts in continental margin sediments: a new look at barium remobilization in the zone of sulfate reduction and formation of heavy barites in diagenetic fronts. *Chem. Geol.,* 127:125–139.

Twichell, S.C., Meyers, P.A., and Diester-Haass, L., 2002. Significance of high C/N ratios in organic-carbon-rich Neogene sediments under the Benguela Current upwelling system. *Org. Geochem.,* 33:715–722.

Waterman, L.S., Sayles, F.L., and Manheim, F.T., 1972. Interstitial water studies on small core samples, Leg 14. *In* Hays, D.E., Pimm, A.C., et al., *Init. Repts. DSDP,* 14: Washington (U.S. Govt. Printing Office), 753–762.

Figure F1. Seismic reflection line GeoB220 collected during *Meteor* site survey M49-4 across Site 1257. See Figure F1, p. 5, in Shipboard Scientific Party ("Site Survey and Underway Geophysics"), this volume. Green = Reflector C, red = Reflector B′, pink = Reflector B, blue = Reflector A. Vertical dashed red line = Site 1257.

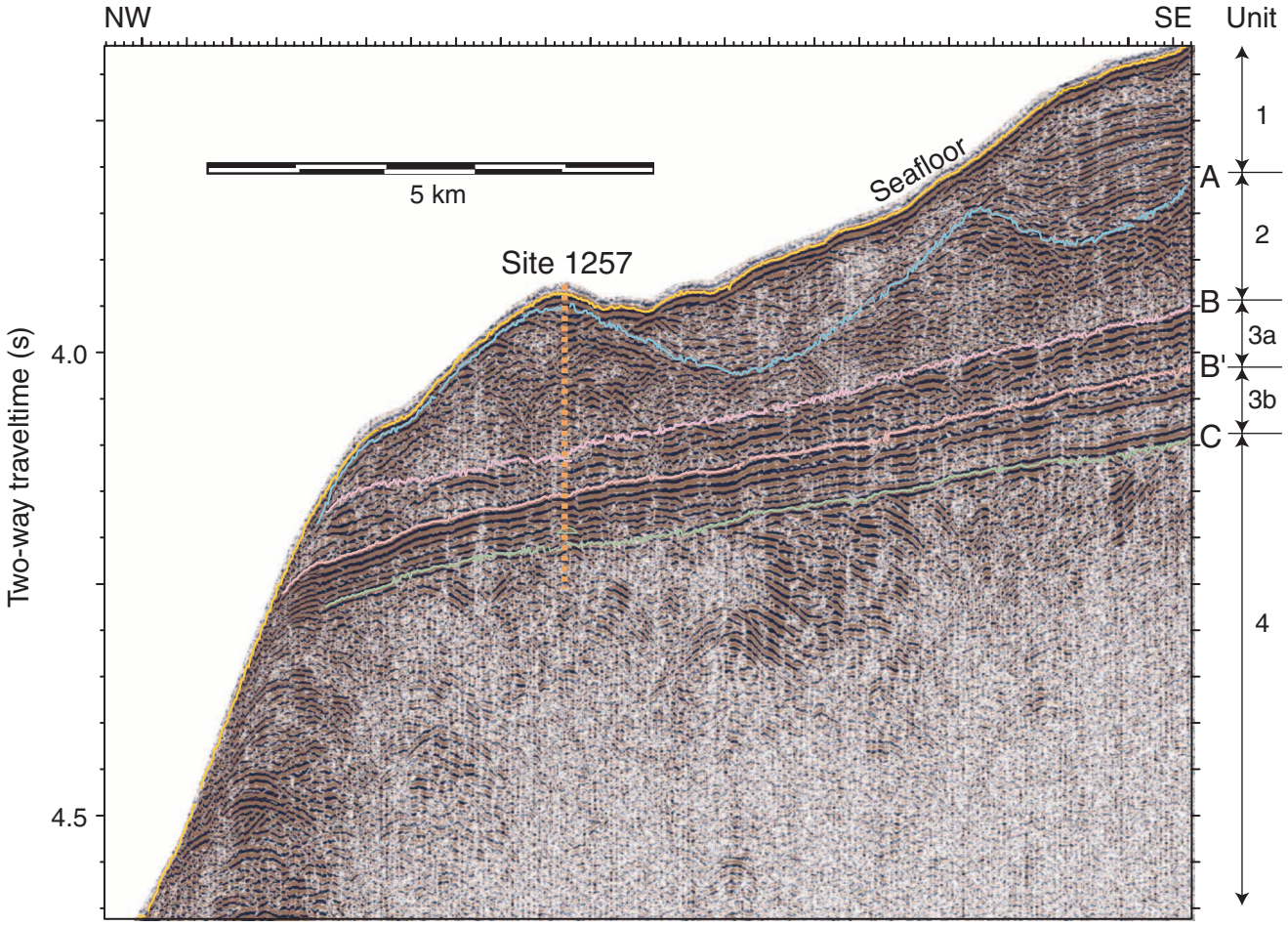

Figure F2. Comparison of recovery and lithostratigraphic units recognized at DSDP Site 144 and ODP Site 1257. TD = total depth.

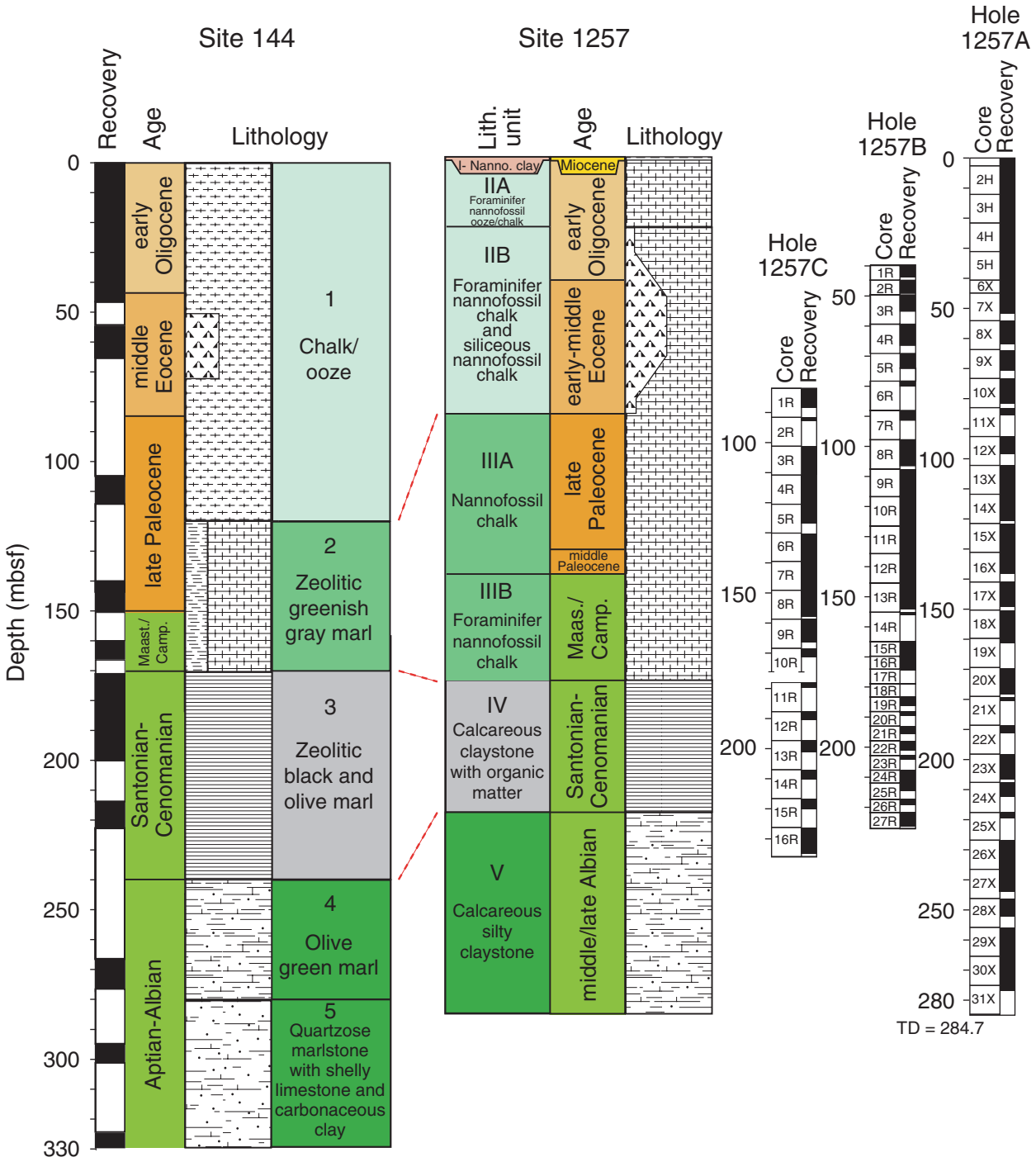

Figure F3. Close-up photographs of representative lithologies from lithostratigraphic Units I and II at Site 1257. **A.** Contact between the pale olive clay of Unit I and the pale yellow nannofossil chalk in the upper part of Unit II (interval 207-1257A-1H-2, 0–20 cm). **B.** The sharp color change, but otherwise similar lithology, of the subtly burrowed mottled dominant lithology typical of Unit II (interval 207-1257A-2H-2, 85–105 cm). (Continued on next page.)

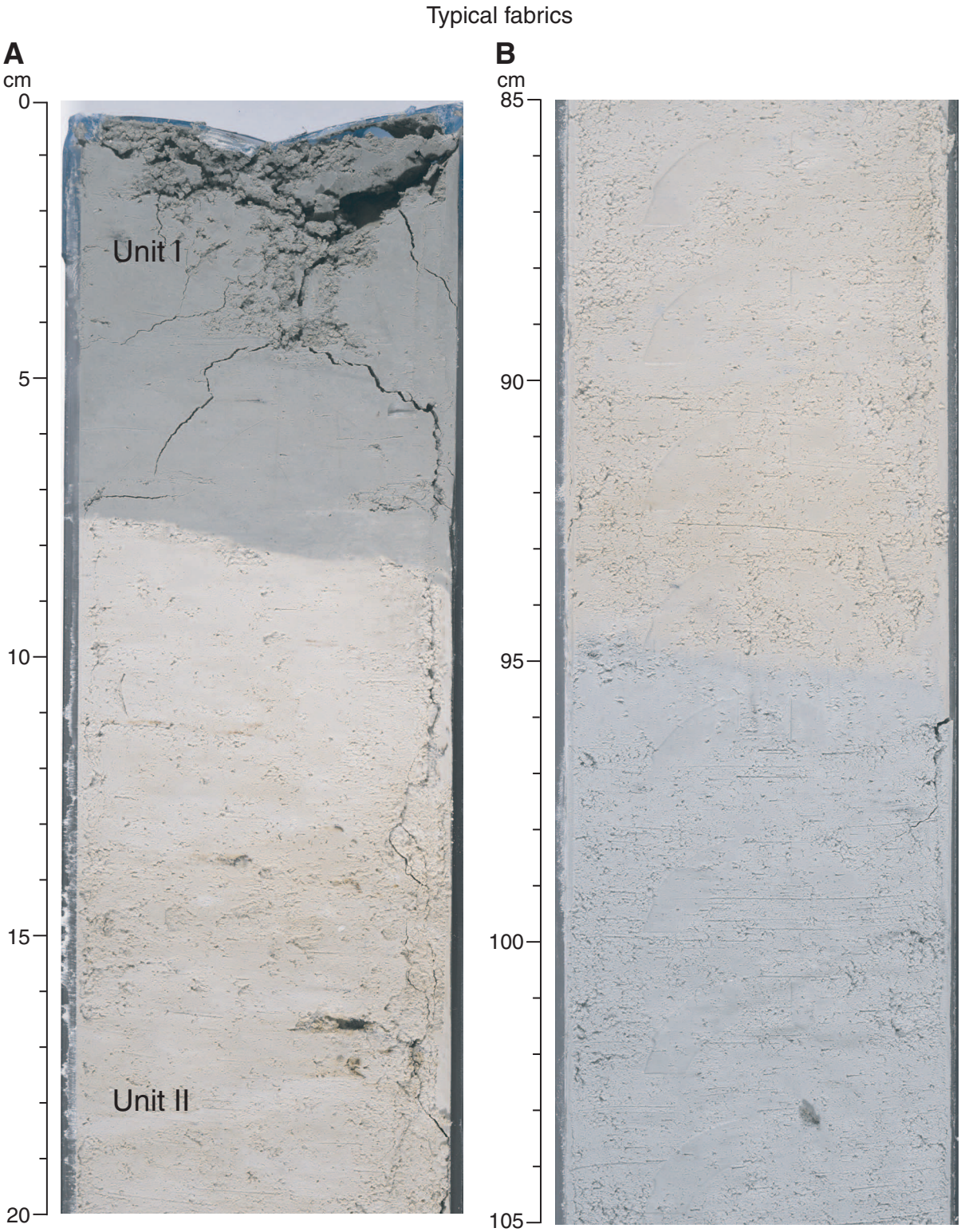

Figure F3 (continued). C. Deformation typical of gravity flow deposits (intervals 207-1257B-1R-2, 15–35 cm, and 5R-2, 25–50 cm).

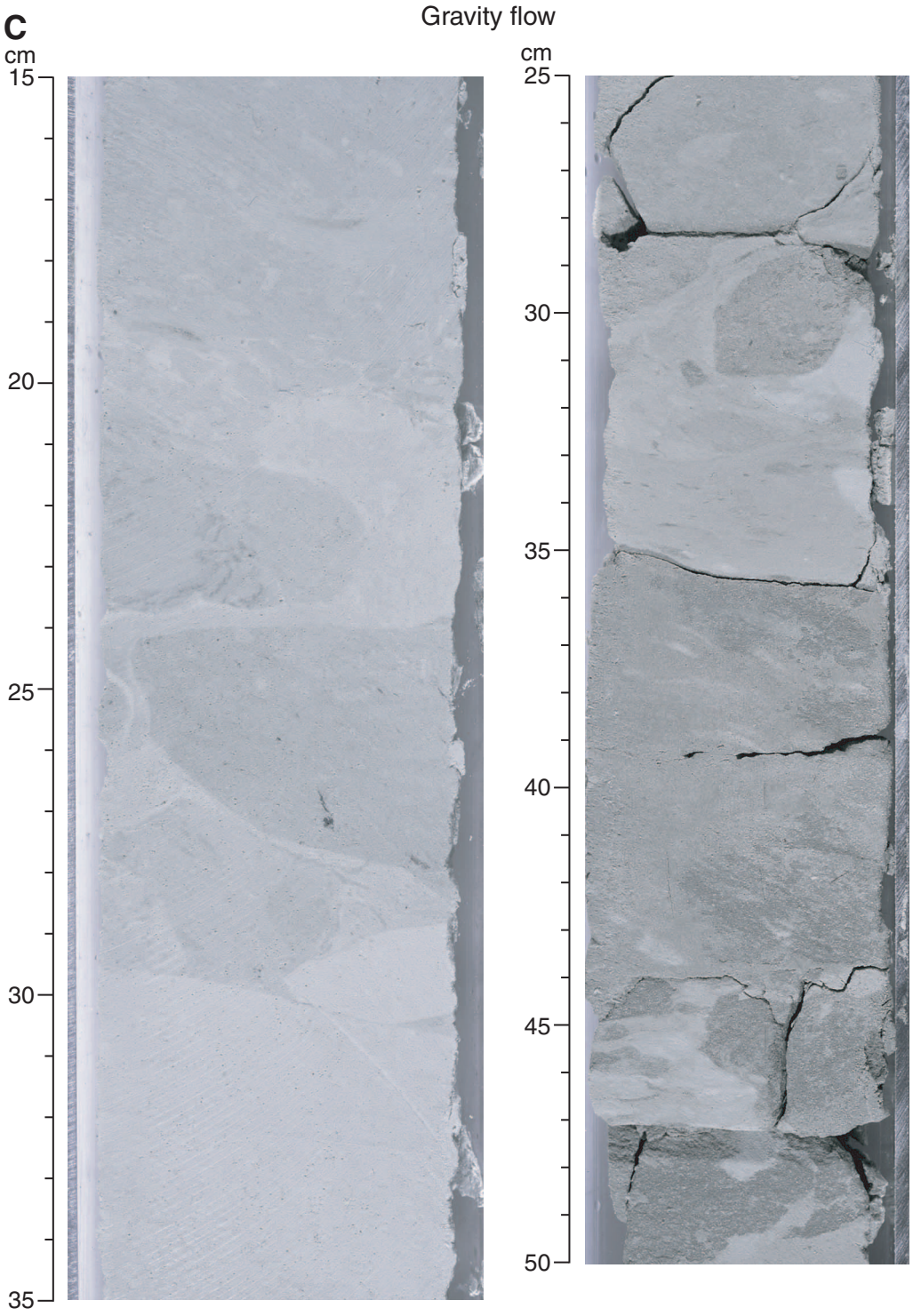

Figure F4. Carbonate and organic carbon concentrations in samples from Site 1257. TD = total depth.

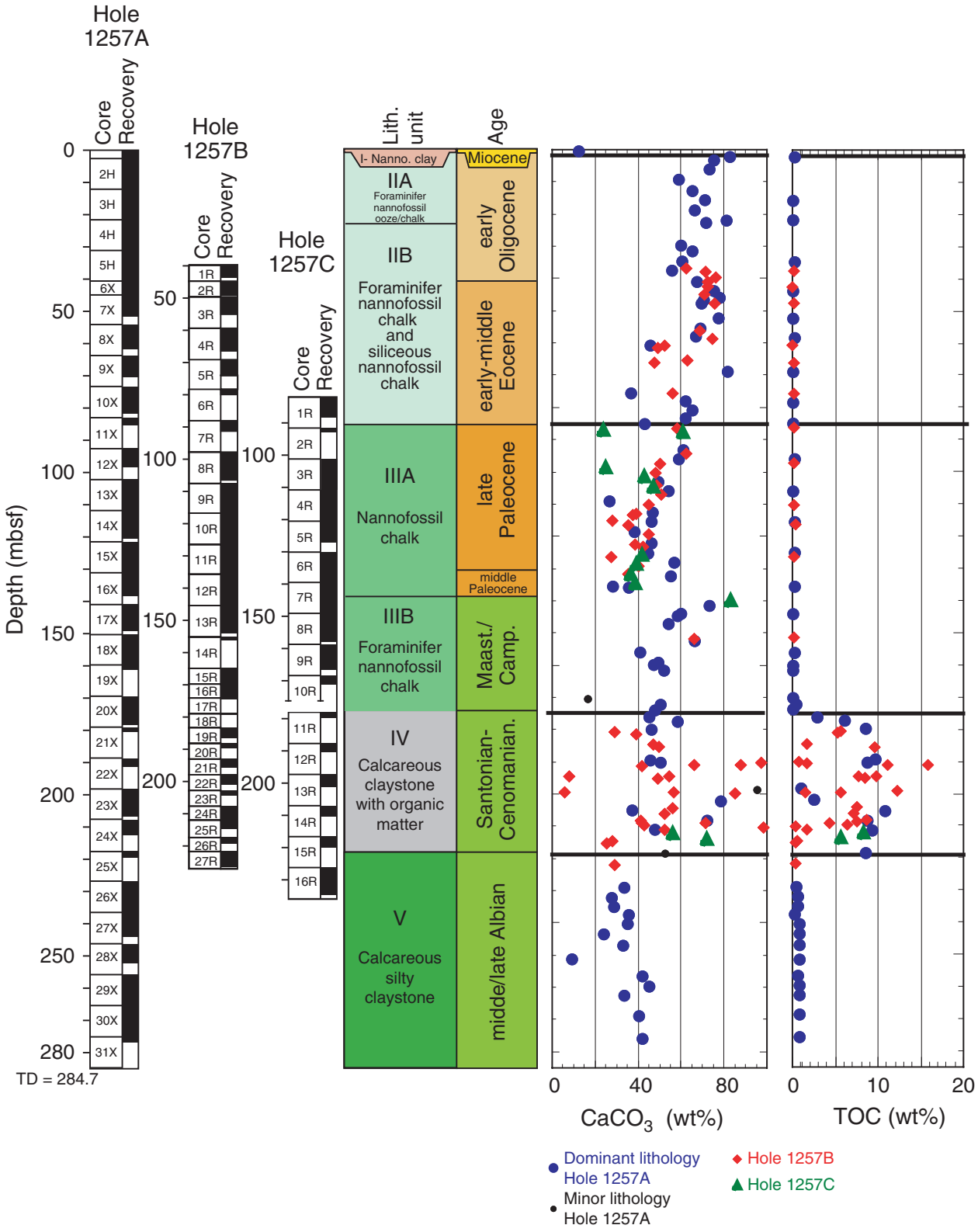

Figure F5. Close-up photographs of characteristic lithologies of pelagic sediments in Unit III. **A, B.** Burrow mottled fabric containing traces typical of the Zoophycos trace fossil assemblage; (A) interval 207-1257A-16X-2, 95–108 cm; (B) interval 1257A-17X-1, 40–55 cm. (Continued on next page.)

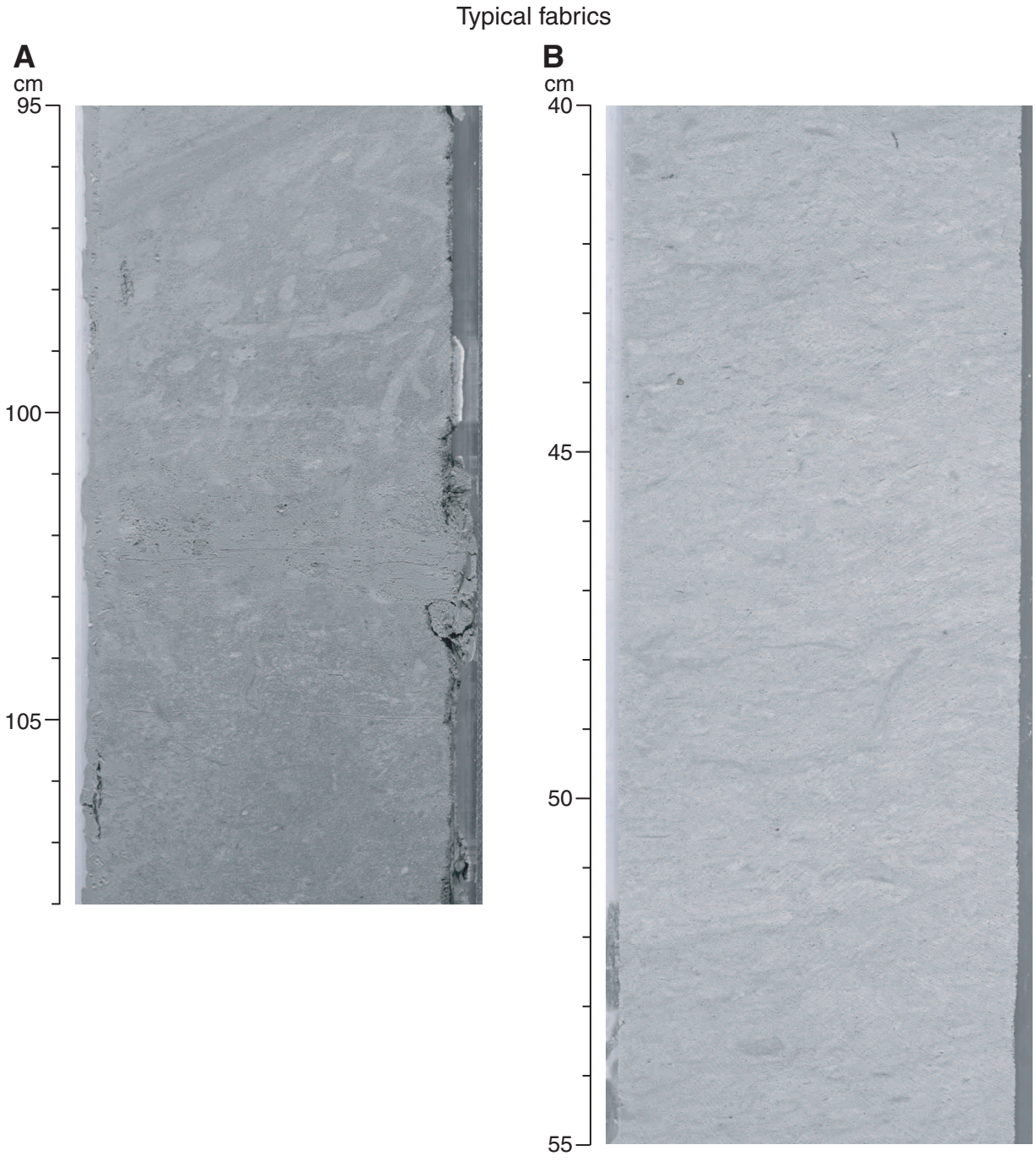

Figure F5 (continued). C, D. Portions of the gravity flow deposit at the contact between Cretaceous and Tertiary sediments. Because clasts in this deposit contain Tertiary microfossils, the deposit is not related to events that occurred at the K/T boundary; (C) interval 207-1257B-12R-5, 15–27 cm; (D) interval 207-1257B-12R-5, 115–128 cm.

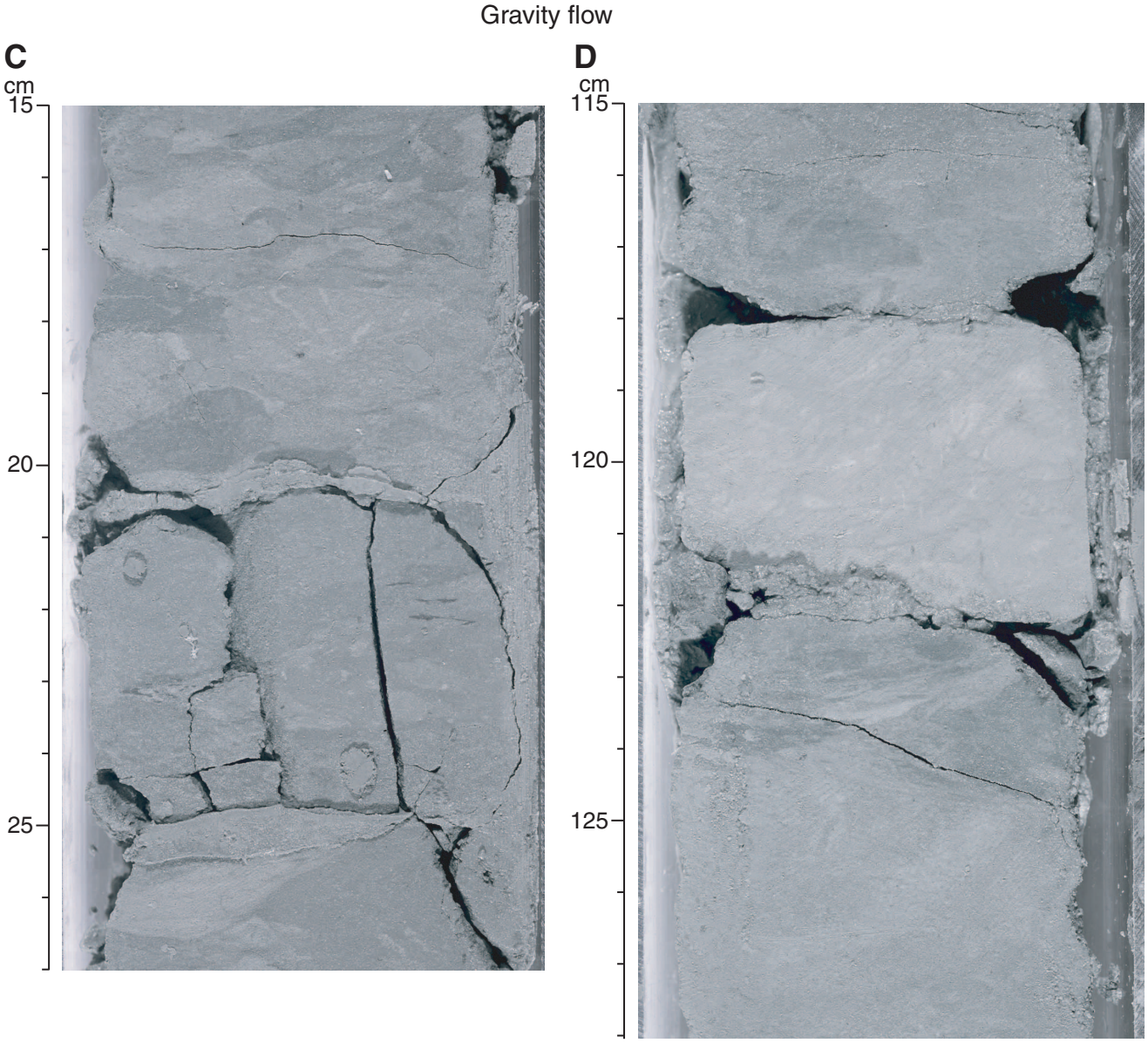

Figure F6. Close-up photographs of typical lithologies of Units IV and V. **A.** Laminations, light–dark cycles, white calcareous laminae, and tan phosphatic lenses in Unit IV (interval 207-1257C-13R-2, 9–30 cm). **B.** Laminations and a layer containing abundant fish debris at 88 cm and a small phosphatic nodule at 91 cm in Unit IV (Sample 207-1257B-25R-2, 86–92 cm). (Continued on next two pages.)

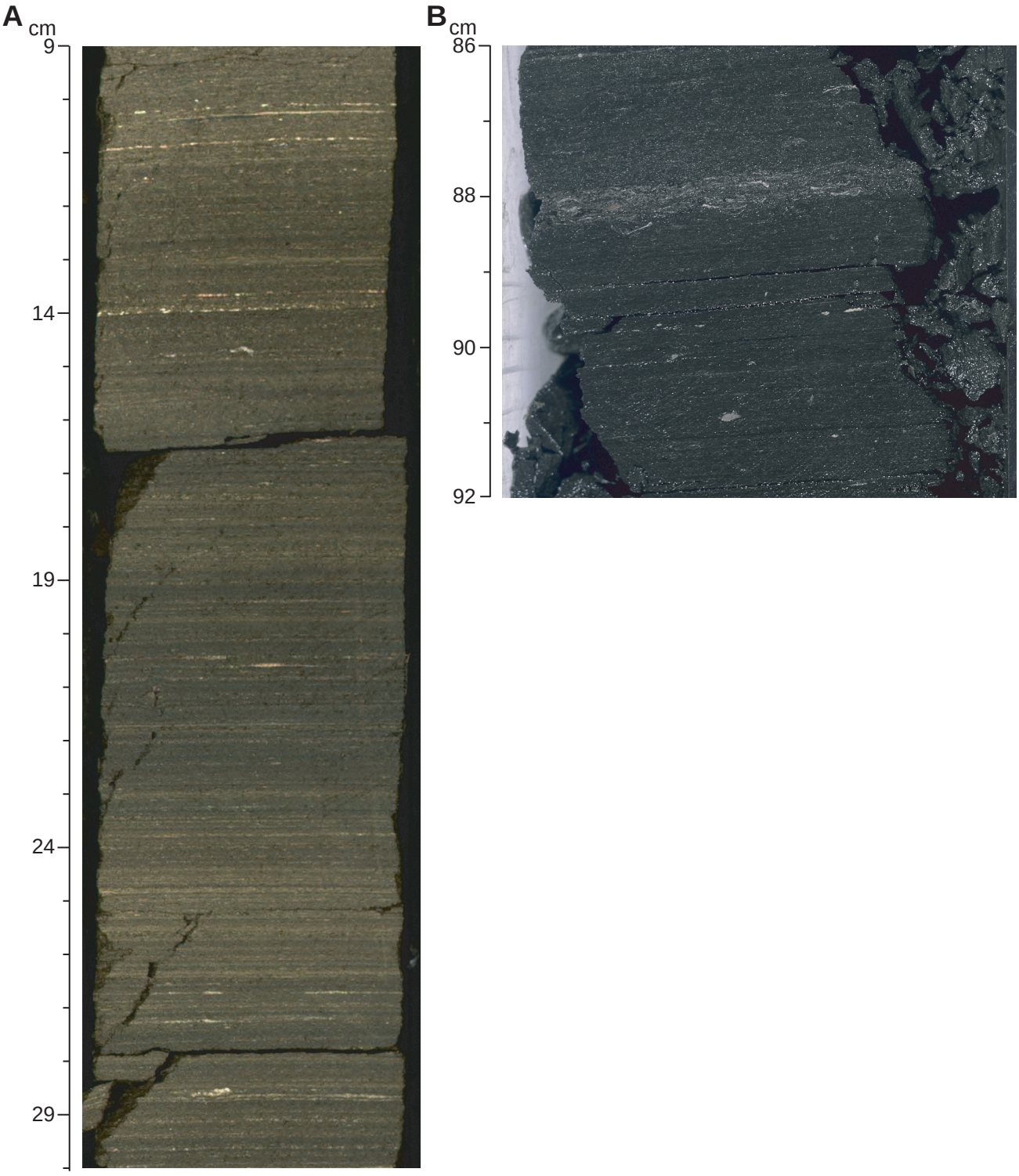

Figure F6 (continued). **C.** Typical laminated limestone in Unit IV (interval 207-1257B-25R-2, 20–40 cm). **D.** Subhorizontal wavy fabric characteristic of Unit V (interval 207-1257B-27R-3, 100–140 cm).

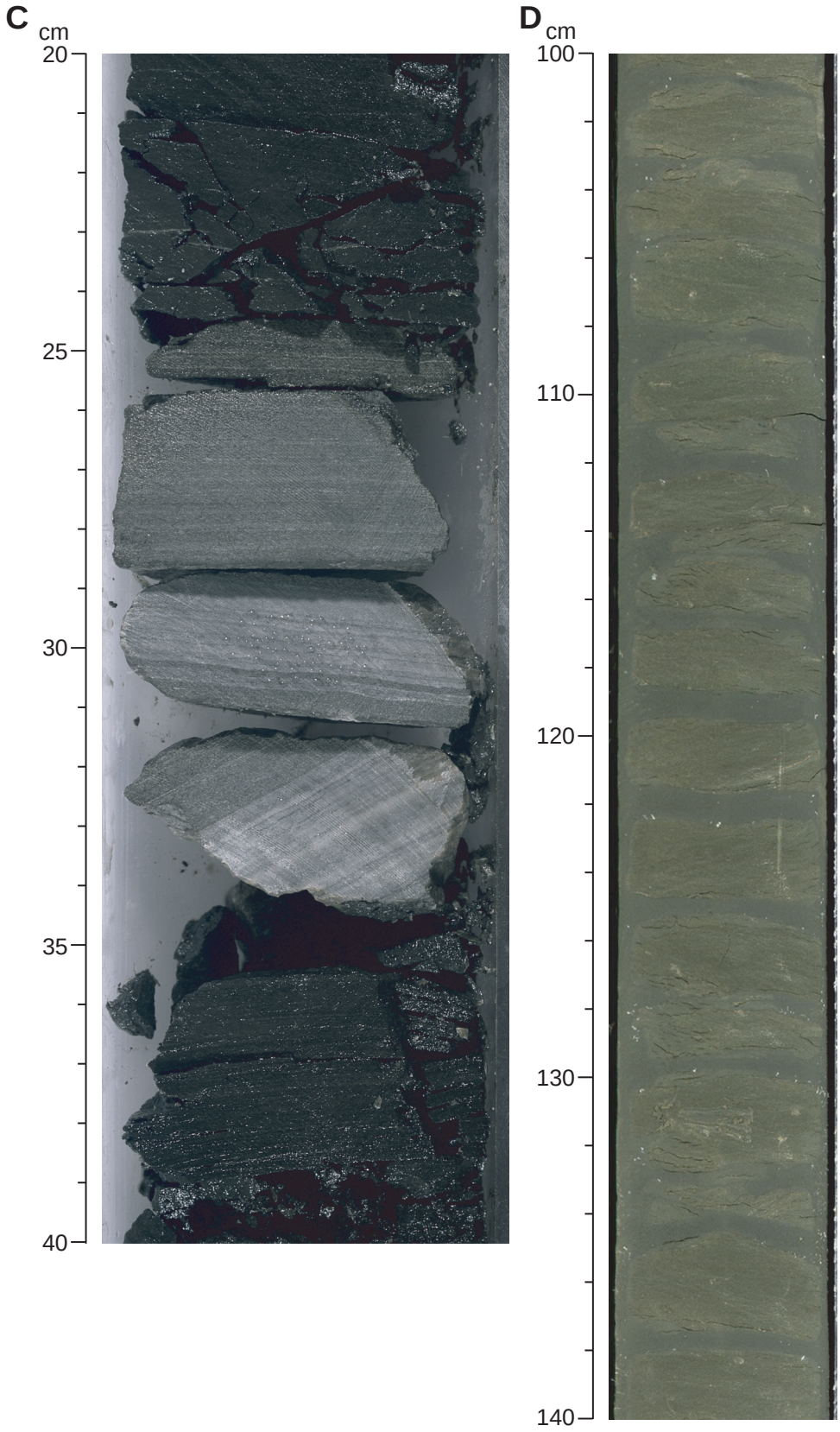

Figure F6 (continued). E. Pyrite in Unit V (interval 207-1257B-26R-3, 100–140 cm).

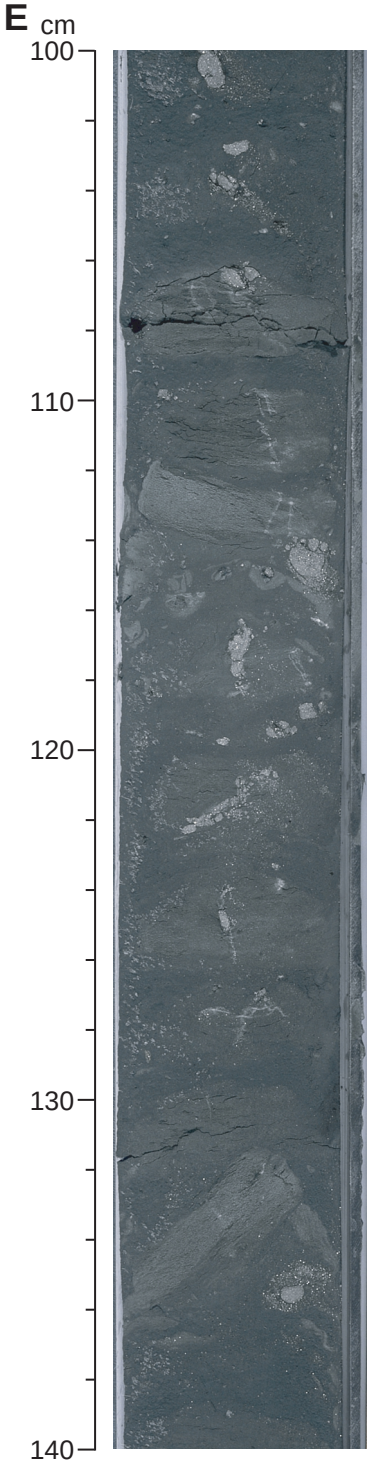

Figure F7. Planktonic foraminifer, calcareous nannofossil, and radiolarian biozonation at Site 1257. TD = total depth.

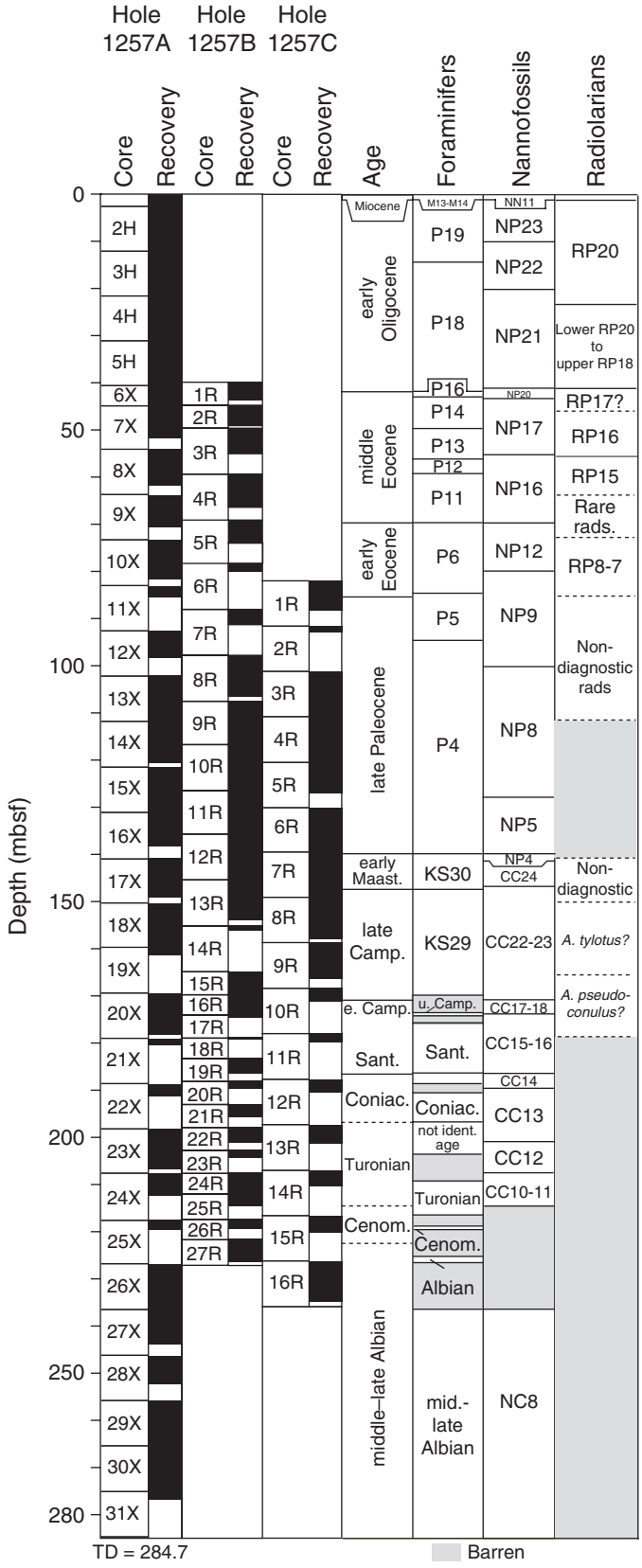

Figure F8. Shipboard paleomagnetic data and initial interpretations of inclination clusters of the Oligocene–Cretaceous from Holes 1257A, 1257B, and 1257C. Magnetic inclinations from long-core measurements from Hole 1257A are a 21-point moving average after AF demagnetization at 15 or 20 mT. Magnetic inclinations from Holes 1257B and 1257C are from intact blocks (excluding measurements in 5 cm of the end of each blocks) after 15-mT demagnetization. The inclination data exclude measurements near the background noise limit of the cryogenic magnetometer ($<3 \times 10^{-5}$ A/m); therefore, measurements with intensities $<5 \times 10^{-5}$ A/m are not considered reliable. In addition, the upper 20 cm of each core that commonly displays spurious high-intensity magnetization or downhole contamination and the upper 5 cm of each section that is influenced by magnetization carried by the blue-colored end cap are excluded. The displayed inclinations are either 3-point running means (solid circles), 2-point means (open circles), or single-level data (open triangles) (from the central portion of blocks between 10 and 15 cm long or from isolated levels in a larger block in which the adjacent measurements were $<5 \times 10^{-5}$ A/m). The magnetic intensity column is from Hole 1257A and includes NRM (small orange circles = 21-point running mean) and after 15-mT demagnetization (small black circles; large blue circles = 101-point log-mean average). Magnetic susceptibility in Hole 1257A, obtained using a magnetic susceptibility core logger (MSCL), is shown by green circles in the rightmost column. Shipboard assignment of polarity zones was based on clusters of magnetic inclinations from intact blocks (right of the polarity zone column), as delimited by the thin lines. Black/dark gray (if less certain) = positive inclinations (originally considered to be normal polarity zones); white/light gray (if less certain) = negative or mixed inclinations (originally considered to be reversed polarity zones). Cross-hatched = uncertain inclination characteristics or gaps in data coverage. The shipboard interpretations of polarity zones were not always supported by analyses of magnetic characteristics during progressive thermal demagnetization of minicores (Fig. **F9,** p. 50). F = foraminifers, N = nannofossils, R = radiolarians. (This figure is available in an **oversized format.**)

Figure F9. Magnetostratigraphy of the Eocene at Site 1257. Inclinations for Holes 1257B and 1257C are 3-point means from central portions of intact intervals as visually identified in each section. Magnetic inclinations for Hole 1257A are a 21-point moving average of the long-core measurements after AF demagnetization at 15 or 20 mT and after filtering data, as explained in Figure F8, p. 49. Yellow dots = Hole 1257A, Red dots = Hole 1257B, Green dots = Hole 1257C. Black/dark gray (if less certain) = positive inclinations (originally considered to be normal polarity zones); white/light gray (if less certain) = negative or mixed inclinations (originally considered to be reversed polarity zones). Cross-hatched = uncertain inclination characteristics or gaps in data coverage. Polarity chron assignments are based on the polarity zone pattern and microfossil biostratigraphy. F = foraminifers, N = nannofossils, R = radiolarians, TD = total depth.

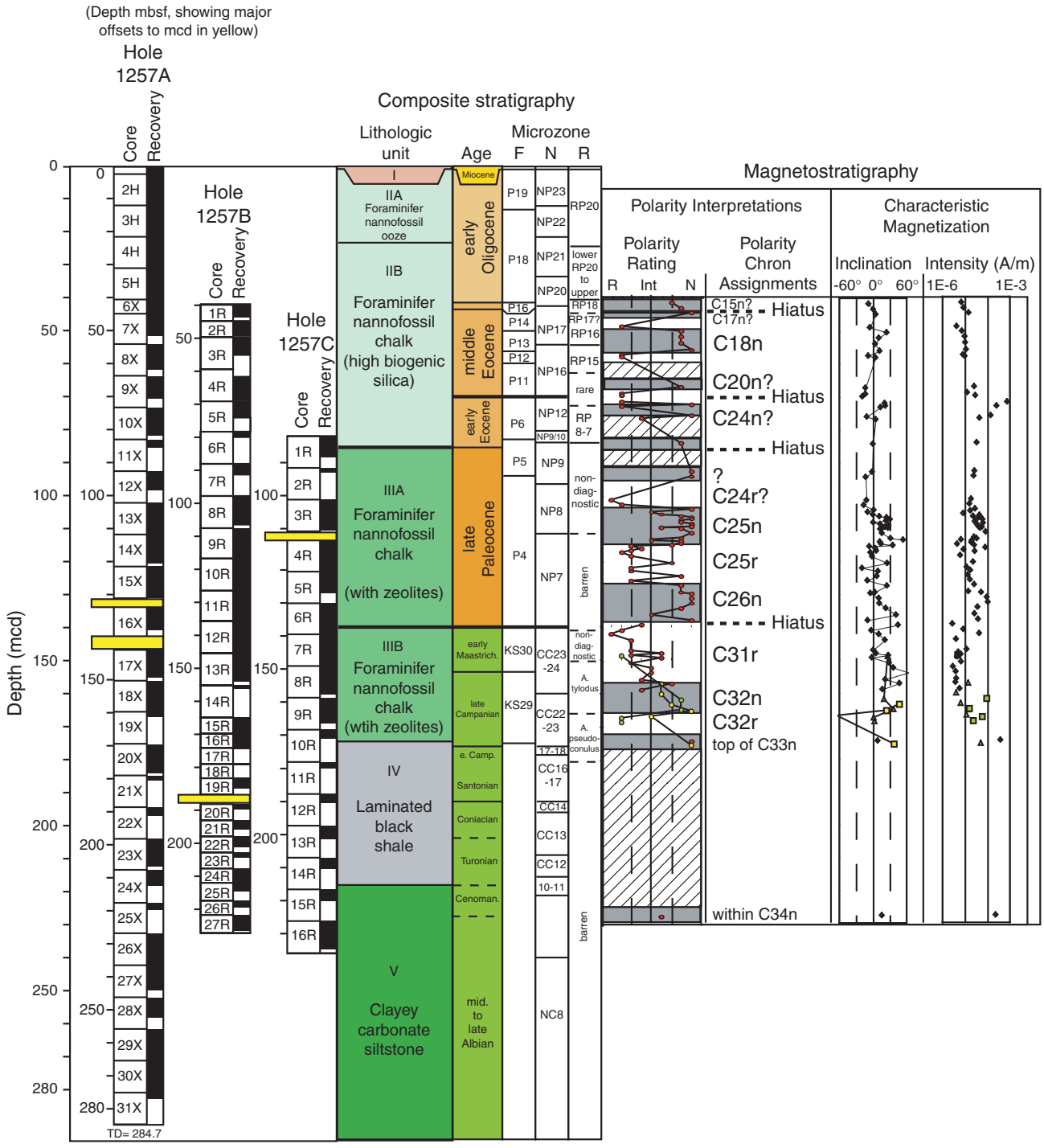

Figure F10. Magnetic susceptibility data plotted with a qualitative estimate of the confidence of the core-to-core correlations among holes at Site 1257. **A.** The composite data from Holes 1257A and 1257B are offset by a constant (5 and 10 units, respectively) for illustration purposes. All data sets are smoothed with a 9-point Gaussian filter. **B.** Green = interval with definitive hole-to-hole correlations and a high-quality splice (i.e., most core gaps spanned), yellow = intervals where core-to-core correlations could be made (i.e., a one-to-one match of signals between holes) but definitive depth positions could not be established because core gaps could not be spanned. In many cases, the poor core quality resulted in only short intervals in a single core having a high-quality signal for correlation (e.g., 180–240 mcd). Thus, correlated cores in the yellow intervals may only have a 1–2 m that have similar MST signals. Diagonal line pattern = intervals where hole-to-hole correlations could not be made (primarily a result of only one hole in that interval). P/E = Paleocene/Eocene boundary, K/T = Cretaceous/Tertiary boundary.

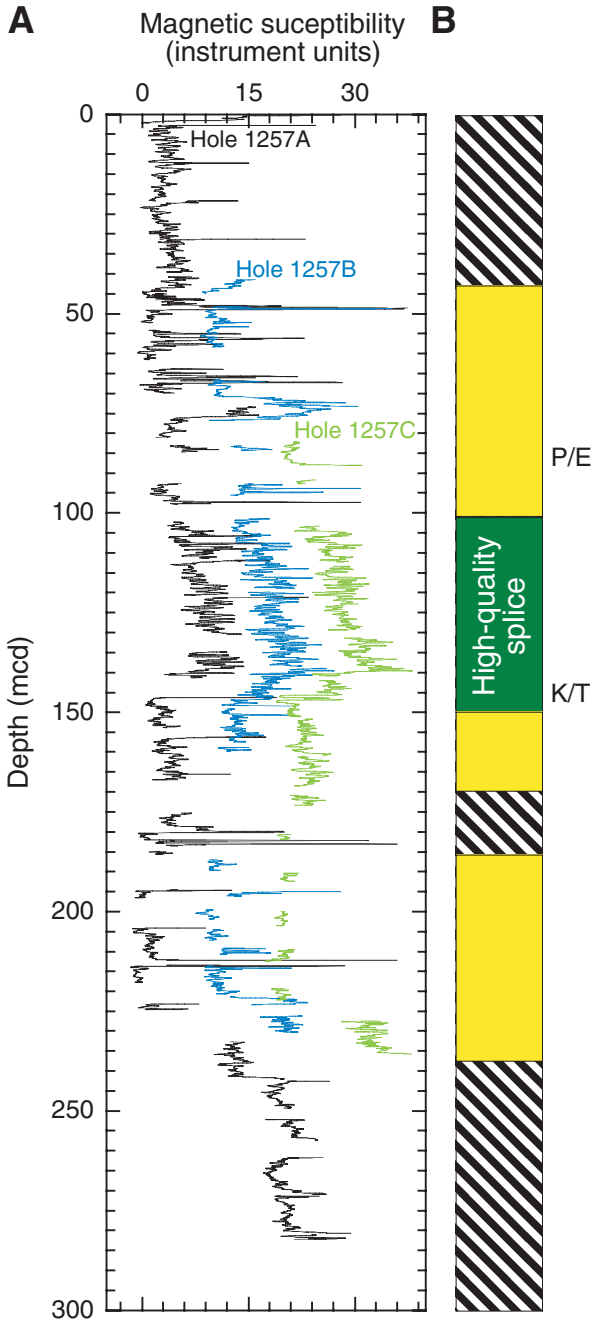

Figure F11. A. Magnetic susceptibility record for the upper Paleocene section of Holes 1257B and 1257C. The data from Hole 1257C are offset by a constant for illustration purposes. **B.** Spliced magnetic susceptibility record for the upper Paleocene section at Site 1257. Black = cores from Hole 1257B used in the splice; blue = cores from Hole 1257C used in the splice. All data sets are smoothed with a 9-point Gaussian filter.

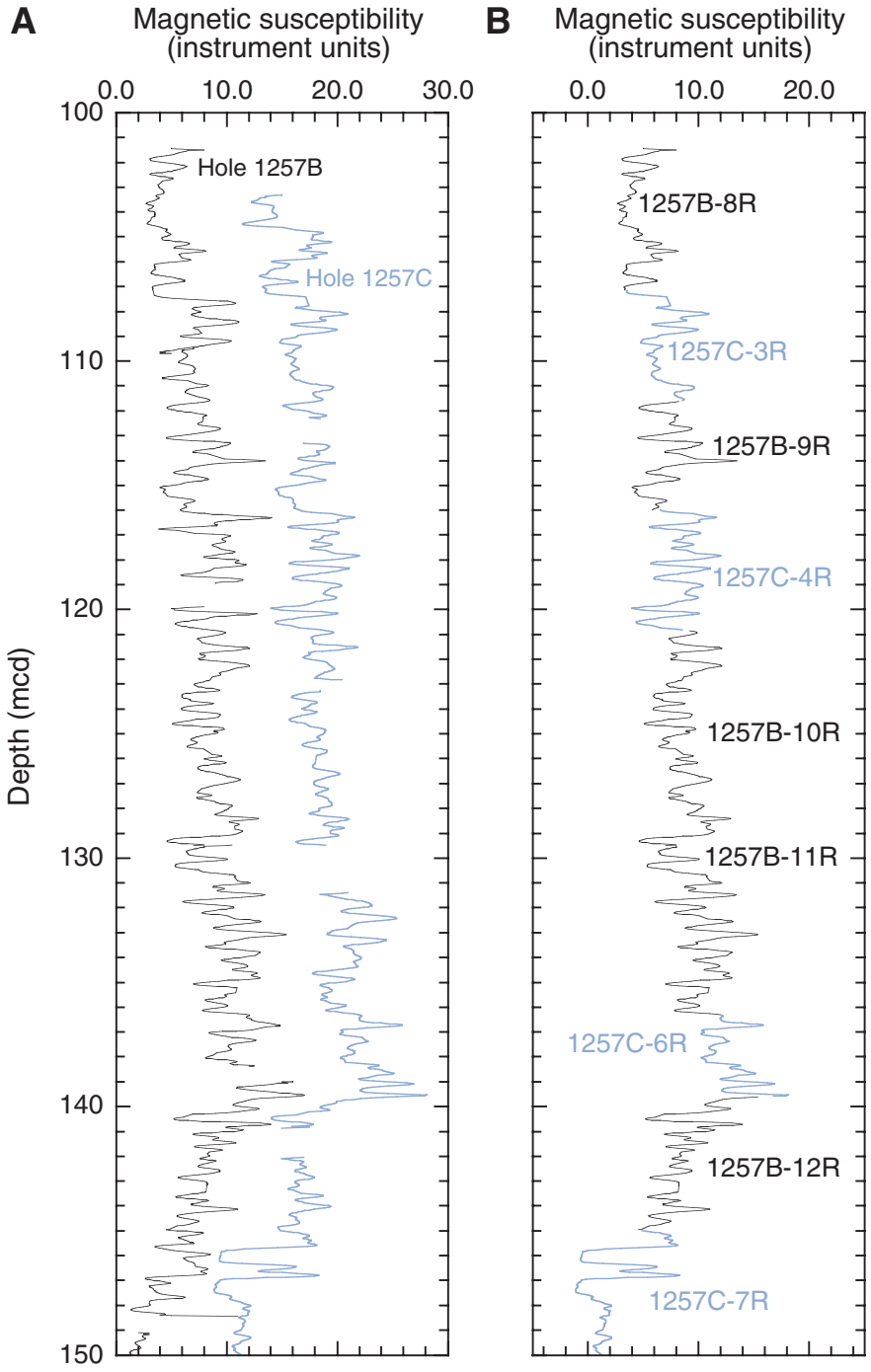

Figure F12. A. NGR record for the upper Paleocene section from Holes 1257B, and 1257C. The data from Hole 1257C are offset by a constant for illustration purposes. **B.** Spliced NGR record for the upper Paleocene section at Site 1257. Black = cores from Hole 1257B used in the splice; blue = cores from Hole 1257C used in the splice. All data sets are smoothed with a 9-point Gaussian filter.

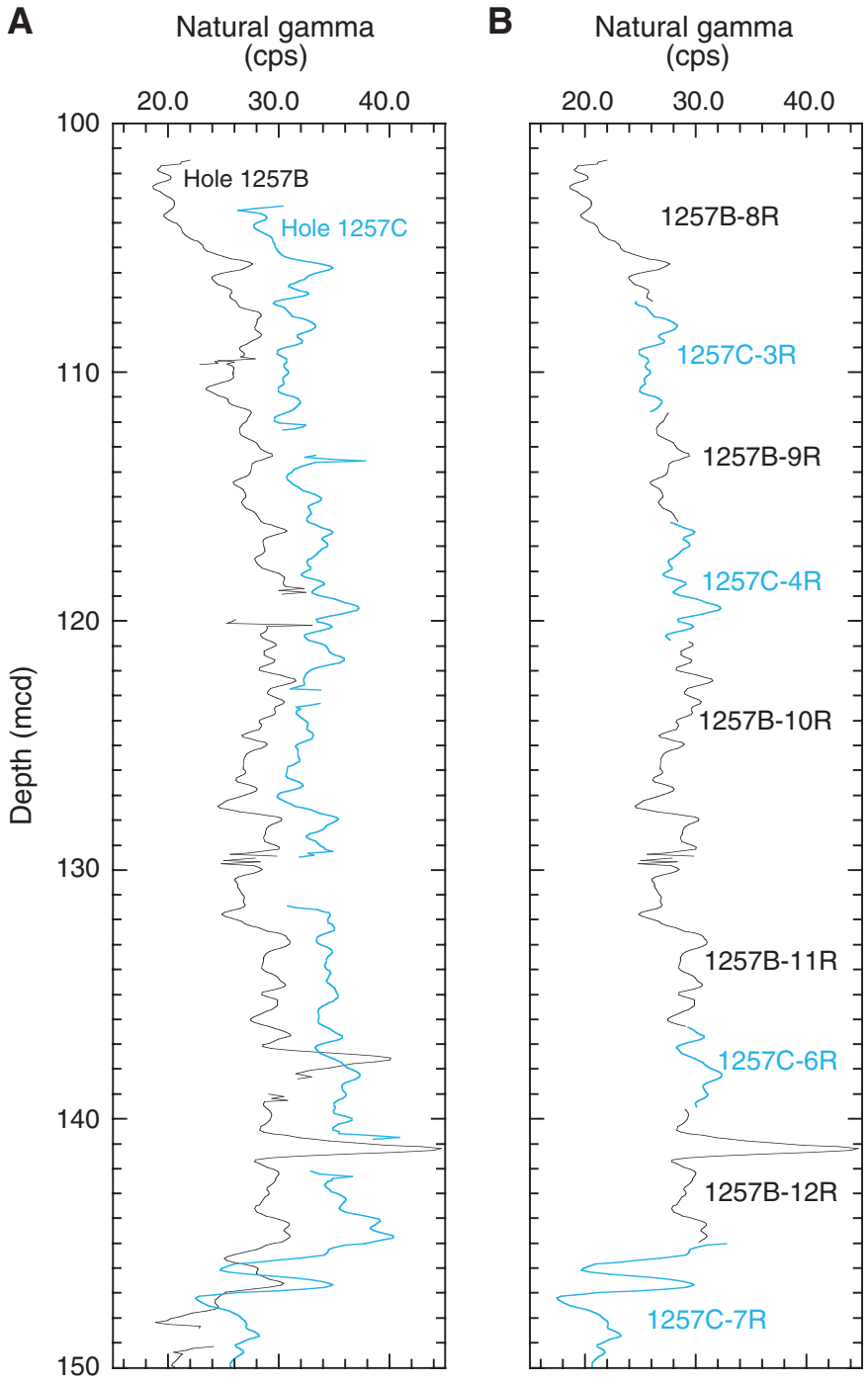

Figure F13. Age-depth plot combining all available biostratigraphic and magnetostratigraphic datums from Hole 1257A, suggesting five intervals (A–E) with apparently constant LSRs. Apparent hiatuses are also present at five levels. E/O = Eocene/Oligocene boundary, K/T = Cretaceous/Tertiary boundary.

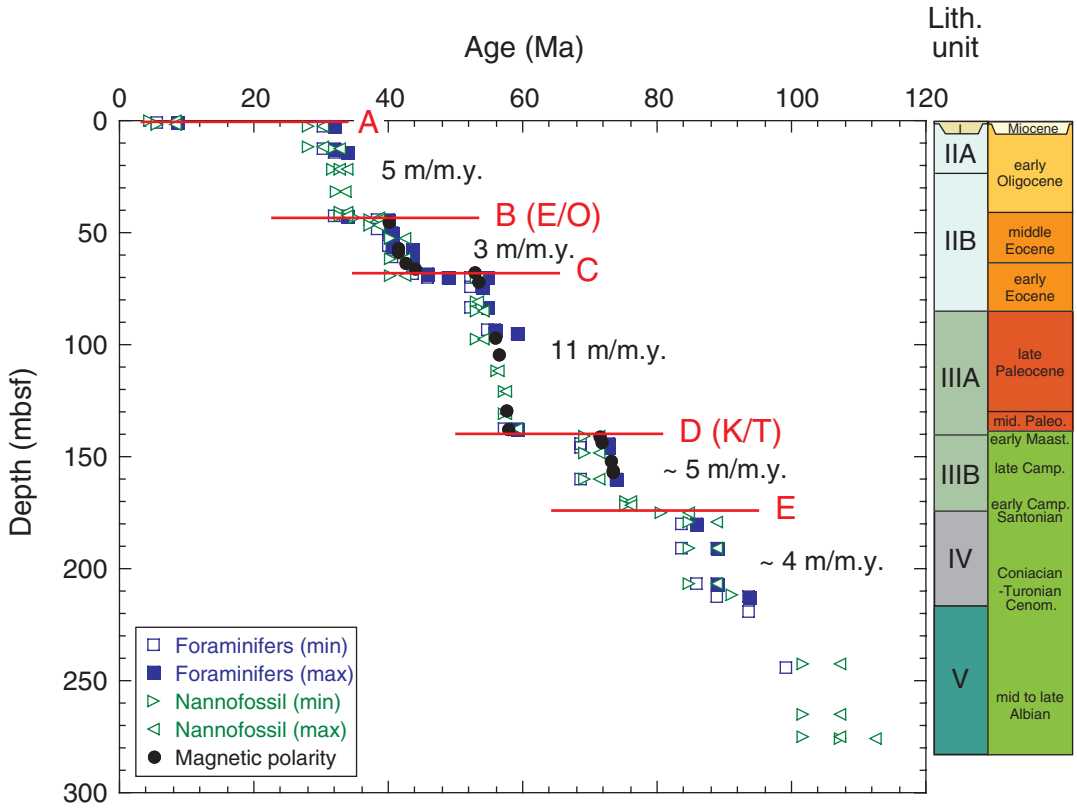

Figure F14. Rock-Eval pyrolysis van Krevelen–type diagram of sediment samples from Holes 1257A, 1257B, and 1257C. Organic matter appears to be predominantly Type II algal material that has been variably oxidized.

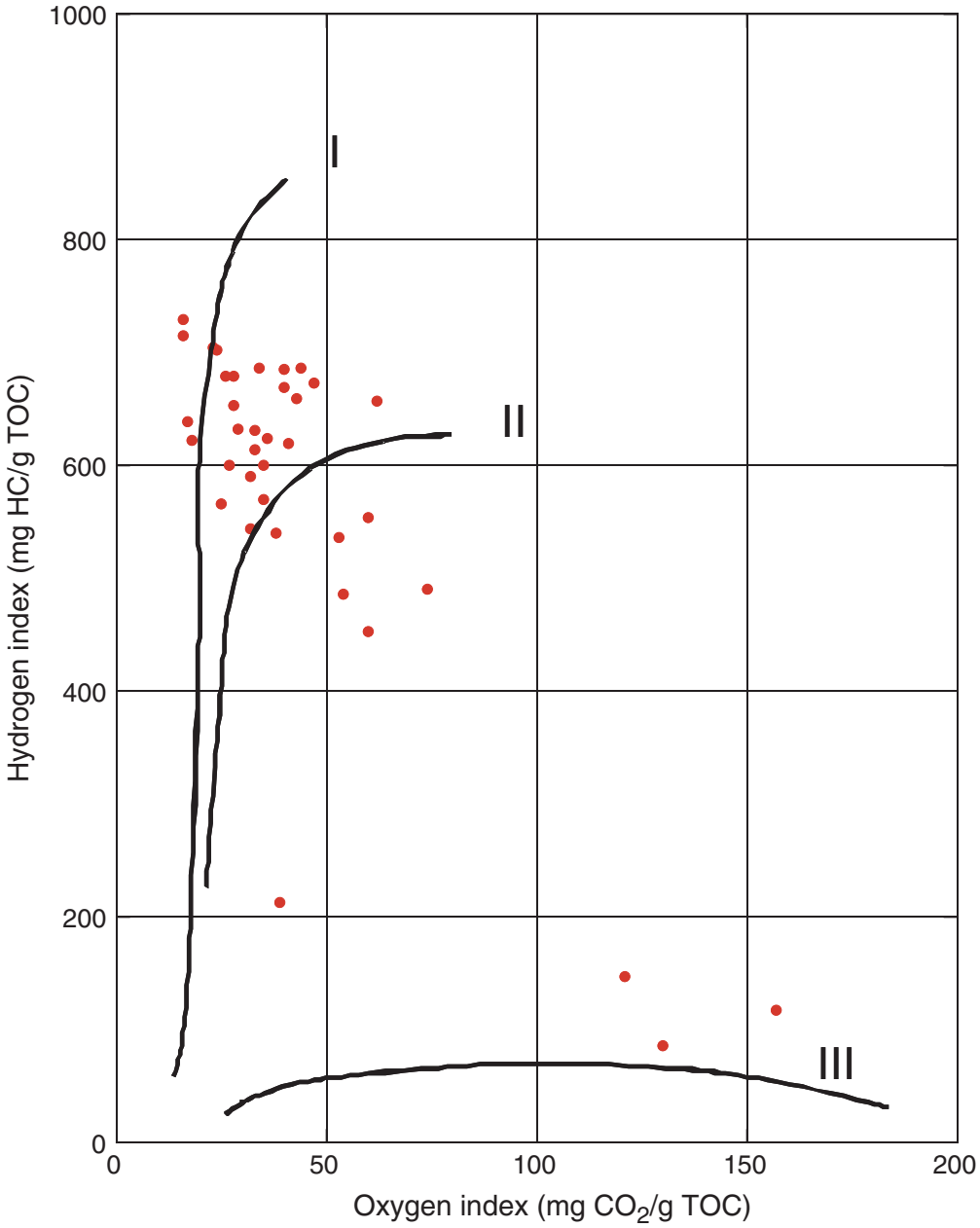

Figure F15. Comparison of concentrations of routine headspace gas (HS) analyses and microbial methane in sediments from Hole 1257A.

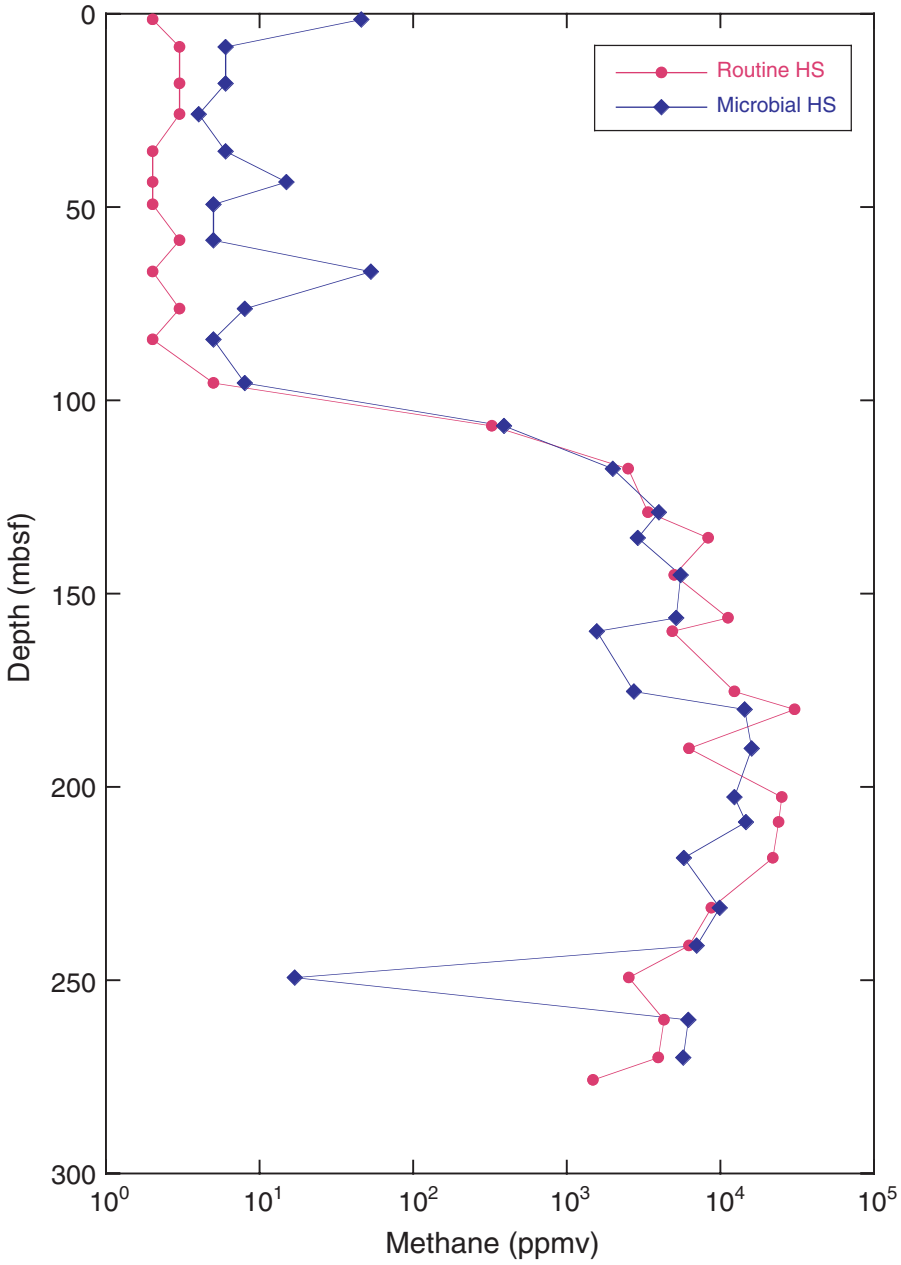

Figure F16. Profiles of chemical constituents in interstitial waters from Site 1257. Data from DSDP Site 144 are given for comparison (Waterman et al., 1972; Presley et al., 1973). Shaded intervals = approximate depth interval of Unit IV, the black shale sequence. ICP-AES = inductively coupled plasma–atomic emission spectroscopy. **A.** Salinity. **B.** Chloride. **C.** Sodium. **D.** Potassium. **E.** Alkalinity. **F.** Sulfate. **G.** Ammonium. **H.** Barium. (Continued on next page.)

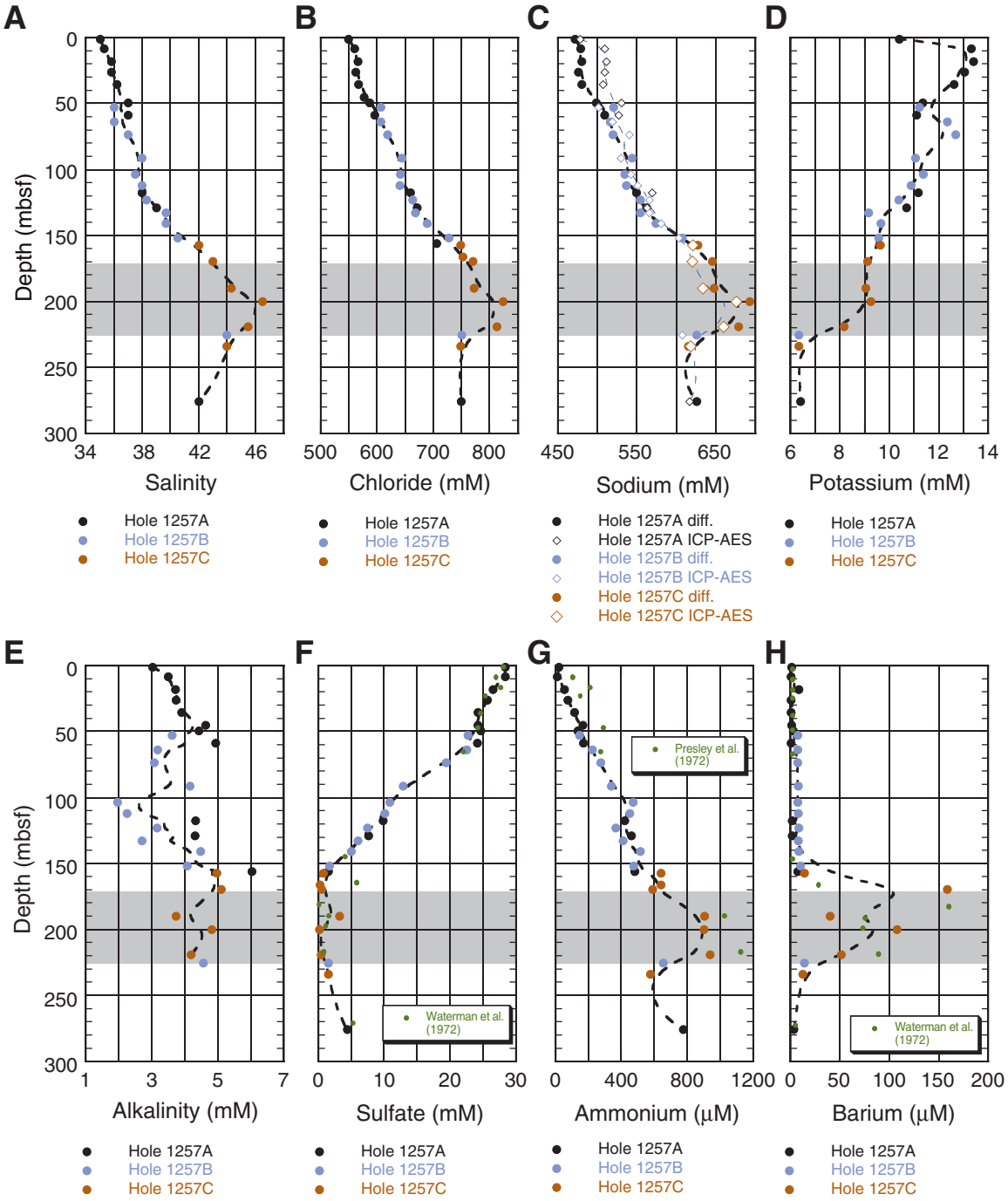

Figure F16 (continued). **I.** Calcium. **J.** Strontium. **K.** Magnesium. **L.** Lithium. **M.** Boron. **N.** Silica. **O.** Iron. **P.** Manganese.

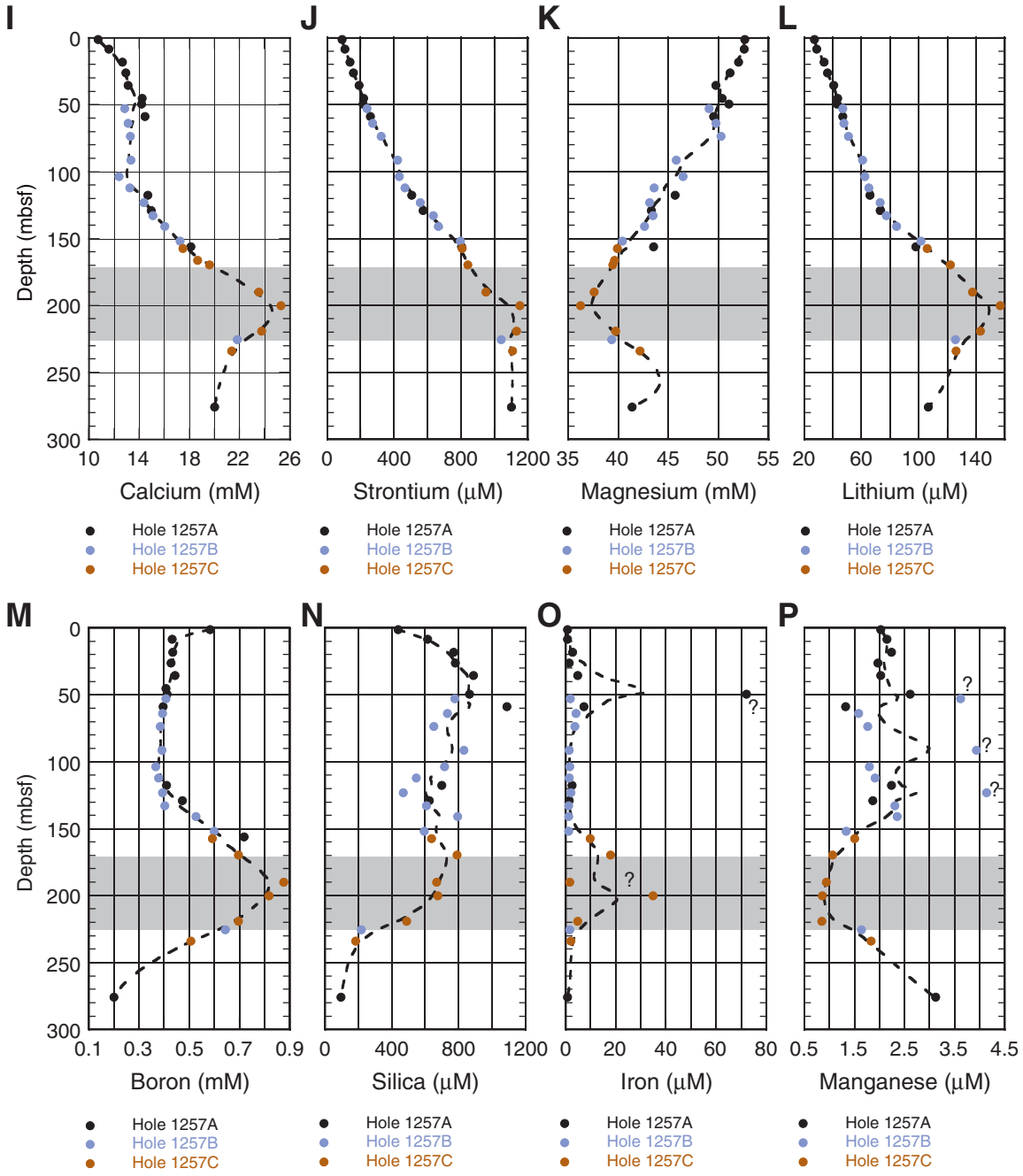

Figure F17. Correlation of (A) strontium vs. magnesium and (B) chloride vs. lithium in interstitial waters retrieved from Site 1257.

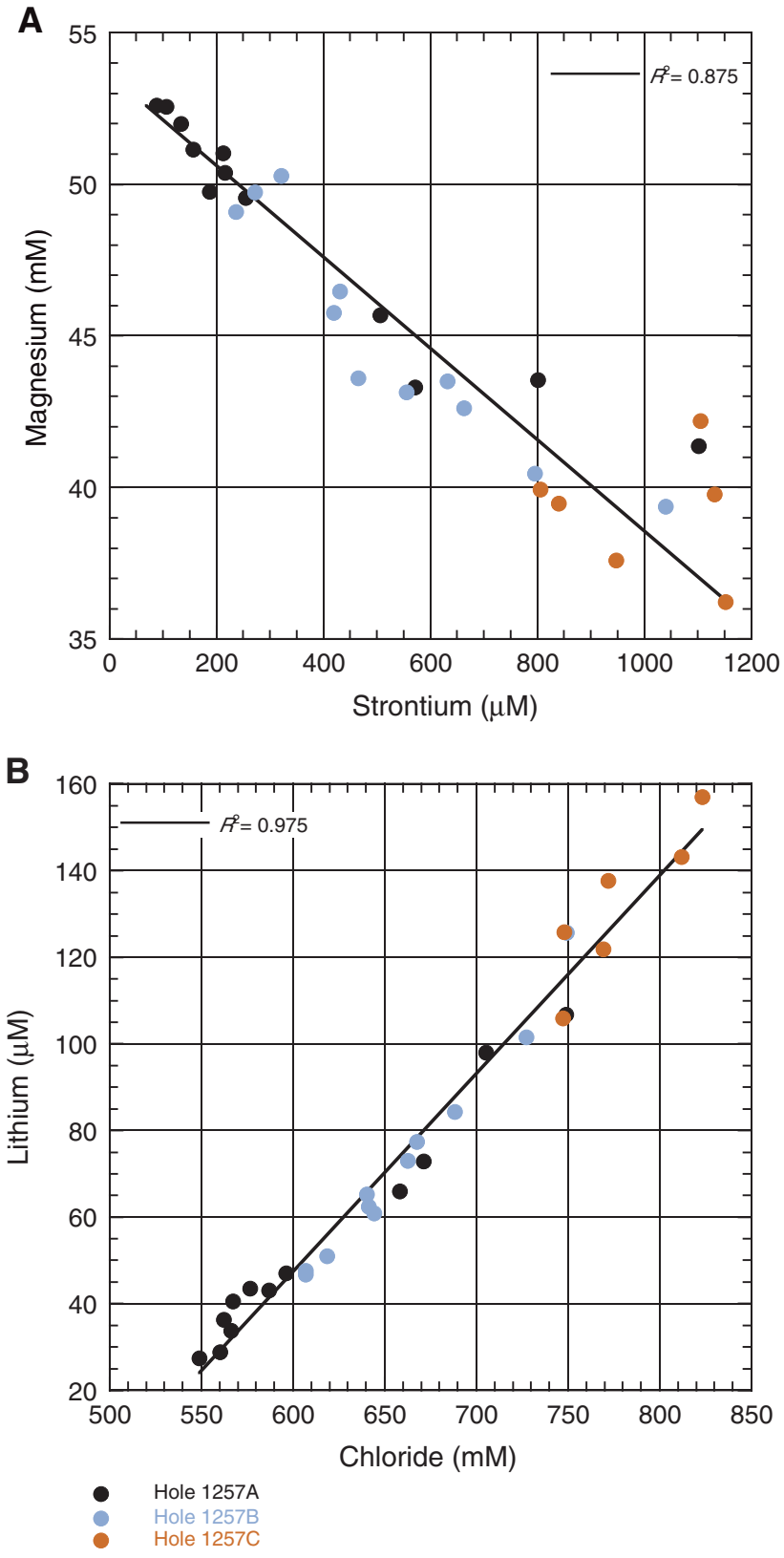

Figure F18. Bulk density, grain density, and porosity of discrete samples at Site 1257. Red = Hole 1257A, blue = Hole 1257B, green = Hole 1257C.

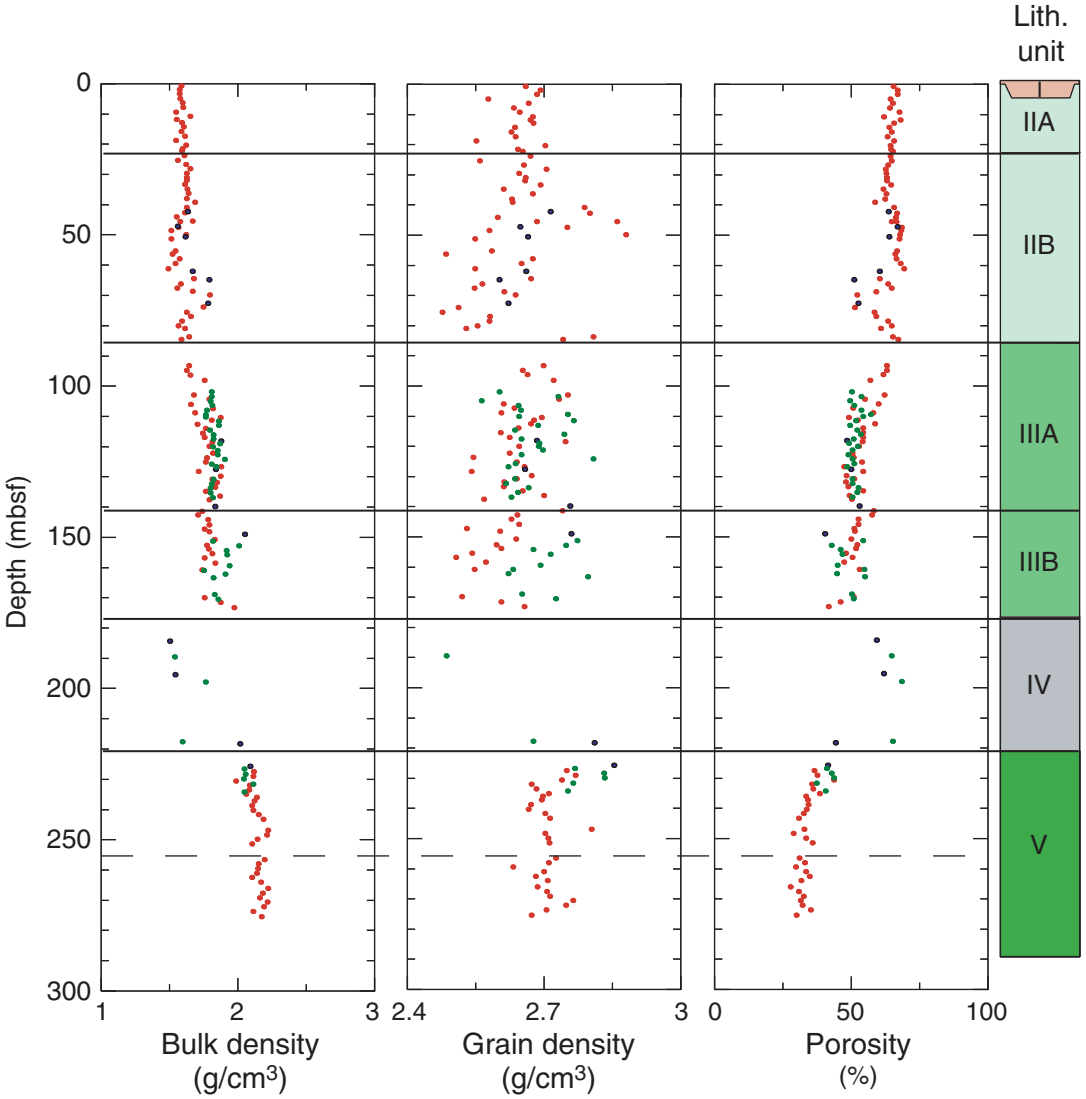

Figure F19. MAD densities (red) compared to MST GRA density (blue) in Holes 1257A, 1257B, and 1257C.

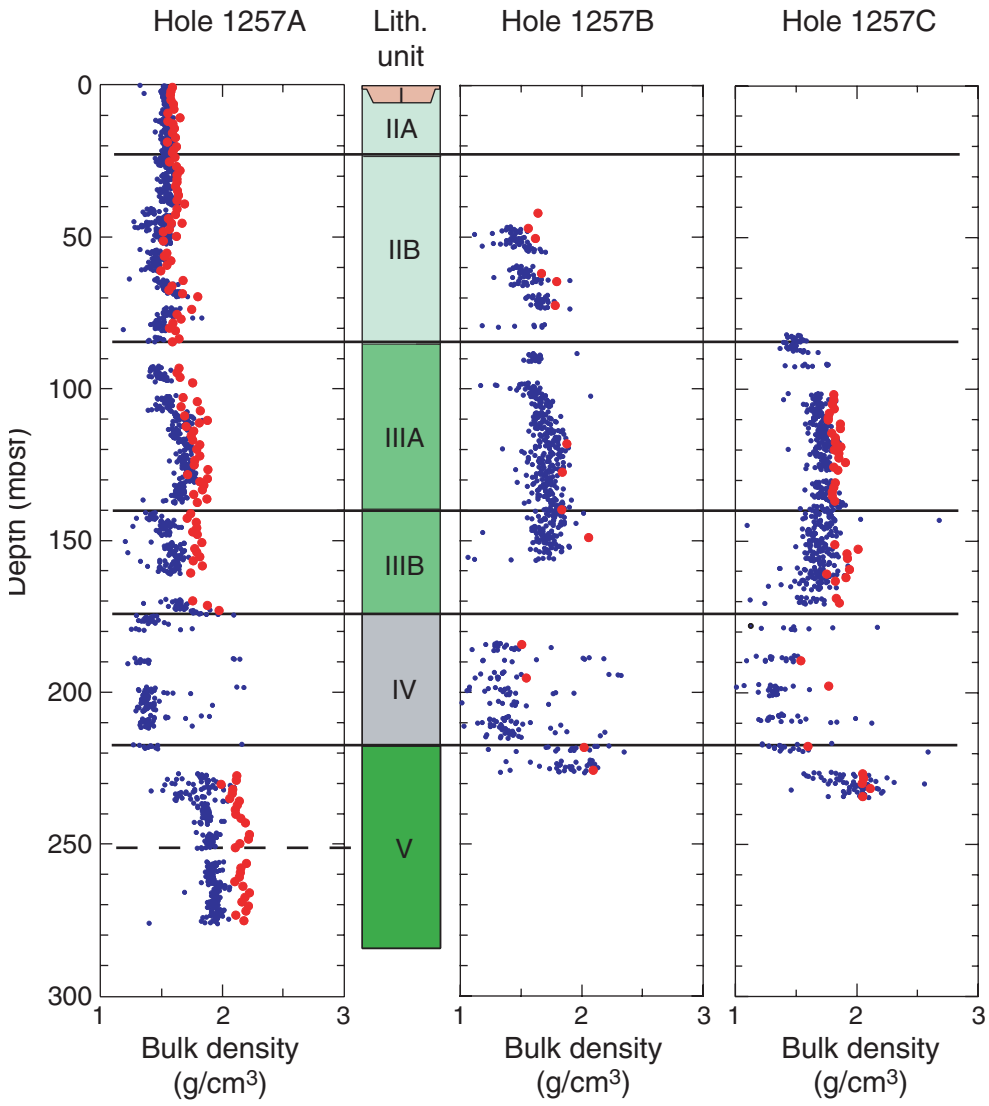

Figure F20. A. *P*-wave velocity measurements from split cores at Site 1257. Red = Hole 1257A, blue = Hole 1257B, green = Hole 1257C. **B.** Combined split-core velocity measurements (black) (corrected for in situ temperature and pressure) overlain with logging velocities (blue).

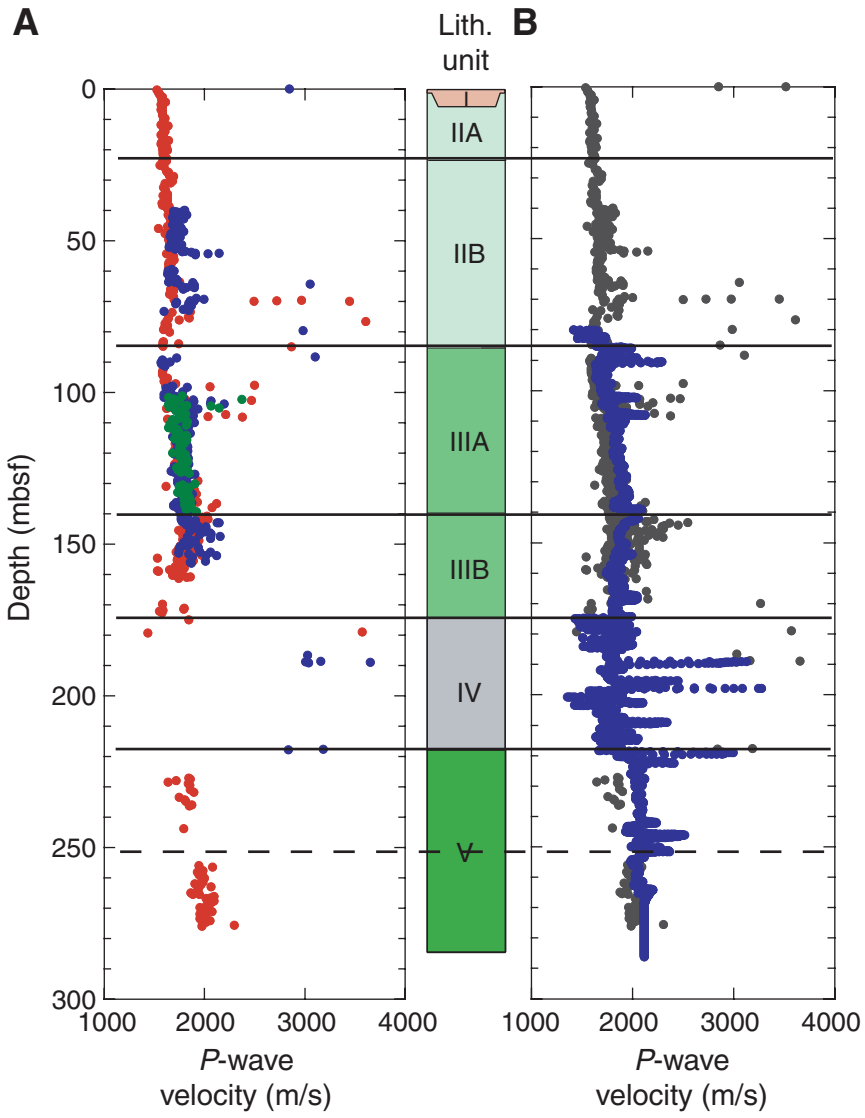

Figure F21. MST data. NGR = natural gamma radiation. **A.** Hole 1257A. (Continued on next two pages.)

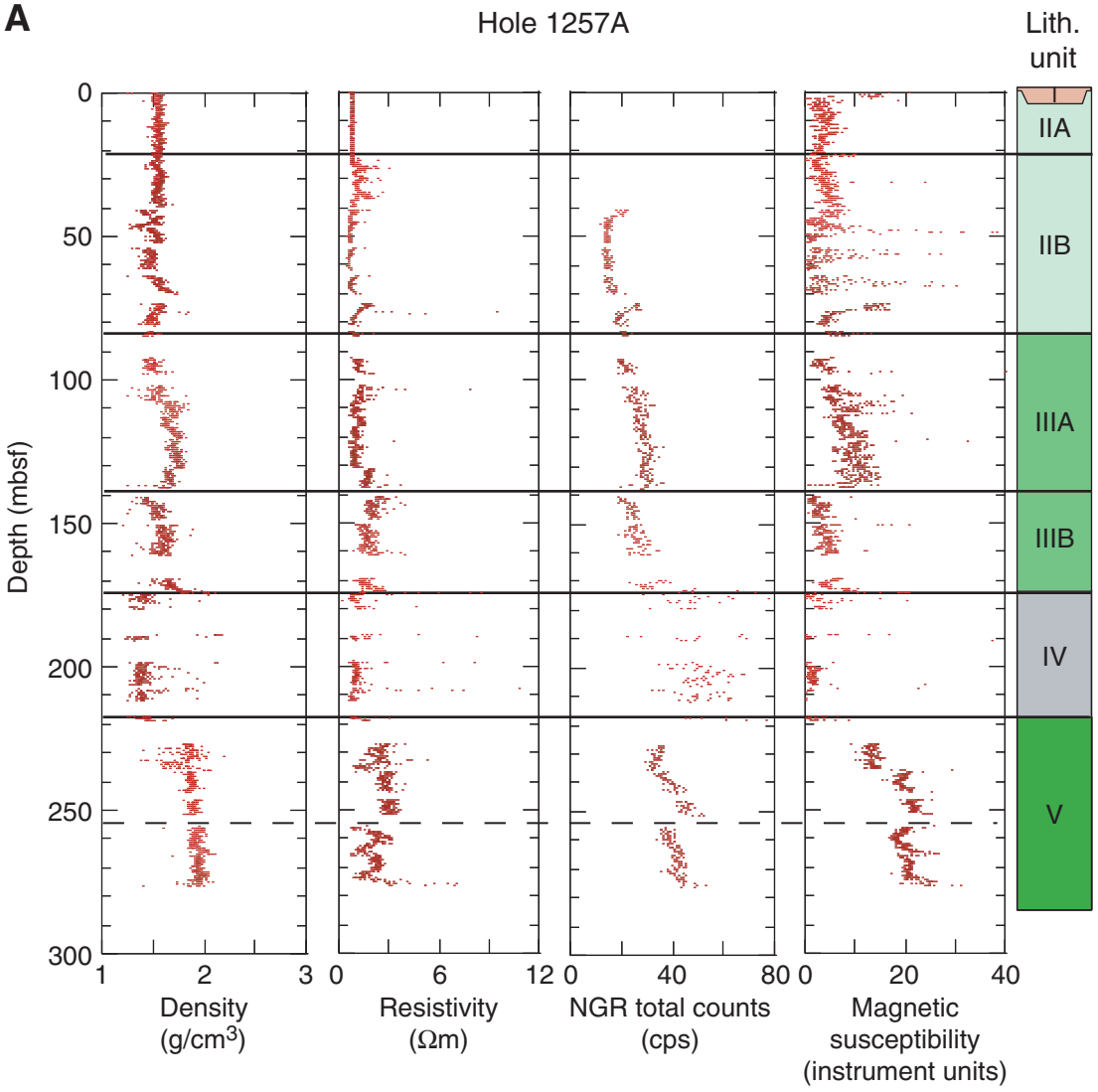

Figure F21 (continued). B. Hole 1257B.

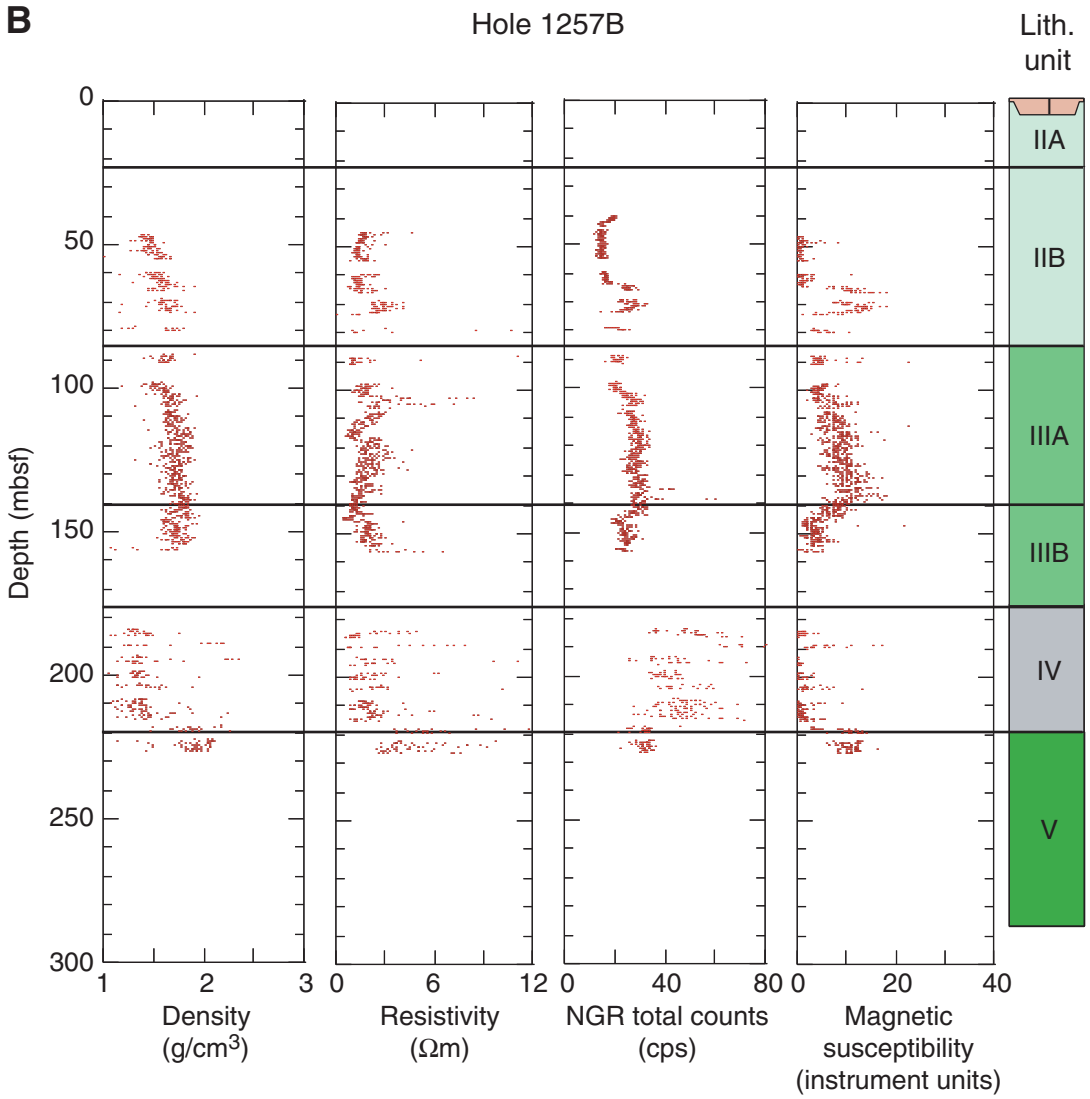

Figure F21 (continued). C. Hole 1257C.

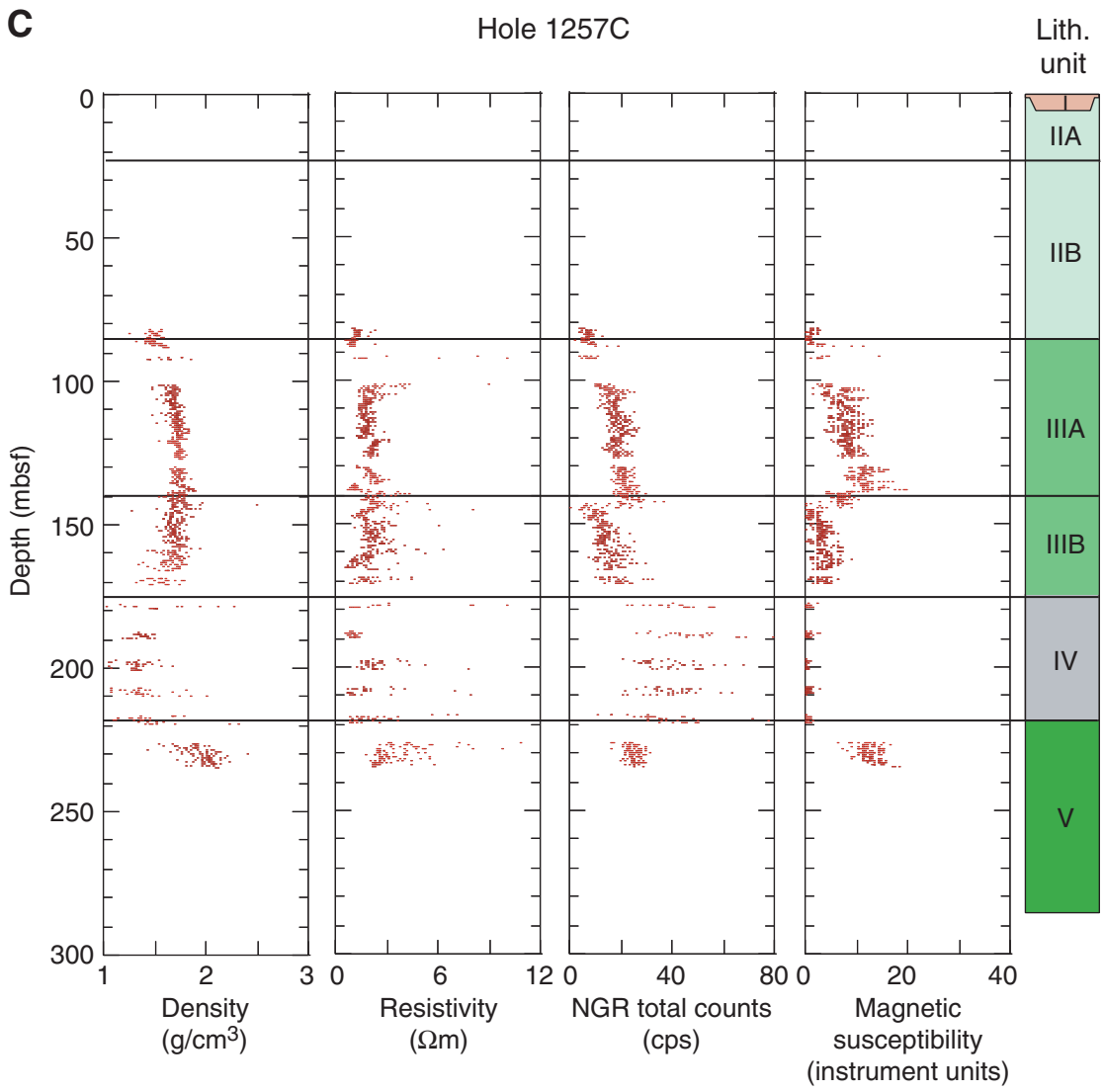

Figure F22. Summary of logging runs in Hole 1257A. MGT = Multi-Sensor Spectral Gamma Ray Tool, FMS = Formation MicroScanner, WST = Well Seismic Tool.

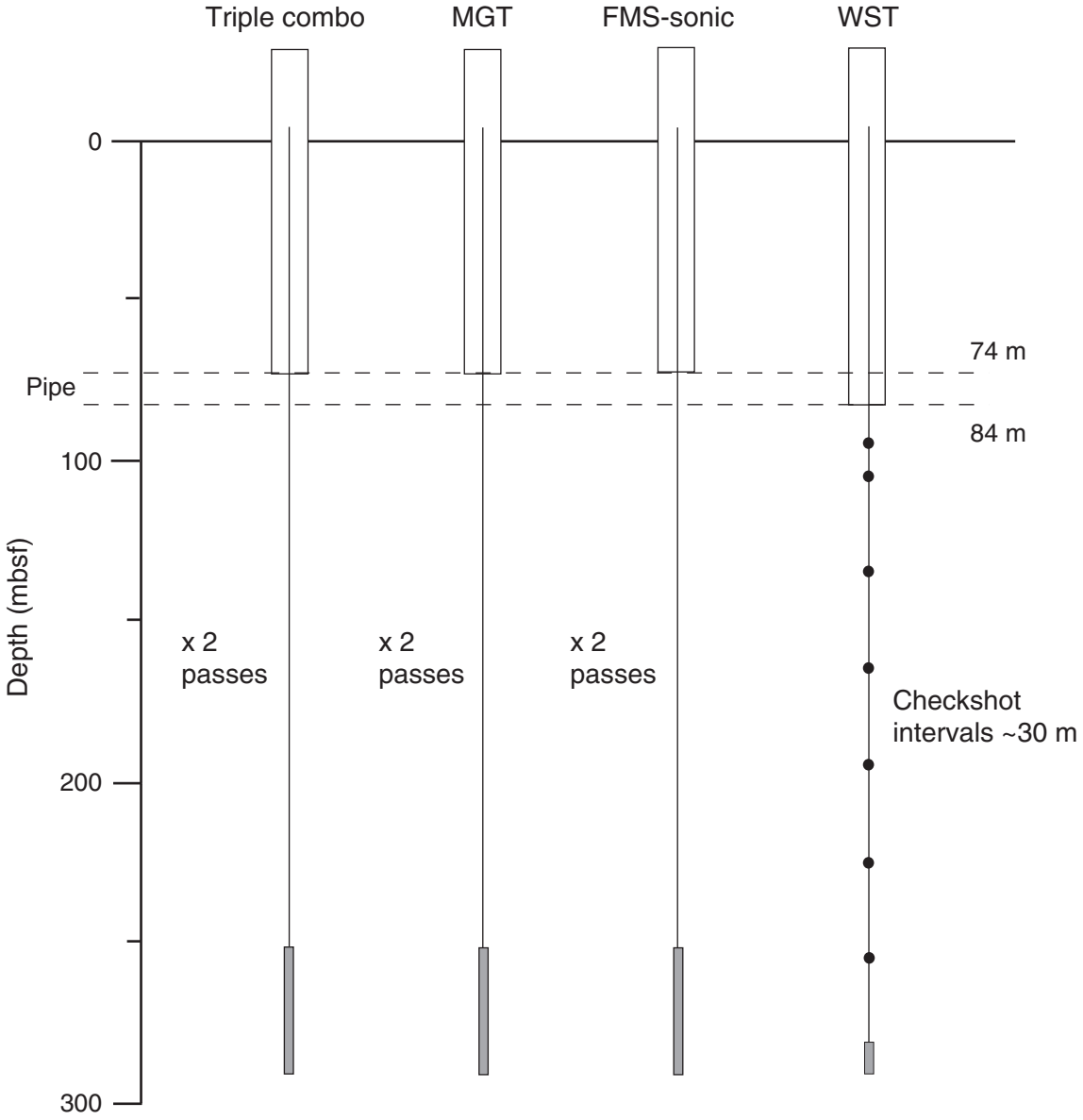

Figure F23. Borehole caliper logs from two passes of the triple combination (TC) and Formation MicroScanner (FMS)-sonic tool strings.

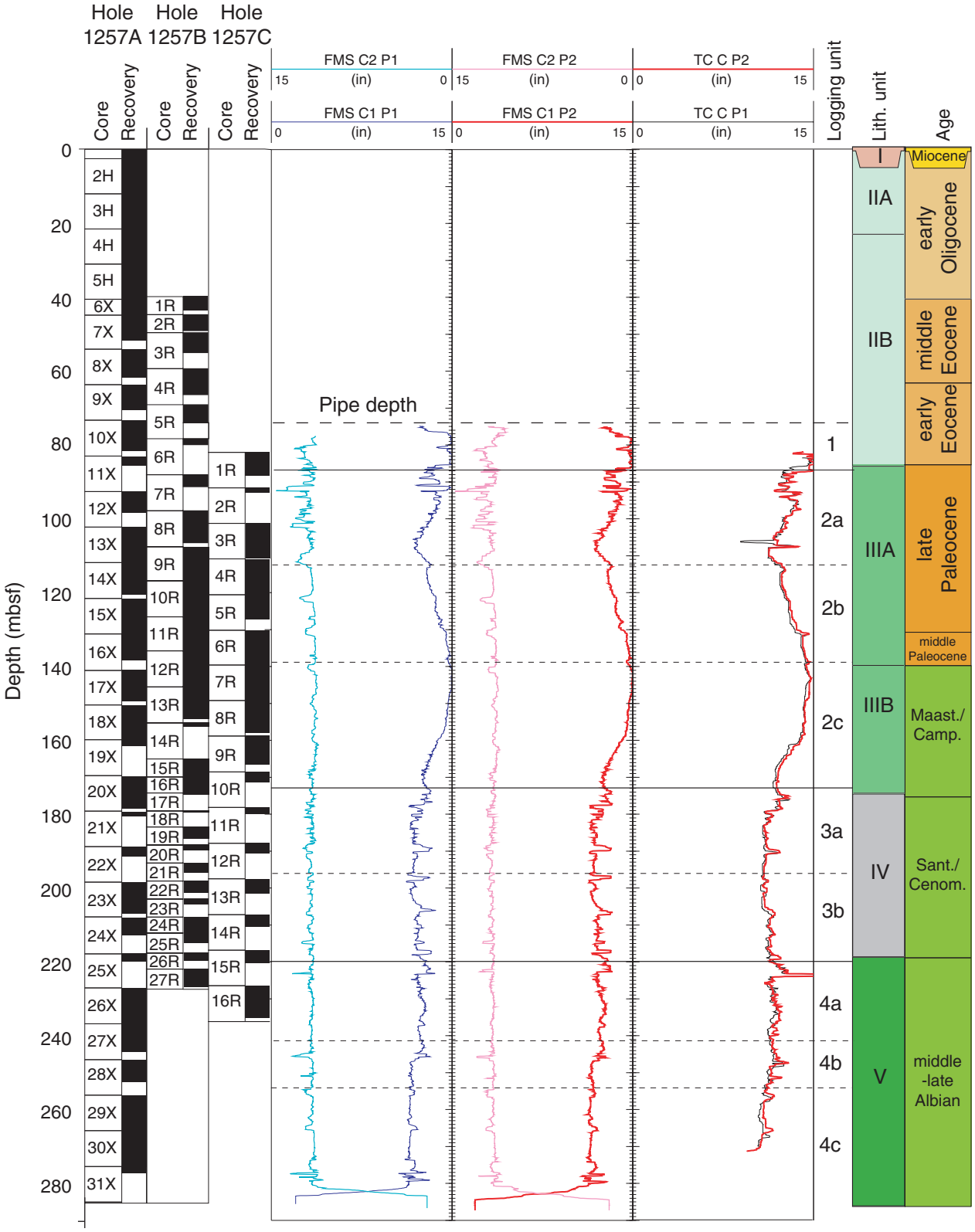

Figure F24. Geophysical logs and equivalent core physical properties from Hole 1257A. TC = triple combination.

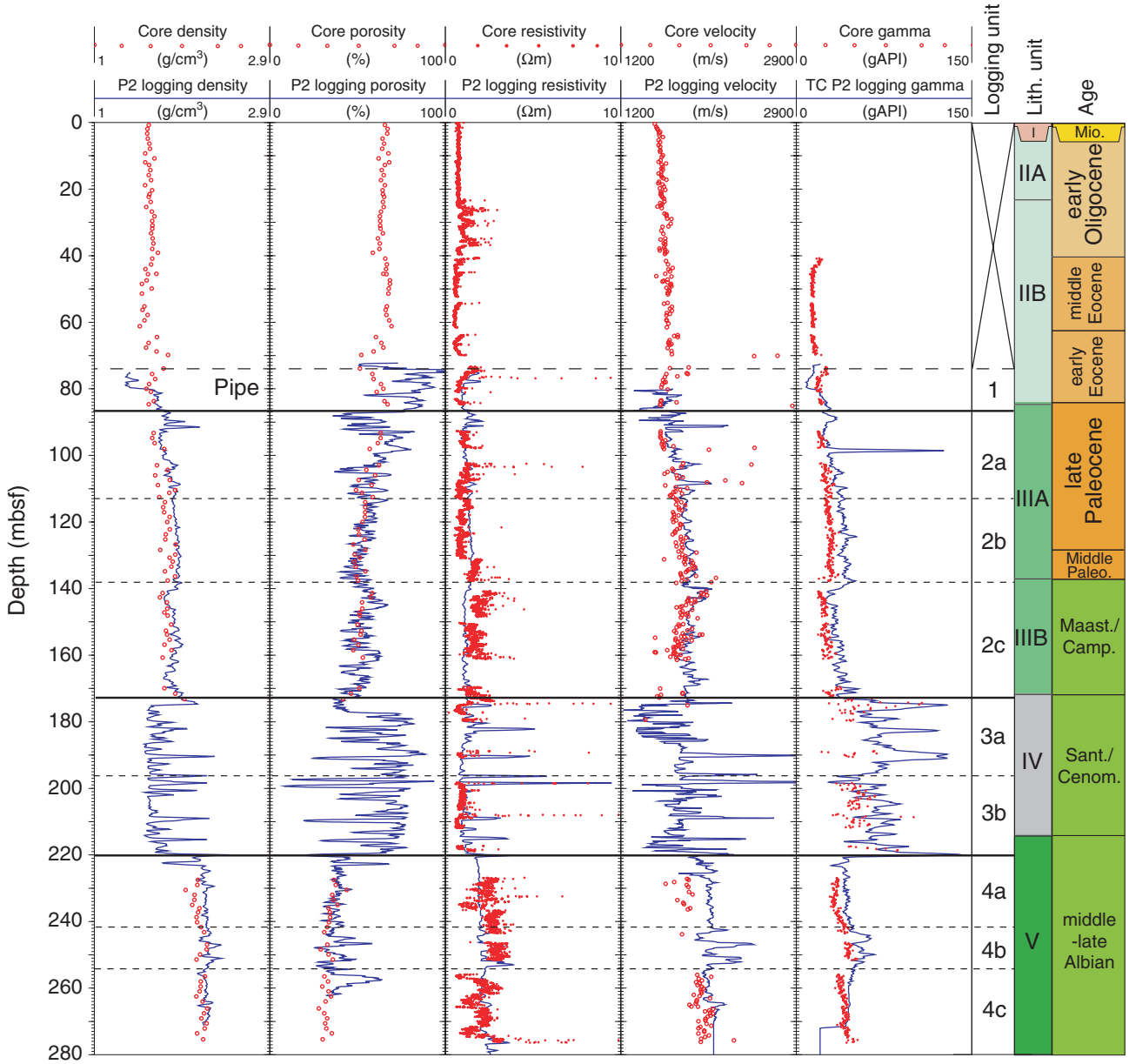

Figure F25. Geophysical logs, caliper data, and logging units from Hole 1257A. TC = triple combination, FMS = Formation MicroScanner, MGT = Multi-Sensor Spectral Gamma Ray Tool, HSGR = HNGS standard (total) gamma ray, PEF = photoelectric effect.

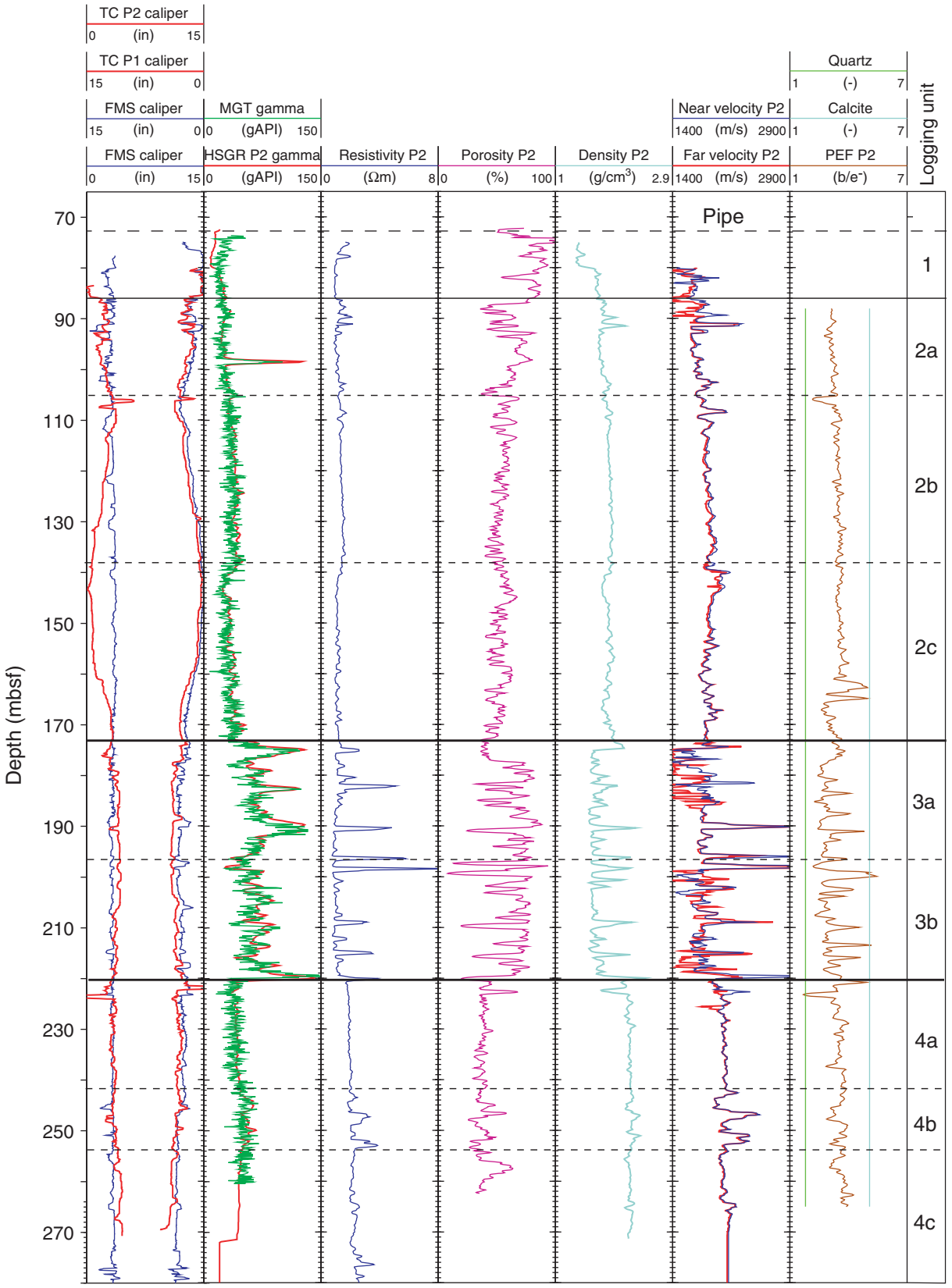

Figure F26. Logging data from logging Units 1 and 2 in Hole 1257A. TC = triple combination, FMS = Formation MicroScanner, MGT = Multi-Sensor Spectral Gamma Ray Tool, HSGR = HNGS standard (total) gamma ray.

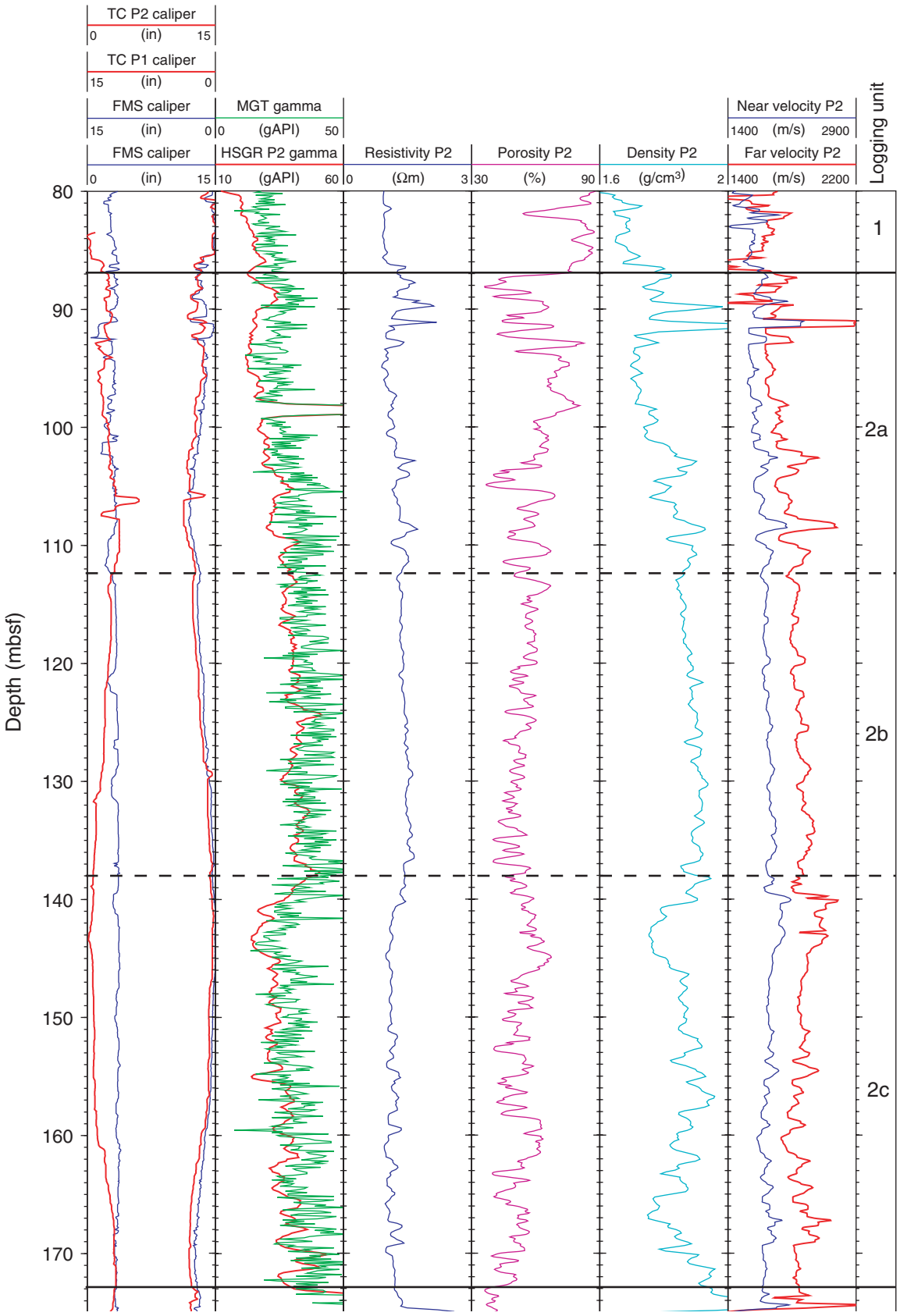

Figure F27. High-resolution MGT gamma ray logs from Hole 1257A. CGR = computed gamma ray.

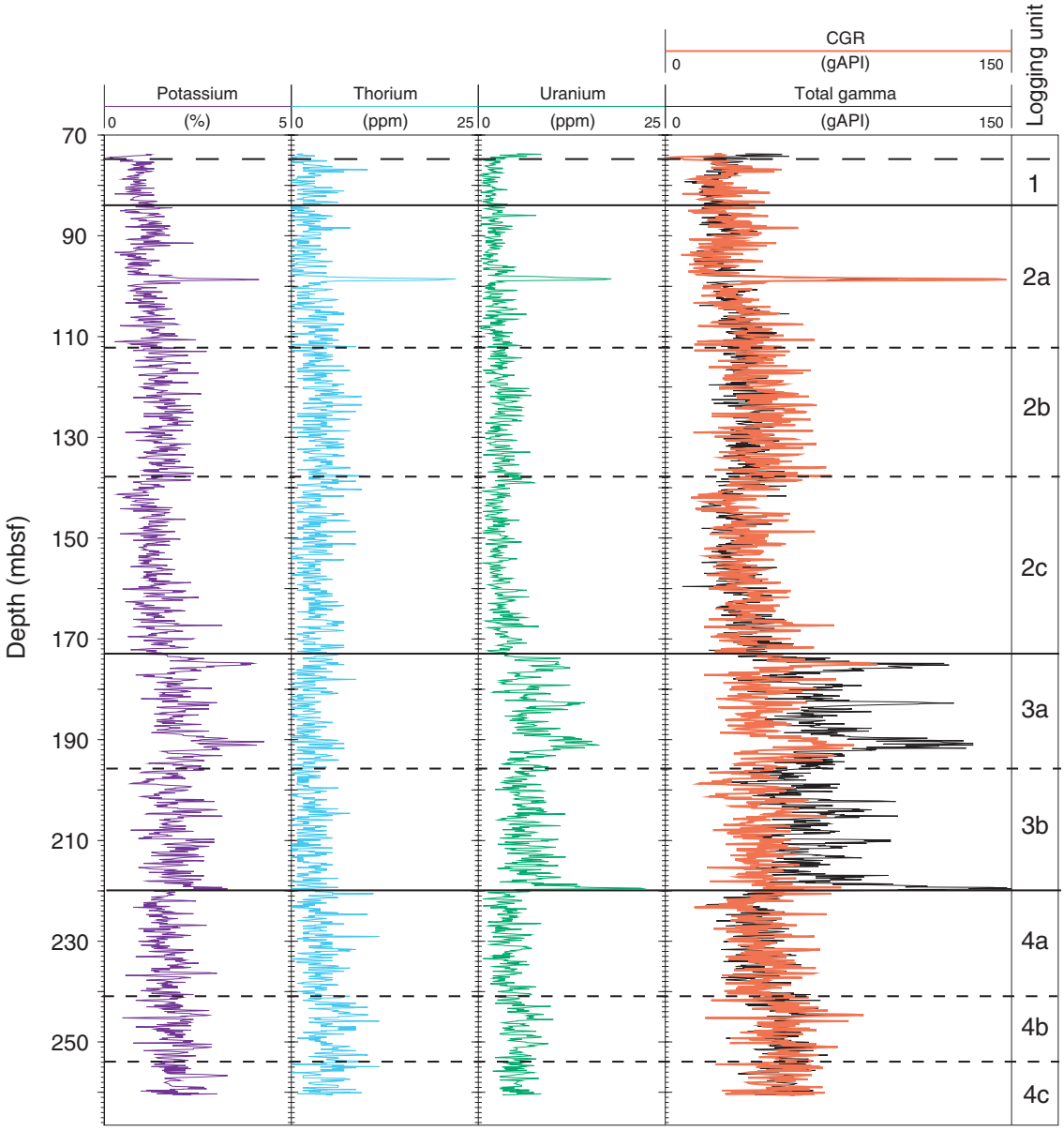

Figure F28. Geophysical logs and Formation MicroScanner (FMS) imagery through the black shale interval, logging Unit 3, in Hole 1257A. TC = triple combination, MGT = Multi-Sensor Spectral Gamma Ray Tool, HSGR = HNGS standard (total) gamma ray, PEF = photoelectric effect.

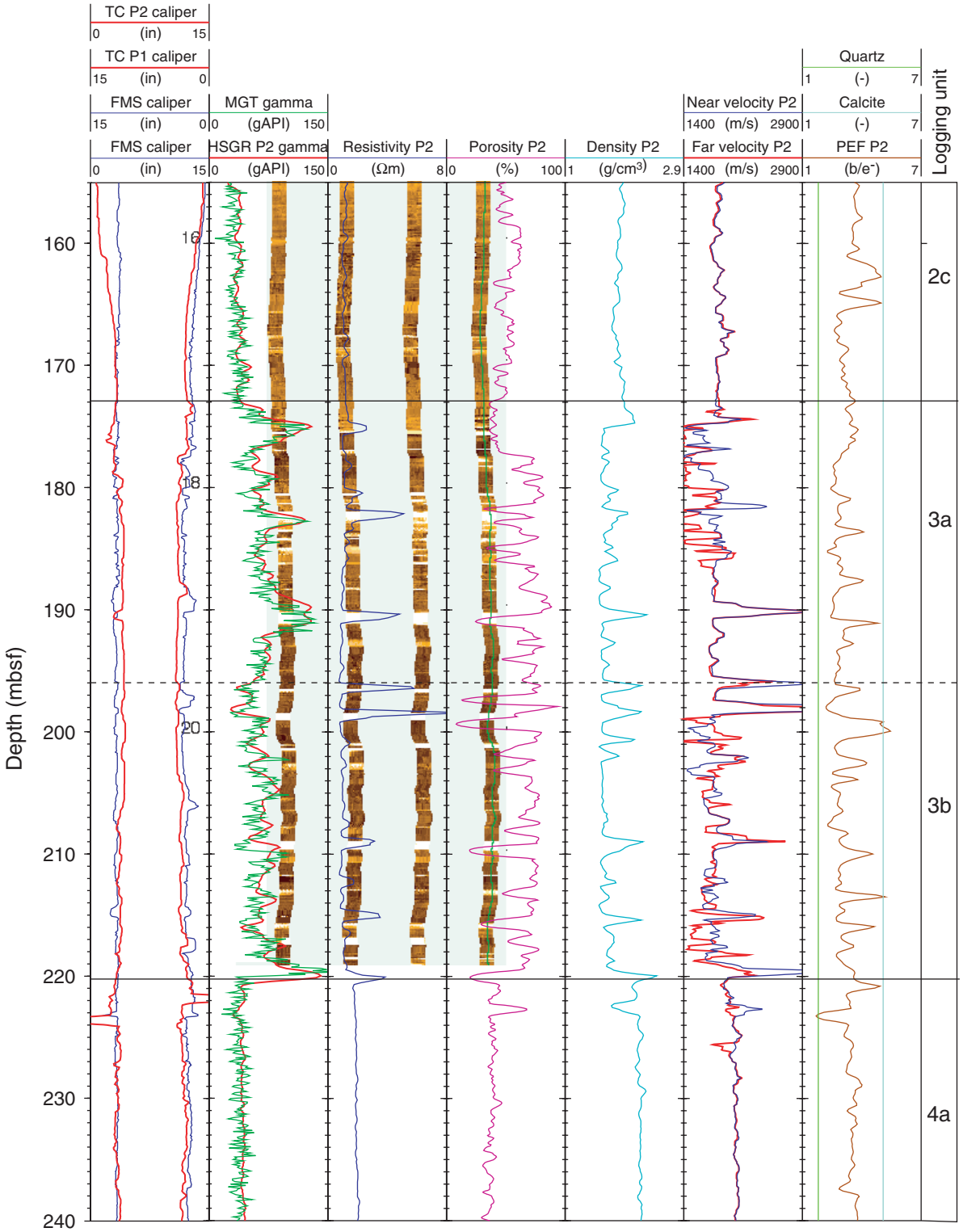

Figure F29. Comparisons of core-measured total organic carbon (TOC) and log-calculated TOC values through the black shale interval from logging Unit 3 in Hole 1257A.

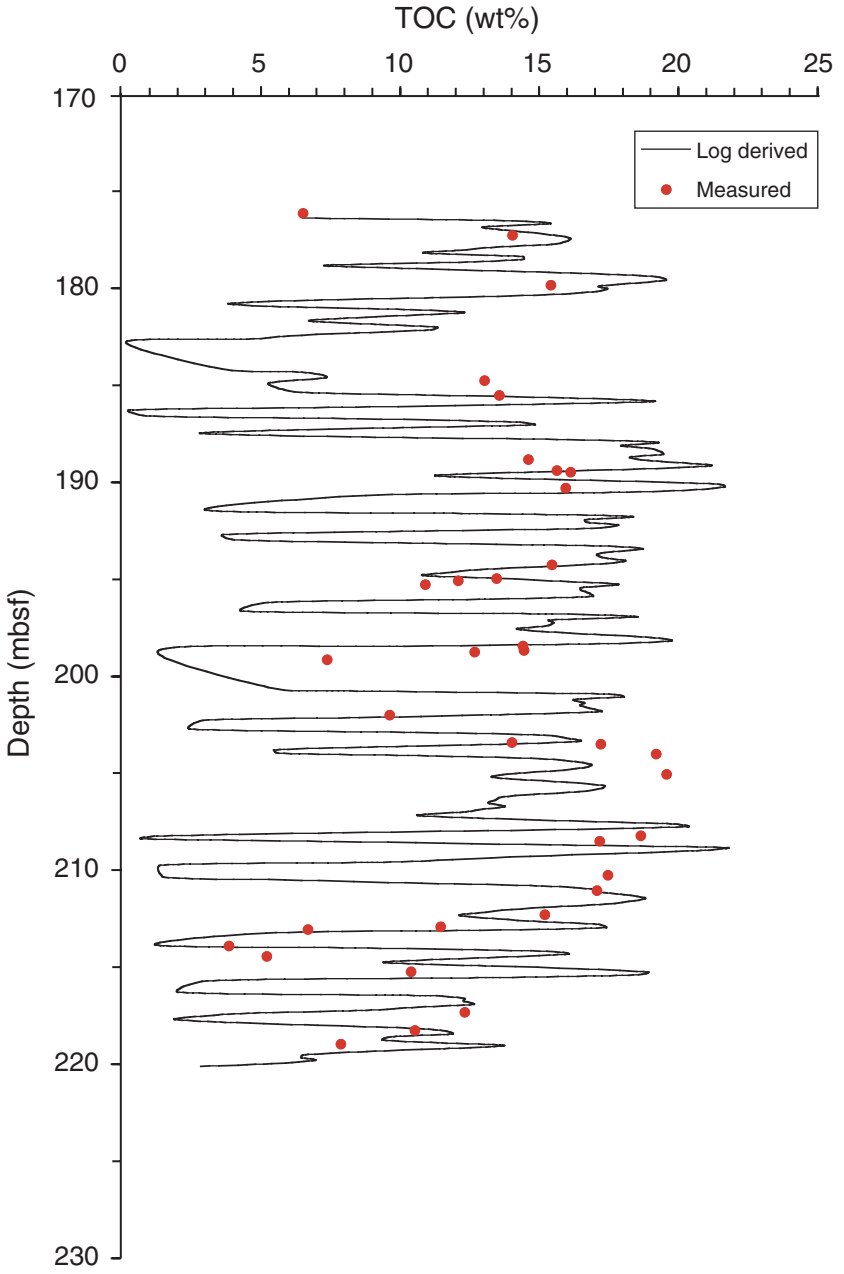

Figure F30. High-resolution MGT gamma ray logs and FMS imagery from the gamma ray spike at 98.5 mbsf in Hole 1257A. CGR = computed gamma ray.

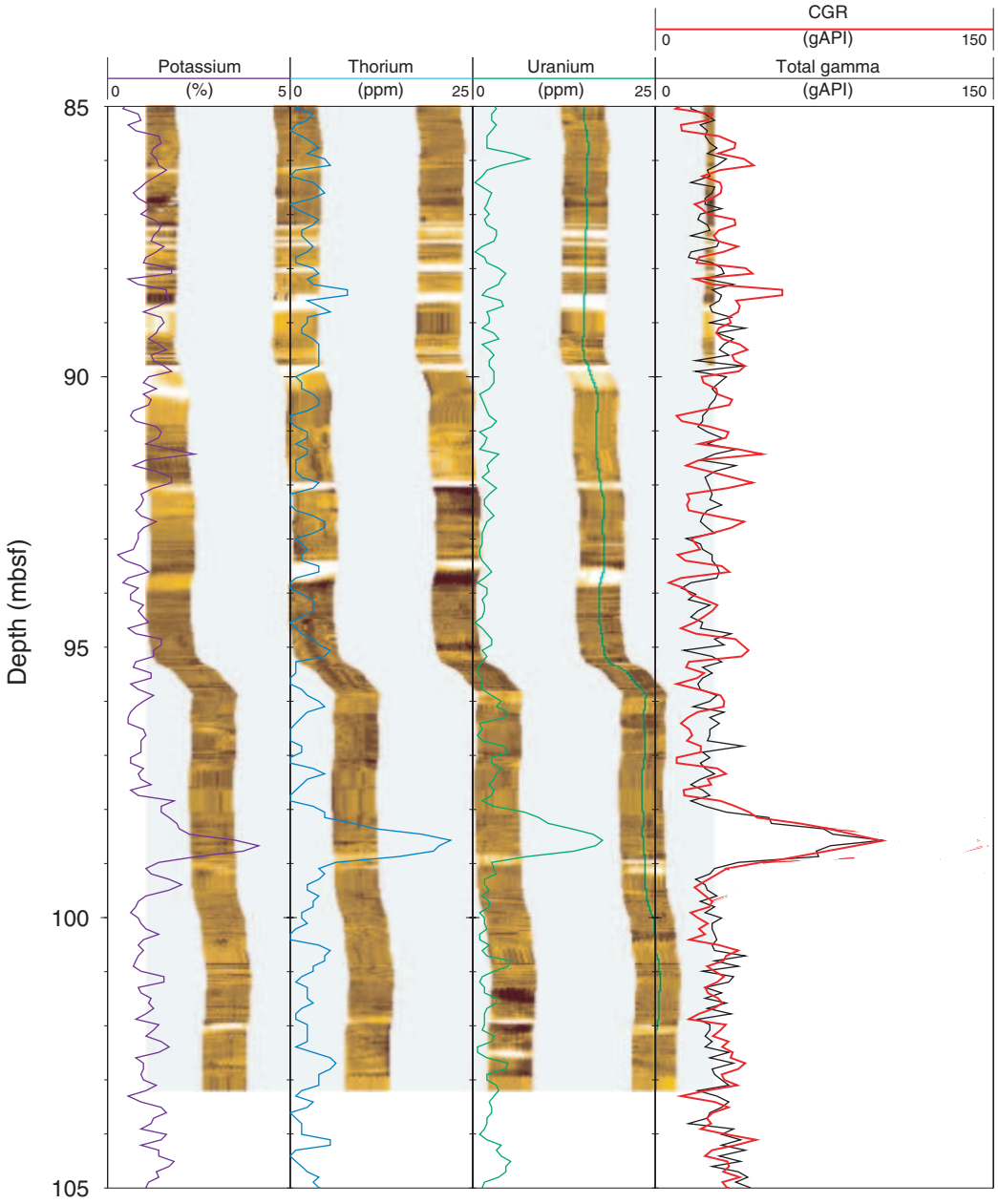

Figure F31. Borehole temperature recorded on the first logging-downhole pass of the TAP tool.

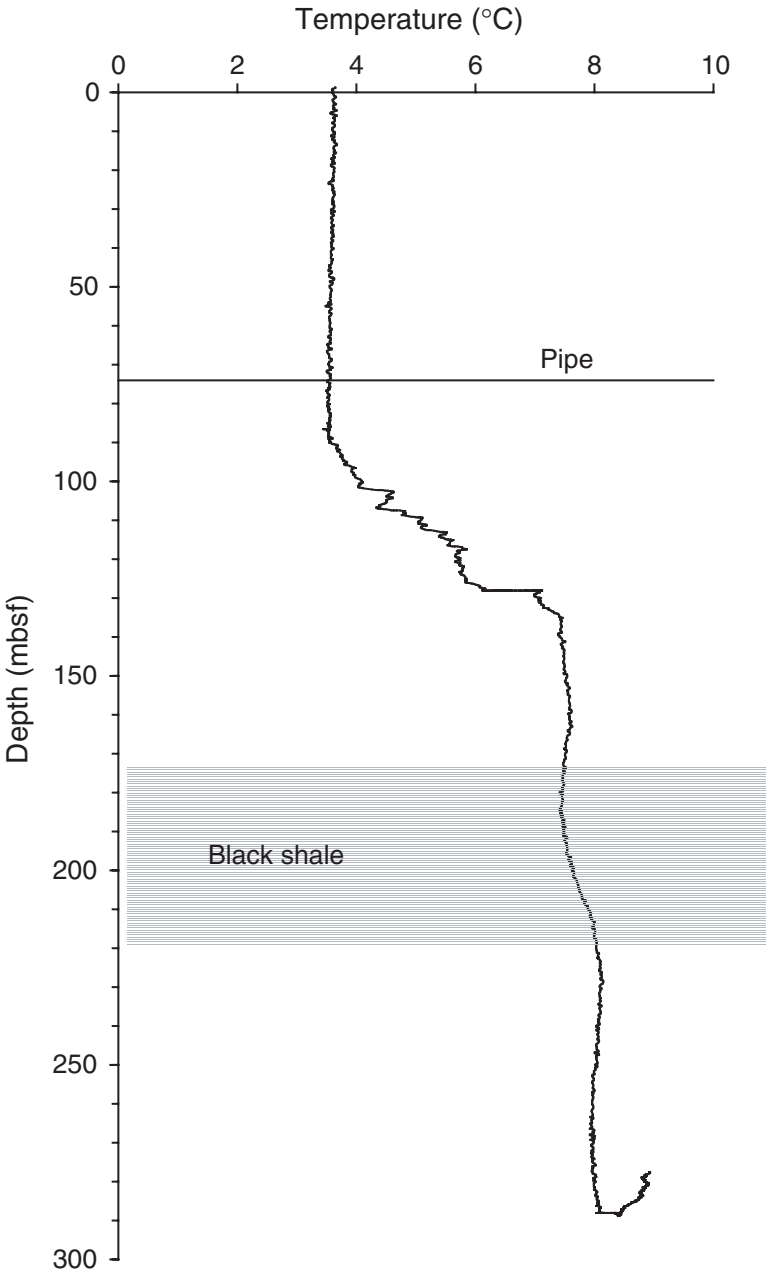

Figure F32. Formation density, velocity, impedance, and reflection coefficient series profiles obtained from downhole logging and core physical property measurements from Hole 1257A. The solid black line on the velocity curve represents interval velocities calculated from the checkshot survey. The logging velocities were shifted by –100 m/s to match the checkshot and laboratory-measured velocity values.

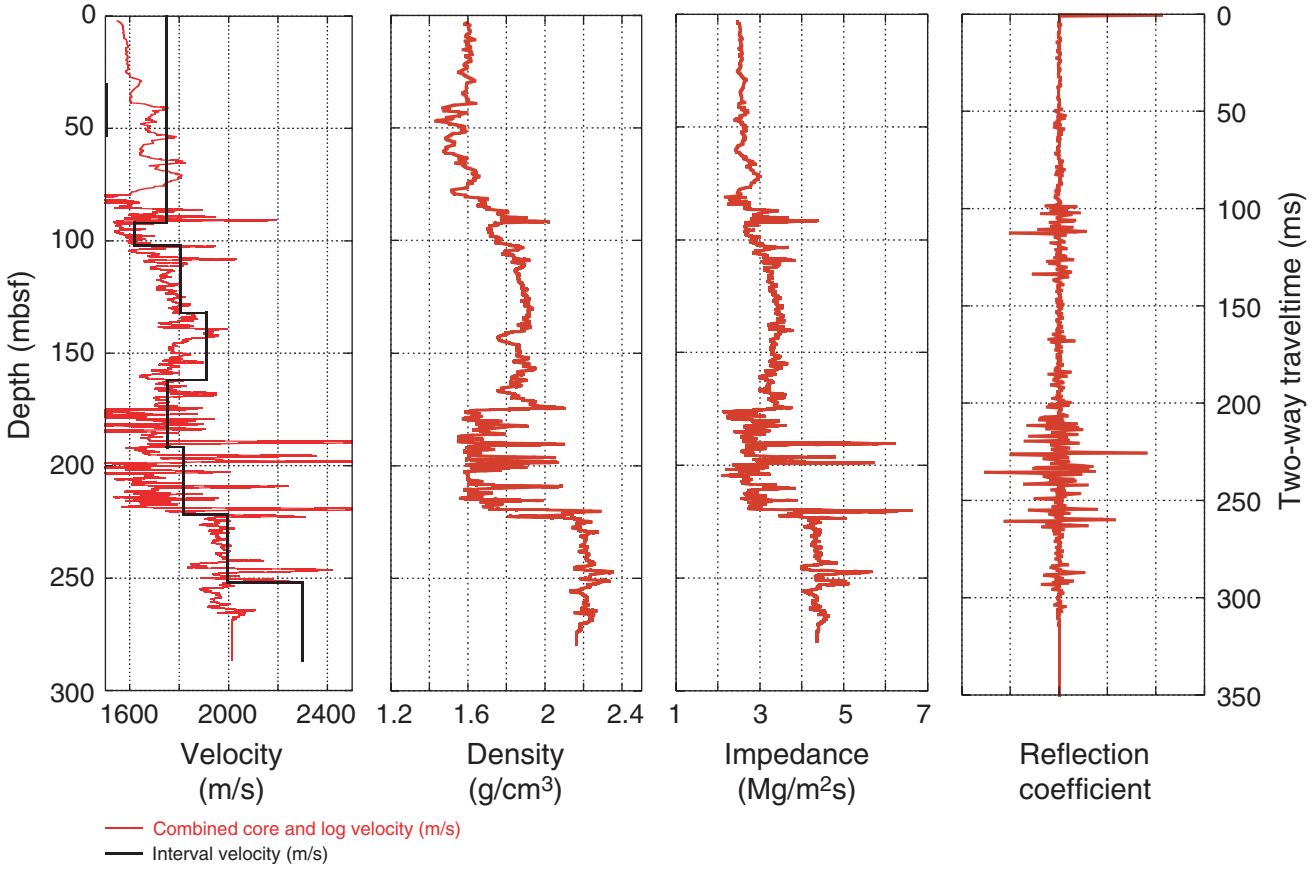

Figure F33. Synthetic seismogram derived from the density and velocity logs in Hole 1257A laid on seismic line M49-4 GeoB01-220 at the position of Site 1257. Adjacent to the seismogram is the impedance profile from which the synthetic seismogram was derived. Reflectors A, B, B′, and C are shown on the seismic profile.

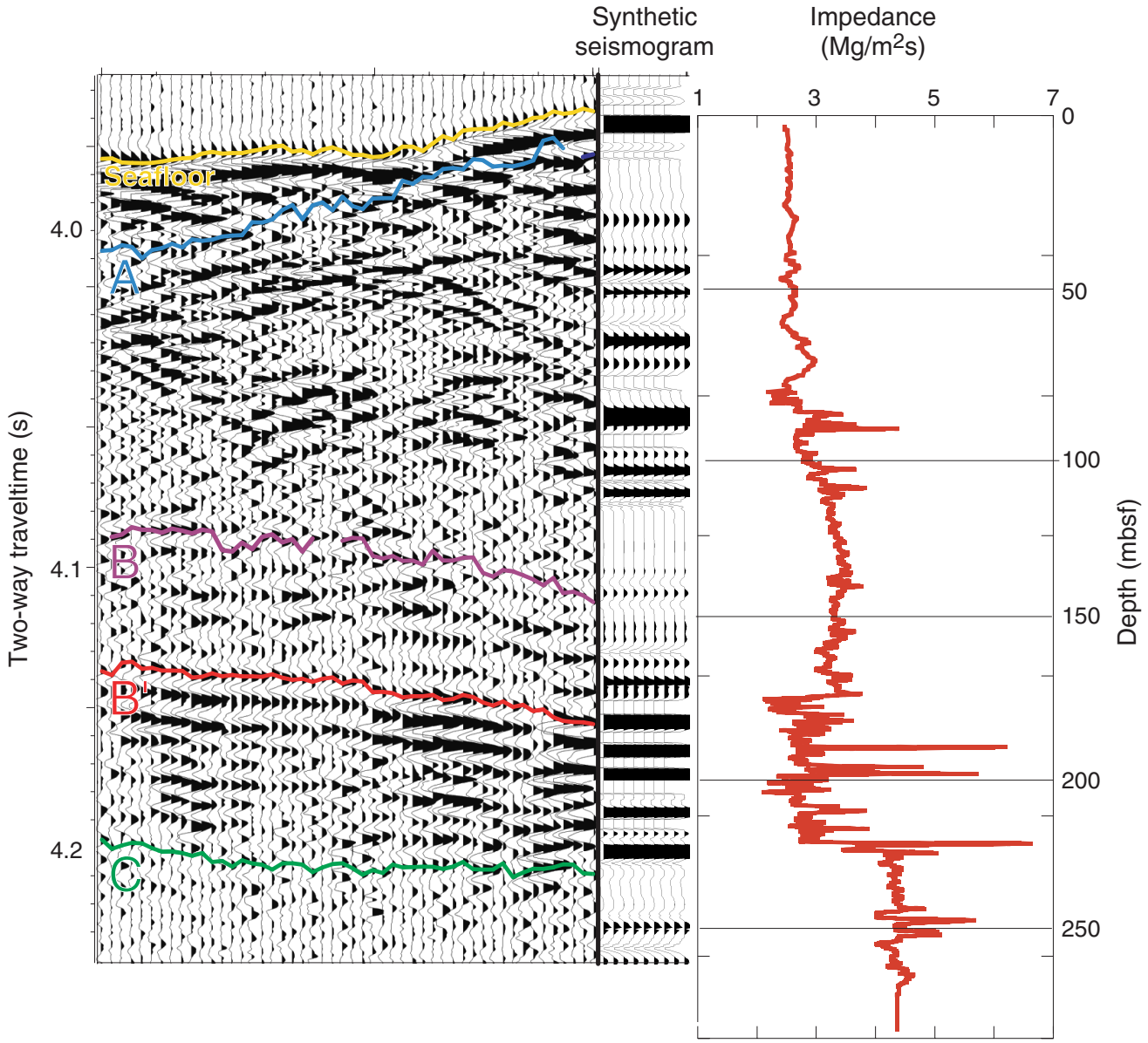

Table T1. Coring summary, Site 1257. (See table note. Continued on next page.)

Hole 1257A
Latitude: 9°27.2302′N
Longitude: 54°20.5184′W
Time on site: 169.25 (1430 hr, 15 Jan–1530 hr, 22 Jan 2003)
Time on hole: 104.25 (1430 hr, 15 Jan–2245 hr, 19 Jan 2003)
Seafloor (drill pipe measurement from rig floor, mbrf): 2961.9
Distance between rig floor and sea level (m): 10.9
Water depth (drill pipe measurement from sea level, m): 2951.0
Total depth (drill pipe measurement from rig floor, mbrf): 3246.6
Total penetration (meters below seafloor, mbsf): 284.7
Total length of cored section (m): 284.7
Total core recovered (m): 216.05
Core recovery (%): 75.9
Total number of cores: 31
Total number of drilled intervals: 0

Hole 1257B
Latitude: 9°27.2184′N
Longitude: 54°20.5075′W
Time on hole: 38.58 (2245 hr, 19 Jan–1320 hr, 21 Jan 2003)
Seafloor (drill pipe measurement from rig floor, mbrf): 2961.9
Distance between rig floor and sea level (m): 10.9
Water depth (drill pipe measurement from sea level, m): 2951.0
Total depth (drill pipe measurement from rig floor, mbrf): 3189.2
Total penetration (meters below seafloor, mbsf): 227.3
Total length of cored section (m): 187.3
Total length of drilled intervals (m): 40.0
Total core recovered (m): 116.23
Core recovery (%): 62.1
Total number of cores: 27
Total number of drilled intervals: 1

Hole 1257C
Latitude: 9°27.2057′N
Longitude: 54°20.4955′W
Time on hole: 26.42 (1320 hr, 21 Jan–1530 hr, 22 Jan 2003)
Seafloor (drill pipe measurement from rig floor, mbrf): 2961.9
Distance between rig floor and sea level (m): 10.9
Water depth (drill pipe measurement from sea level, m): 2951.0
Total depth (drill pipe measurement from rig floor, mbrf): 3197.8
Total penetration (meters below seafloor, mbsf): 235.90
Total length of cored section (m): 153.9
Total length of drilled intervals (m): 82.0
Total core recovered (m): 96.60
Core recovery (%): 62.8
Total number of cores: 16
Total number of drilled intervals: 1

Core	Date (Jan 2003)	Local time (hr)	Depth (mbsf) Top	Depth (mbsf) Bottom	Length (m) Cored	Length (m) Recovered	Recovery (%)	Remarks
207-1257A-								
1H	16	0030	0.0	2.6	2.6	2.59	99.6	
2H	16	0130	2.6	12.1	9.5	9.89	104.1	
3H	16	0315	12.1	21.6	9.5	10.02	105.5	
4H	16	0430	21.6	31.1	9.5	10.00	105.3	
5H	16	0550	31.1	40.6	9.5	9.90	104.2	
6X	16	0825	40.6	44.9	4.3	6.21	144.4	AHC on
7X	16	0925	44.9	54.1	9.2	7.71	83.8	AHC on
8X	16	1030	54.1	63.7	9.6	7.87	82.0	AHC on
9X	16	1210	63.7	73.3	9.6	6.73	70.1	AHC on
10X	16	1315	73.3	83.0	9.7	8.26	85.2	AHC on
11X	16	1515	83.0	92.6	9.6	2.28	23.8	AHC on
12X	16	1645	92.6	102.2	9.6	5.77	60.1	AHC on
13X	16	1850	102.2	111.8	9.6	9.66	100.6	
14X	16	2015	111.8	121.5	9.7	9.08	93.6	
15X	16	2145	121.5	131.1	9.6	9.87	102.8	
16X	16	2255	131.1	140.7	9.6	7.32	76.3	
17X	17	0005	140.7	150.3	9.6	8.43	87.8	
18X	17	0110	150.3	159.7	9.4	9.73	103.5	
19X	17	0310	159.7	169.4	9.7	1.92	19.8	

Table T1 (continued).

Core	Date (Jan 2003)	Local time (hr)	Depth (mbsf) Top	Depth (mbsf) Bottom	Length (m) Cored	Length (m) Recovered	Recovery (%)	Remarks
20X	17	0515	169.4	179.0	9.6	8.71	90.7	
21X	17	0715	179.0	188.6	9.6	1.22	12.7	
22X	17	1025	188.6	198.2	9.6	2.58	26.9	
23X	17	1330	198.2	207.6	9.4	8.52	90.6	
24X	17	1525	207.6	217.2	9.6	4.82	50.2	
25X	17	1745	217.2	226.8	9.6	2.16	22.5	
26X	17	2015	226.8	236.5	9.7	9.94	102.5	
27X	17	2230	236.5	246.2	9.7	7.63	78.7	
28X	18	0045	246.2	255.8	9.6	5.98	62.3	
29X	18	0315	255.8	265.4	9.6	9.91	103.2	
30X	18	0555	265.4	275.1	9.7	9.97	102.8	
31X	18	0920	275.1	284.7	9.6	1.37	14.3	
			Cored totals:		284.7	216.05	75.9	
207-1257B-								
			*****Drilled from 0.0 to 40.0 mbsf*****					
1R	20	1020	40.0	44.8	4.8	3.77	78.5	AHC on
2R	20	1135	44.8	49.8	5.0	4.60	92.0	AHC on
3R	20	1220	49.8	59.4	9.6	5.63	58.7	AHC on
4R	20	1340	59.4	69.0	9.6	6.97	72.6	AHC on
5R	20	1430	69.0	78.7	9.7	4.98	51.3	AHC on
6R	20	1535	78.7	88.3	9.6	1.42	14.8	AHC on
7R	20	1625	88.3	97.9	9.6	3.26	34.0	AHC on
8R	20	1715	97.9	107.6	9.7	8.69	89.6	AHC on
9R	20	1825	107.6	117.2	9.6	9.96	103.8	AHC on
10R	20	1920	117.2	126.8	9.6	9.94	103.5	AHC on
11R	20	2015	126.8	136.2	9.4	9.19	97.8	AHC on
12R	20	2110	136.2	145.8	9.6	9.83	102.4	AHC on
13R	20	2155	145.8	155.5	9.7	8.69	89.6	AHC on
14R	20	2250	155.5	165.1	9.6	1.16	12.1	AHC on
15R	20	2350	165.1	170.1	5.0	0.02	0.4	AHC on
16R	21	0045	170.1	174.4	4.3	0.09	2.1	
17R	21	0205	174.4	179.4	5.0	0.83	16.6	AHC on
18R	21	0255	179.4	183.7	4.3	0.50	11.6	AHC on
19R	21	0335	183.7	188.7	5.0	3.10	62.0	
20R	21	0430	188.7	193.3	4.6	1.48	32.2	
21R	21	0525	193.3	198.3	5.0	2.75	55.0	
22R	21	0615	198.3	203.0	4.7	3.01	64.0	
23R	21	0700	203.0	208.0	5.0	1.95	39.0	
24R	21	0745	208.0	212.6	4.6	4.72	102.6	AHC on
25R	21	0850	212.6	217.6	5.0	2.68	53.6	AHC on
26R	21	1015	217.6	222.3	4.7	2.36	50.2	AHC on
27R	21	1145	222.3	227.3	5.0	4.65	93.0	AHC on
			Cored totals:		187.3	116.23	62.1	
			Drilled total:		40.0			
			Total:		227.3			
207-1257C-								
			*****Drilled from 0.0 to 82.0 mbsf*****					
1R	21	1835	82.0	91.6	9.6	6.35	66.2	AHC on
2R	21	1935	91.6	101.2	9.6	1.28	13.3	AHC on
3R	21	2030	101.2	110.8	9.6	9.45	98.4	AHC on
4R	21	2125	110.8	120.5	9.7	9.90	102.1	
5R	21	2205	120.5	130.1	9.6	6.52	67.9	
6R	21	2250	130.1	139.5	9.4	9.64	102.6	
7R	21	2330	139.5	149.1	9.6	9.53	99.3	
8R	22	0015	149.1	158.7	9.6	9.43	98.2	
9R	22	0115	158.7	168.4	9.7	7.74	79.8	
10R	22	0225	168.4	178.0	9.6	2.82	29.4	
11R	22	0325	178.0	187.7	9.7	1.88	19.4	
12R	22	0440	187.7	197.3	9.6	2.76	28.8	AHC on
13R	22	0535	197.3	207.0	9.7	4.01	41.3	AHC on
14R	22	0635	207.0	216.6	9.6	3.24	33.8	AHC on
15R	22	0805	216.6	226.2	9.6	3.47	36.2	AHC on
16R	22	0940	226.2	235.9	9.7	8.58	88.5	AHC on
			Cored totals:		153.9	96.60	62.8	
			Drilled total:		82.0			
			Total:		235.9			

Note: AHC = active heave compensator.

Table T2. Lithostratigraphic units and subunits, Site 1257.

Unit/ subunit	Hole, core, section, interval (cm)	Depth (mbsf)	Thickness (m)	Age	Lithology
	207-				
I	1257A-1H-1, through 1H-2, 7	0–1.57	1.57	late Neogene	Nannofossil clay
IIA	1257A-1H-1, 7, through 4H-2, 75	1.57–23.85	22.28	early Oligocene	Nannofossil ooze with foraminifers; nannofossil chalk with foraminifers
IIB	1257A-4H-2, 75, through 10X-3, 55 1257B-1R-1, 0, through 6R-1, 0 1257C-1R-1, 0, through 1R-3, 95	23.85–76.85 <40.00–78.70 <82.00–85.95	53.00	early Oligocene–early Eocene	Siliceous nannofossil chalk with foraminifers to nannofossil chalk with siliceous microfossils and foraminifers
IIIA	1257A-10X-3, 55, through 16X-CC, 63 1257B-6R-1, 0, through 12R-7, 60 1257C-1R-3, 95, through 7R-5, 15	76.85–140.70 78.70–145.81 85.95–145.15	66.80	late Paleocene–middle Paleocene	Nannofossil chalk; foraminifer nannofossil chalk
IIIB	1257A-16X-CC, 63, through 20X-4, 52 1257B-12R-7, 60, through 17R-1, 17 1257C-7R-5, 15, through 11R-1, 3	140.70–174.42 145.81–174.57 145.15–178.03	33.80	early Maastrichtian–early Campanian	Foraminifer nannofossil chalk
IV	1257A-20X-4, 52, through 26X-1, 0 1257B-17R-1, 17, through 25R-2, 112 1257C-11R-1, 3, through 15R-CC, 39	174.42–226.80 174.57–217.60 178.03–226.20	52.60	Santonian–middle Cenomanian	Calcareous claystone with organic matter; clayey chalk with organic matter; limestone
V	1257A-26X-1, 0, through 31X-CC, 56 1257B-25R-2, 112, through 27R-CC, 22 1257C-15R-CC, 39, through 16R-CC, 18	226.80–284.67 217.60–227.30 226.20–235.88	47.20	mid–late Albian	Silty calcareous claystone to clayey carbonate siltstone

Table T3. Datum levels for calcareous nannofossils, Site 1257.

Core, section, interval (cm)	Depth (mbsf)		Depth (mcd)		Datum	Species	Zone	Age	Age (Ma)
	Top	Bottom	Top	Bottom					
207-1257A-									
1H-1, 25–26	0.00	0.25	0.00	0.25	T	*Amaurolithus delicatus*	NN13–NN15	late Miocene	4.6
1H-2, 4.5–5.5	0.25	1.55	0.25	1.55	T	*Discoaster quinqueramus*	NN11	late Miocene	5.6
1H-CC, 25–30	2.54	2.84	2.54	2.84	B	*Sphenolithus distentus*	NP23	early Oligocene	30.4
2H-1, 24–25	2.54	2.84	2.54	2.84	T	*Dictyococcites bisectus*	NP23	early Oligocene	25.5
2H-CC, 24–29	11.83	12.44	11.83	12.44	T	*Reticulofenestra umbilica*	NP22	early Oligocene	31.7
3H-CC, 35–39	21.60	22.08	21.60	22.08	T	*Ericsonia formosa*	NP21	earliest Oligocene	32.9
4H-CC, 23–27	29.15	31.56	29.15	31.56	T	*Ericsonia obruta*	NP21	earliest Oligocene	32.2
6X-2, 104–105	42.75	43.14	42.75	43.14	T	*Discoaster saipanensis*	NP20	late Eocene	34.0
6X-2, 104–105	43.14	43.84	43.14	43.84	B	*Dictyococcites bisectus*	NP20	late Eocene	38.5
6X-2, 104–105	42.75	43.14	42.75	43.14	T	*Cribrocentrum reticulatum*	NP20	late Eocene	34.9
6X-3, 24–25	43.14	43.84	43.14	43.84	T	*Chiasmolithus grandis*	NP17	middle Eocene	37.1
6X-CC, 21–26	46.76	52.56	46.76	52.56	B	*Reticulofenestra umbilica*	NP17	middle Eocene	42.5
8X-CC, 31–36	52.56	61.92	52.56	61.92	T	*Chiasmolithus grandis*	NP16	middle Eocene	37.1
9X-4, 25–26	61.92	68.45	61.92	68.45	T	*Chiasmolithus solitus*	NP16	middle Eocene	40.4
10X-CC, 46–51	81.51	84.74	81.51	84.74	B	*Sphenolithus radians*	NP12/NP13	early Eocene	53.3
10X-CC, 46–51	70.38	81.51	70.38	81.51	T	*Discoaster multiradiatus*	NP12/NP13	early Eocene	53.0
13X-CC, 31–36	111.81	120.83	111.81	120.83	B	*Heliolithus riedelii*	NP8	late Paleocene	57.3
13X-CC, 31–36	111.81	120.83	111.81	120.83	B	*Discoaster multiradiatus*	NP8	late Paleocene	56.2
15X-CC, 39–44	131.32	138.37	130.91	142.00	B	*Discoaster mohleri*	NP8	late Paleocene	57.5
16X-CC, 58–63	131.32	138.37	130.91	142.00	T	*Fasciculithus pileatus*	NP5	late Paleocene	58.2
17X-1, 25–26	138.37	140.95	142.00	146.42	T	*Reinhardtites levis*	CC24	middle Maastrichtian	69.2
20X-1, 25–26	169.65	170.49	175.45	176.29	B	*Reinhardtites levis*	CC22	late Campanian	75.7
20X-1, 25–26	169.65	170.49	175.45	176.29	B	*Uniplanarius trifidum*	CC22	late Campanian	76.0
20X-5, 0	173.90	175.40	179.70	181.20	T	*Marthasterites furcatus*	CC16/CC17	Campanian/Santonian	80.6
21X-CC, 25	179.00	180.15	184.80	185.95	T	*Lithastrinus septenarius*	CC15/CC16	Santonian	84.7
24X-CC, 42	212.42	219.26	218.22	225.06	B	*Eiffellithus turriseiffelii*	CC10/CC11	Turonian	101.7
29X-CC, 41–46	265.66	271.40	271.46	277.20	B	*Tranolithus orionatus*	NC8	Albian	107.3
207-1257B-									
4R-CC, 16–21	66.32	73.90	73.43	76.95	B	*Tribrachiatus orthostylus*	NP12	early Eocene	53.4
6R-CC, 10–15	73.90	80.07	76.95	84.44	T	*Fasciculithus tympaniformis*	NP9	late Paleocene	54.1
9R-CC, 30–35	117.51	127.09	119.28	129.67	B	*Discoaster mohleri*	NP7	late Paleocene	57.5
12R-6, 78	144.49	145.31	147.16	147.98	B	*Fasciculithus ullii*	NP4/NP5	middle Paleocene	60.0
12R-7, 44	145.31	145.65	147.98	148.32	T	*Arkhangelskiella cymbiformis*	CC25	middle Maastrichtian	65.0
16R-CC, 4–9	165.10	170.14	168.30	173.34	T	*Uniplanarius trifidum*	CC23	late Campanian~	71.3
17R-1, 0	174.40	186.66	173.34	189.86	B	*Uniplanarius trifidum*	CC23	late Campanian~	76.0
20R-CC, 21	186.66	190.23	189.86	196.36	T	*Lithastrinus septenarius*	CC14	Coniacian	84.7
22R-CC, 19–21	201.29	204.61	207.42	210.74	B	*Lithastrinus septenarius*	CC13	Coniacian	88.8
207-1257C-									
1R-5, 50	88.00	88.28	88.00	88.28	B	*Discoaster multiradiatus*	NP9	early Eocene	56.2
7R-1, 0	139.50	141.00	141.95	143.45	B	*Heliolithus kleinpellii*	NP7	late Paleocene	58.2
7R-5. 23	145.23	145.40	147.68	147.85	B	*Ellipsolithus macellus*	NP4	early Paleocene	62.2
7R-5, 47	145.40	145.47	147.85	147.92	T	*Arkhangelskiella cymbiformis*	CC24	early Maastrichtian~late Campanian	65.0

Note: T = top, B = bottom.

Table T4. Distribution of planktonic foraminifers, Hole 1257A. (This table is available in an **oversized format.**)

Table T5. Datum levels for planktonic foraminifers, Site 1257.

Core, section, interval (cm)	Depth (mbsf) Top	Depth (mbsf) Bottom	Depth (mcd) Top	Depth (mcd) Bottom	Datum	Species	Zone	Age	Age (Ma)
207-1257A-									
3H-2, 50–54	12.60	14.10	12.60	14.10	T	*Pseudohastigerina micra*	P18	early Oligocene	32.0
6X-3, 50–52	42.60	44.10	42.60	44.10	T	*Acarinina* spp.*	P14	middle Eocene	37.5–38.5
6X-3, 50–52	42.60	44.10	42.60	44.10	T	*Morozovella spinulosa**	P14	middle Eocene	37.9
7X-4, 47–51	48.39	49.87	48.39	49.87	T	*Orbulinoides beckmanni*	P13	middle Eocene	40.1
8X-2, 47–48	56.07	57.61	56.07	57.61	B	*Orbulinoides beckmanni*	P13	middle Eocene	40.5
9X-5, 50–54	68.70	69.70	68.70	69.70	T	*Morozovella aragonensis*	P11	middle Eocene	43.6
9X-CC, 43–48	69.70	70.38	69.70	70.38	T	*Morozovella subbotinae**	P6	early Eocene	50.8
9X-CC, 43–48	69.70	70.38	69.70	70.38	T	*Morozovella marginodentata**	P6	early Eocene	52.3
10X-2, 50–54	73.80	75.30	73.80	75.30	T	*Morozovella formosa*	P6	early Eocene	54.0
11X-1, 49–54	83.49	84.61	83.49	84.61	B	*Igorina broedermanni*	P6	early Eocene	54.7
11X-1, 49–54	83.49	84.61	83.49	84.61	B	*Morozovella gracilis*	P6	early Eocene	54.9
11X-1, 49–54	83.49	84.61	83.49	84.61	B	*Morozovella marginodentata*	P6	early Eocene	54.8
11X-2, 27–32	83.49	84.61	83.49	84.61	T	*Morozovella velascoensis* group	P5	early Eocene	54.7
12X-2, 50–54	93.10	94.60	93.10	94.60	T	*Globanomalina pseudomenardii*	P4	late Paleocene	55.9
15X-CC, 39–44	131.32	131.60	130.91	131.19	B	*Acarinina soldadoensis*	P4	late Paleocene	56.5
16X-4, 49–52	136.09	137.50	139.72	141.13	B	*Globanomalina pseudomenardii*	P4	late Paleocene	59.2
16X-CC, 58–63	138.37	141.20	142.00	144.83	B	*Morozonella velascoensis**	P3	late Paleocene	60.0
17X-1, 50–54	138.37	141.20	143.84	146.67	T	*Globotruncana* spp.*	KS31–KS30	Maastrichtian–Campanian	65.0
18X-CC, 27–32	159.98	161.58	165.78	167.38	B	*Globotruncana aegyptiaca**	KS29–KS30	late Campanian	73.8
21X-CC, 0–5	179.90	190.60	185.70	196.40	B	*Contusotruncana fornicata**	Not defined	Santonian	88.0
25X-CC, 36–46	218.85	219.26	224.65	225.06	T	*Rotalipora* spp.*	KS19	late Cenomanian	94.0
207-1257B-									
1R-2, 47–49	40.00	41.97	41.37	43.34	T	*Hantkenina* spp.	P16	late Eocene	33.7
1R-3, 74–77	41.97	43.74	43.34	45.11	T	*Acarinina* spp.*	P14	middle Eocene	37.5–38.5
3R-CC, 21–26	49.35	55.38	52.72	58.75	T	*Morozovella aragonensis*	P11	middle Eocene	43.6
4R-CC, 16–21	55.38	66.32	62.49	73.43	T	*Morozovella gracilis**	P6	early Eocene	54.9
4R-CC, 16–21	55.38	66.32	62.49	73.43	T	*Morozovella formosa**		early Eocene	54.0
6R-CC, 10–15	73.90	80.07	76.95	84.44	T	*Morozovella velascoensis* group	P5	early Eocene	54.7
7R-1, 29–31	88.59	91.15	92.96	95.52	B	*Morozovella subbotinae*	P5	late Paleocene	
7R-CC, 21–26	91.51	106.54	95.88	109.97	B	*Acarinina soldadoensis*	P4	late Paleocene	56.5
8R-CC, 21–26	91.51	106.54	95.88	109.97	T	*Globanomalina pseudomenardii*	P4	late Paleocene	55.9
11R-CC, 5–10	135.94	145.98	138.52	148.65	B	*Globanomalina pseudomenardii**	P4	late Paleocene	59.2
12R-CC, 17–22	135.94	145.98	138.61	148.65	T	*Globotruncana* spp.*	KS30	early Maastrichtian–late Campanian	65.0
16R-CC, 4–9	170.14	186.66	173.34	189.86	B	*Globotruncana aegyptiaca**	KS29~	late Campanian~	73.8
207-1257C-									
1R-CC, 14–19	86.23	88.28	86.23	88.28	T	*Morozovella velascoensis* group	P5	early Eocene	54.7
4R-CC, 15–20	110.60	120.65	112.60	123.05	T	*Globanomalina pseudomenardii*	P4	late Paleocene	55.9
6R-7, 59–64	139.69	148.98	140.89	151.43	B	*Globanomalina pseudomenardii**	P4	late Paleocene	59.2
7R-CC, 19–24	139.69	148.98	140.89	151.43	T	*Globotruncana* spp.*	KS30	early Maastrichtian~late Campanian	65.0
8R-CC, 16–21	158.48	166.39	160.93	168.80	B	*Globotruncana aegyptiaca*	KS30	early Maastrichtian~late Campanian	73.8

Notes: Top and bottom depths refer to the range of possible depth in the core within which the datum is believed to fall. T = top, B = bottom. * = probable incomplete range.

Table T6. Distribution of calcareous nannofossils, Site 1257. (See table notes. Continued on next page.)

Core, section, interval (cm)	Depth (mbsf)	Zone	Age	Preservation	Abundance
207-1257A-					
1H-1, 26	0.26	NN11	late Miocene	M	C
1H-2, 4	1.54	NN11	late Miocene	M	C
1H-CC, 30	2.59	NP23	early Oligocene	G	A
2H-7, 23	11.83	NP23	early Oligocene	M	C
2H-CC, 24	12.44	NP22	early Oligocene	G	A
3H-1, 25	12.35	NP22	early Oligocene	G	A
3H-7, 50	21.60	NP22	early Oligocene	G	A
3H-CC, 35	22.08	NP21	early Oligocene	M	C
4H-6, 25	29.15	NP23	early Oligocene	G	A
4H-CC, 23	31.56	NP21	early Oligocene	G	A
5H-3, 25	34.35	NP22	early Oligocene	G	A
5H-6, 25	38.85	NP21	early Oligocene	G	A
5H-CC, 21	40.70	NP21	early Oligocene	P	F
6X-1, 25	40.85	NP21	early Oligocene		
6X-2, 25	42.35	NP21	early Oligocene		
6X-2, 65	42.75	NP21	early Oligocene	G	A
6X-CC, 21	46.76	NP17	middle Eocene	M	C
7X-CC, 20	52.56	NP17	middle Eocene	P	F
8X-CC, 31	61.92	NP16 top	middle Eocene	P	F
9X-4, 25	68.45	NP16 top	middle Eocene	G	A
9X-4, 95	69.15	NP16 top	middle Eocene	G	A
9X-5, 25	69.45	NP16 top	middle Eocene	G	A
9X-CC, 43	70.38	NP11	early Eocene		
10X-CC, 46	81.51	NP11 lower	early Eocene		
11X-2, 40	84.74	NP9 top	late Paleocene/early Eocene	G	A
11X-CC, 46	85.20	Not defined	No age assignment	P	R
12X-CC, 47	98.32	NP9 top	late Paleocene/early Eocene		
13X-CC, 31	111.81	NP8	late Paleocene		
14X-CC, 12	120.83	NP8	late Paleocene		
15X-CC, 39	131.32	NP8	late Paleocene		
16X-CC, 58	138.37	NP5	late Paleocene	M	
17X-1, 25	140.95	CC24	middle Maastrichtian	G	A
17X-1, 102	141.72	CC24	middle Maastrichtian	M	F
17X-5, 102	147.68	CC23	Maastrichtian/Campanian	M	C
17X-6, 25	148.11	CC23	Maastrichtian/Campanian	M	F
17X-CC, 59	149.08	CC23	Maastrichtian/Campanian	M	C
18X-CC, 27	159.98	CC23	Maastrichtian/Campanian	M	F
19X-1, 25	159.95	CC23	Maastrichtian/Campanian	M	A
19X-CC, 38	161.58	CC23	Maastrichtian/Campanian		
20X-1, 0	169.40	CC22	middle Campanian	M	C
20X-1, 26	169.66	CC22	middle Campanian	G	A
20X-2, 0	170.90	CC22	middle Campanian	M	C
20X-2, 102	171.92	CC22	middle Campanian	G	A
20X-3, 0	172.40	CC17/CC18	early Campanian	M	C
20X-4, 0	173.90	CC17/CC18	early Campanian	P	F
20X-5, 0	175.40	CC16/CC17	Campanian/Santonian	P	F
21X-1, 0	179.00	CC15/CC16	Santonian	P	F
21X-CC, 0	179.90	CC15/CC16	Santonian	P	F
22X-2, 0	190.10	CC14	Coniacian	P	F
22X-CC, 15	190.88	CC13	Coniacian	P	R
23X-CC, 19	206.67	CC12	Turonian	G	A
24X-CC, 22	212.22	CC10/CC11	Turonian	G	A
25X-CC, 36	219.26	Barren	No age assignment		
26X-CC, 43	236.69	Barren	No age assignment		
27X-4, 143	242.43	NC8	late Albian	M	F
28X-CC, 41	252.13	NC8	late Albian	M	F
29X-CC, 41	265.66	NC8	Albian	M	C
30X-5, 0	271.40	NC8	Albian	M	F
30X-6, 0	272.90	NC8	Albian	M	F
30X-CC, 38	275.32	NC8	Albian	M	C
31X-CC, 51	276.42	NC8	Albian	P	R
207-1257B-					
3R-CC, 21	55.38	NP16	middle Eocene		
4R-CC, 16	66.32	NP12	early Eocene	P	A

Table T6 (continued).

Core, section, interval (cm)	Depth (mbsf)	Zone	Age	Preservation	Abundance
5R-CC, 12	73.90	NP9	early Eocene		
6R-CC, 10	80.07	NP9	late Paleocene		
7R-1, 9	88.39	NP9	late Paleocene		
7R-1, 43	88.73	NP9 below	late Paleocene	G	A
7R-CC, 21	91.51	NP9	late Paleocene		
8R-CC, 21	106.54	NP8/NP7	late Paleocene		
9R-CC, 30	117.51	NP7	late Paleocene		
10R-CC, 10	127.09	NP7	late Paleocene		
11R-CC, 5	135.94	NP7	late Paleocene		
12R-3, 150	140.70	NP7	late Paleocene		
12R-6, 78	144.49	NP4/NP5	late Paleocene	M	C
12R-6, 150	145.21	CC24	Maastrichtian	M	A
12R-7, 10	145.31	CC24	Maastrichtian	M	A
12R-CC, 17	145.98	CC24	Maastrichtian	M	C
13R-CC, 0	154.43	CC23	late Campanian		
14R-1, 116	156.66	CC22/CC23	late Campanian		
15R-1, 2	165.12	CC23	late Campanian	M	C
16R-CC, 9	170.19	CC23	late Campanian	M	C
19R-CC, 14	186.66	CC15–CC16	Santonian–Campanian	P	F
20R-CC, 8	190.10	CC13	Coniacian	P	F
21R-CC, 18	196.02	CC13	Coniacian	M	C
22R-CC, 19	201.29	CC13	Coniacian	M	F
23R-2, 70	204.61	CC12	Turonian	M	C
24R-4, 55	212.51	CC10–CC11	Cenoman–Turonian	M	C
25R-1, 149	214.10	CC10–CC11	Cenoman–Turonian	M	C
207-1257C-					
1R-3, 0	85.00	NP9 upper	early Eocene	G	A
1R-5, 40	87.90	NP9 upper	early Eocene	G	A
1R-5, 50	88.00	NP9 upper	early Eocene	G	A
1R-CC, 14	88.28	NP9 lower	late Paleocene	G	A
2R-CC, 8	92.83	NP9 lower	late Paleocene	G	A
3R-CC, 19	110.60	NP7	late Paleocene	G	A
4R-CC, 15	120.65	NP7	late Paleocene		
5R-CC, 8	126.97	NP7	late Paleocene		
6R-7, 59	139.69	NP7	late Paleocene		
7R-1, 0	139.50	NP7	late Paleocene		
7R-2, 0	141.00	NP6	late Paleocene		
7R-5, 23	145.23	NP4	late Paleocene	P	R
7R-5, 40	145.40	NP4	late Paleocene	M	F
7R-5, 47	145.47	CC24	Maastrichtian	M	C
7R-5, 120	146.20	CC24	Maastrichtian	M	C
8R-CC, 16	158.48	CC22/CC23	early Maastrichtian~late Campanian	M	C
9R-CC, 14	166.39	CC22	late Campanian	G	A
10R-CC, 16	171.17	CC22	late Campanian	M	A
12R-CC, 20	190.40	CC13	Coniacian	G	A
13R-CC, 20	201.30	CC13	Coniacian	M	C
14R-CC, 0	210.03	CC10–CC12	Cenoman-Turon	G	A
15R-4, 36	219.44	CC10	Cenoman		
15R-CC, 39	220.07	CC10	Cenoman		
16R-CC, 12	234.72	CC9	Albian		

Notes: Preservation: G = good, M = moderate, P = poor. Abundance: A = abundant, C = common, F = few, R = rare.

Table T7. Distribution of planktonic foraminifers, Hole 1257B. (Continued on next two pages.)

Core, section, interval (cm)	Depth (mbsf)	Zone	Age	Preservation	Abundance	*Favusella washitensis*	*Globigerinelloides bentonensis*	*Hedbergella delrioensis*	*Hedbergella planispira*	*Heterohelix moremani*	*Globigerinelloides caseyi*	*Heterohelix reussi*	*Hastigerinoides watersi*	*Heterohelix globulosa*	*Whiteinella baltica*	*Costellagerina libyca*	*Hedbergella amabilis*	*Dicarinella imbricata*	*Whiteinella inornata*	*Clavihedbergella simplex*	*Hastigerinoides subdigitata*	*Archaeoglobigerina cretacea*	*Contusotruncana fornicata*	*Globotruncana aegyptiaca*	*Globotruncana arca*	*Globotruncana esnehensis*	*Globotruncanella havanensis*	*Globotruncanita stuarti*	*Globigerinelloides prairiehillensis*	*Pseudoguembelina costulata*	*Rugoglobigerina rugosa*	*Rugotruncana subcircumnodifer*	*Archaeoglobigerina blowi*	*Globotruncana linneiana*	*Laeviheterohelix glabrans*	*Globotruncana ventricosa*	*Contusotruncana plummerae*	*Gansserina gansseri*	*Rugoglobigerina pennyi*	*Chiloguembelina wilcoxensis*
207-1257B-																																							
1R-1, 0–1	40.00	P18	early Oligocene	P	F																																		X
1R-2, 47–49	41.97	P16	late Eocene	G	A																																		
1R-3, 74–77	43.74	P14	middle Eocene	G	A																																		
2R-CC, 14–19	49.35	P14	middle Eocene	M	F																																		
3R-CC, 21–26	55.38	P11	middle Eocene	M	C																																		
4R-CC, 16–21	66.32	P6	early Eocene	P	C																																		X
5R-CC, 12–17	73.90	P6	early Eocene		B																																		
6R-CC, 10–15	80.07	P5	early Eocene	P	C																																		
7R-1, 29–31	88.59	P5	late Paleocene	P	C																																		
7R-CC, 21–26	91.51	P4	late Paleocene	G	C																																		
8R-CC, 21–26	106.54	P4	late Paleocene	M	C																																		
9R-CC, 30–35	117.51	P4	late Paleocene	G	C																																		
10R-CC, 10–15	127.09	P4	late Paleocene	G	C																																		
11R-CC, 5–10	135.94	P4	late Paleocene	G	C																																		X
12R-CC, 17–22	145.98	KS30	early Maastrichtian–late Campanian	P	F																				X				X	X		X			X	X	X	X	
13R-CC, 0–6	154.43	KS29~	late Campanian~	M	C																		X	X				R		X	X			X	X	X			
14R-1, 111–116	156.61	KS29~	late Campanian~	P	F																				X					X			X	X	X	X			
15R-1, 0–2	165.10	KS29~	late Campanian~	P	C																	X	X	X	X				X	X	X	X							
16R-CC, 4–9	170.14	KS29~	late Campanian~	P	R																	X	X	X	X	X	X	X			X	X							
19R-CC, 14–16	186.66	Not defined	Coniacian	M	F					X				X			X		X	X	X																		
20R-CC, 8–11	190.10	Not defined	Coniacian	G	F							X		X	X			X	X																				
21R-CC, 18–20	196.02	Not defined	No age assignment	M	R			X	X					X	X																								
22R-CC, 19–21	201.29	Not defined	No age assignment	G	F			X				X		X	X	X	X																						
23R-2, 70–71	204.61	Not defined	No age assignment	P	F			X				X	X	X	X																								
24R-4, 55–56	212.51	Not defined	Turonian?	M	R			X			X	X																											
25R-1, 149–150	214.09	Not defined	No age assignment	P	R			X		X																													
26R-CC, 18–20	219.94				B																																		
27R-CC, 20–23	226.92	Not defined	Albian?	P	R	X	X	X	X																														

Notes: Preservation: G = good, M = moderate, P = poor. Abundance: A = abundant, C = common, F = few, R = rare, B = barren.

Table T7 (continued).

Core, section, interval (cm)	Depth (mbsf)	Zone	Age	Preservation	Abundance	*Globanomalina pseudomenardii*	*Morozovella acuta*	*Morozovella aequa*	*Morozovella apanthesma*	*Morozovella occlusa*	*Morozovella velascoensis*	*Subbotina triangularis*	*Subbotina triloculinoides*	*Subbotina velascoensis*	*Acarinina mckannai*	*Acarinina nitida*	*Acarinina coalingensis*	*Acarinina soldadoensis*	*Globanomalina planoconica*	*Morozovella edgari*	*Morozovella subbotinae*	*Subbotina patagonica*	*Planorotalites pseudoscitula*	*Pseudohastigerina micra*	*Acarinina esnaensis*	*Acarinina wilcoxensis*	*Morozovella gracilis*	*Turborotalia praecentralis*	*Acarinina bullbrooki*	*Acarinina rohri*	*Igorina broedermanni*	*Morozovella aragonensis*	*Morozovella spinulosa*	*Muricoglobigerina senni*	*Subbotina boweri*	*Acarinina praetopilensis*	*Globigerinatheka mexicana*	*Globigerinatheka tropicalis*	*Turborotalia pomeroli*	*Turborotalia cerroazulensis*
207-1257B-																																							
1R-1, 0–1	40	P18	early Oligocene	P	F																																		
1R-2, 47–49	41.97	P16	late Eocene	G	A																			X														X	X
1R-3, 74–77	43.74	P14	middle Eocene	G	A																									X								X	X
2R-CC, 14–19	49.35	P14	middle Eocene	M	F																									X		X	X		X	X	X	X	
3R-CC, 21–26	55.38	P11	middle Eocene	M	C																								X	X	X	X	X	X					
4R-CC, 16–21	66.32	P6	early Eocene	P	C											X		X			X			X	X	X	X												
5R-CC, 12–17	73.9	P6	early Eocene		B																																		
6R-CC, 10–15	80.07	P5	early Eocene	P	C		X	X		X		X	X			X		X					X	X														
7R-1, 29–31	88.59	P5	late Paleocene	P	C		X	X			X			X			X	X	X	X	X	X																
7R-CC, 21–26	91.51	P4	late Paleocene	G	C		X	X	X	X	X	X	X	X			X	X																				
8R-CC, 21–26	106.54	P4	late Paleocene	M	C	X	X	X	X	X		X	X	X		X																						
9R-CC, 30–35	117.51	P4	late Paleocene	G	C	X	X	X	X	X	X	X		X																								
10R-CC, 10–15	127.09	P4	late Paleocene	G	C	X	X	X			X	X		X	X																								
11R-CC, 5–10	135.94	P4	late Paleocene	G	C	X	X	X	X	X	X	X	X	X																								
12R-CC, 17–22	145.98	KS30	early Maastrichtian–late Campanian	P	F																																		
13R-CC, 0–6	154.43	KS29~	late Campanian~	M	C																																		
14R-1, 111–116	156.61	KS29~	late Campanian~	P	F																																		
15R-1, 0–2	165.1	KS29~	late Campanian~	P	C																																		
16R-CC, 4–9	170.14	KS29~	late Campanian~	P	R																																		
19R-CC, 14–16	186.66	Not defined	Coniacian	M	F																																		
20R-CC, 8–11	190.1	Not defined	Coniacian	G	F																																		
21R-CC, 18–20	196.02	Not defined	No age assignment	M	R																																		
22R-CC, 19–21	201.29	Not defined	No age assignment	G	F																																		
23R-2, 70–71	204.61	Not defined	No age assignment	P	F																																		
24R-4, 55–56	212.51	Not defined	Turonian?	M	R																																		
25R-1, 149–150	214.09	Not defined	No age assignment	P	R																																		
26R-CC, 18–20	219.94				B																																		
27R-CC, 20–23	226.92	Not defined	Albian?	P	R																																		

Table T7 (continued).

Core, section, interval (cm)	Depth (mbsf)	Zone	Age	Preservation	Abundance	*Catapsydrax dissimilis*	*Catapsydrax unicavus*	*Globigerina pseudovenezuelana*	*Globigerina yeguaensis*	*Globorotaloides suteri*	*Hantkenina alabamensis*	*Subbotina gortanii*	*Subbotina linaperta*	*Turborotalia increbescens*	*Turborotalia pseudoampliapertura*	*Chiloguembelina cubensis*	*Dentoglobigerina galavisi*	*Globigerina euapertura*	*Turborotalia ampliapertura*
207-1257B-																			
1R-1, 0–1	40	P18	early Oligocene	P	F	X	X			X						X	X	X	X
1R-2, 47–49	41.97	P16	late Eocene	G	A	X	X	X	X	X	X	X	X	X	X				
1R-3, 74–77	43.74	P14	middle Eocene	G	A														
2R-CC, 14–19	49.35	P14	middle Eocene	M	F														
3R-CC, 21–26	55.38	P11	middle Eocene	M	C														
4R-CC, 16–21	66.32	P6	early Eocene	P	C														
5R-CC, 12–17	73.9	P6	early Eocene		B														
6R-CC, 10–15	80.07	P5	early Eocene	P	C														
7R-1, 29–31	88.59	P5	late Paleocene	P	C														
7R-CC, 21–26	91.51	P4	late Paleocene	G	C														
8R-CC, 21–26	106.54	P4	late Paleocene	M	C														
9R-CC, 30–35	117.51	P4	late Paleocene	G	C														
10R-CC, 10–15	127.09	P4	late Paleocene	G	C														
11R-CC, 5–10	135.94	P4	late Paleocene	G	C														
12R-CC, 17–22	145.98	KS30	early Maastrichtian–late Campanian	P	F														
13R-CC, 0–6	154.43	KS29~	late Campanian~	M	C														
14R-1, 111–116	156.61	KS29~	late Campanian~	P	F														
15R-1, 0–2	165.1	KS29~	late Campanian~	P	C														
16R-CC, 4–9	170.14	KS29~	late Campanian~	P	R														
19R-CC, 14–16	186.66	Not defined	Coniacian	M	F														
20R-CC, 8–11	190.1	Not defined	Coniacian	G	F														
21R-CC, 18–20	196.02	Not defined	No age assignment	M	R														
22R-CC, 19–21	201.29	Not defined	No age assignment	G	F														
23R-2, 70–71	204.61	Not defined	No age assignment	P	F														
24R-4, 55–56	212.51	Not defined	Turonian?	M	R														
25R-1, 149–150	214.09	Not defined	No age assignment	P	R														
26R-CC, 18–20	219.94				B														
27R-CC, 20–23	226.92	Not defined	Albian?	P	R														

Table T8. Distribution of planktonic foraminifers, Hole 1257C. (Continued on next page.)

Core, section, interval (cm)	Depth	Zone	Age	Preservation	Group abundance	*Costellagerina pilula*	*Hedbergella delrioensis*	*Heterohelix reussi*	*Whiteinella archaeocretacea*	*Heterohelix moremani*	*Hastigerinoides subdigitata*	*Hedbergella simplex*	*Heterohelix globulosa*	*Contusotruncana fornicata*	*Globigerinelloides prairiehillensis*	*Globotruncana aegyptiaca*	*Globotruncana arca*	*Heterohelix punctulata*	*Pseudoguembelina costulata*	*Rugoglobigerina macrocephala*	*Rugotruncana subcircumnodifer*	*Globotruncanella havanensis*	*Globotruncanella petaloidea*	*Globotruncanita stuarti*	*Rugoglobigerina rugosa*	*Globanomalina pseudomenardii*	*Morozovella acuta*	*Morozovella aequa*	*Morozovella apanthesma*	*Morozovella velascoensis*	*Subbotina triangularis*	*Subbotina triloculinoides*	*Subbotina velascoensis*	*Acarinina nitida*	*Acarinina soldadoensis*
207-1257C-																																		
1R-1, 145–150	83.50	P6	early Eocene	G	C																									X				
1R-3, 123–125	86.23	P6	early Eocene	G	C																						X					X		X
1R-CC, 14–19	88.28	P6	early Eocene	G	C																					X	X			X		X		X
2R-CC, 8–13	92.83	P5	late Paleocene	G	C																					X	X		X	X	X	X		X
3R-CC, 19–24	110.60	P5	late Paleocene	G	A																					X	X		X	X	X	X	X	X
4R-CC, 15–20	120.65	P4	late Paleocene	G	A																					X	X		X	X	X	X	X	X
5R-CC, 8–13	126.97	P4	late Paleocene	G	C																					X	X		X	X	X	X	X	X
6R-7, 59–64	139.69	P4	late Paleocene	G	A																					X	X	X	X	X	X	X	X	
7R-CC, 19–24	148.98	KS30	early Maastrichtian~late Campanian	M	C											X	X				X	X	X	X	X									
8R-CC, 16–21	158.48	KS30	early Maastrichtian~late Campanian	M	C									X	X	X	X	X	X	X	X													
9R-CC, 14–19	166.39	Not defined	No age assignment	P	R								X																					
10R-CC, 16–21	171.17	Not defined	No age assignment		B																													
12R-CC, 20–26	190.40	Not defined	No age assignment	P	R		X	X			X	X	X																					
13R-CC, 20–21	201.30	Not defined	No age assignment	P	R					X																								
14R-CC, 0–4	210.03	Not defined	Santonian?	P	C	X	X	X	X																									
15R-CC, 34–39	220.02				B																													
16R-CC, 12–18	234.72																																	

Note: Preservation: G = good, M = moderate, P = poor. Abundance: A = abundant, C = common, R = rare, B = barren.

Table T8 (continued).

Core, section, interval (cm)	Depth	Zone	Age	Preservation	Group abundance	*Acarinina mckannai*	*Morozovella occlusa*	*Chiloguembelina wilcoxensis*	*Igorina albeari*	*Morozovella subbotinae*	*Acarinina coalingensis*	*Acarinina quetra*	*Chiloguembelina crinita*	*Morozovella gracilis*	*Acarinina wilcoxensis*
207-1257C-															
1R-1, 145–150	83.50	P6	early Eocene	G	C					X					X
1R-3, 123–125	86.23	P6	early Eocene	G	C			X		X	X	X	X	X	
1R-CC, 14–19	88.28	P6	early Eocene	G	C		X		X	X					
2R-CC, 8–13	92.83	P5	late Paleocene	G	C		X	X							
3R-CC, 19–24	110.60	P5	late Paleocene	G	A	X	X								
4R-CC, 15–20	120.65	P4	late Paleocene	G	A	X									
5R-CC, 8–13	126.97	P4	late Paleocene	G	C										
6R-7, 59–64	139.69	P4	late Paleocene	G	A										
7R-CC, 19–24	148.98	KS30	early Maastrichtian~late Campanian	M	C										
8R-CC, 16–21	158.48	KS30	early Maastrichtian~late Campanian	M	C										
9R-CC, 14–19	166.39	Not defined	No age assignment	P	R										
10R-CC, 16–21	171.17	Not defined	No age assignment		B										
12R-CC, 20–26	190.40	Not defined	No age assignment	P	R										
13R-CC, 20–21	201.30	Not defined	No age assignment	P	R										
14R-CC, 0–4	210.03	Not defined	Santonian?	P	C										
15R-CC, 34–39	220.02				B										
16R-CC, 12–18	234.72														

Table T9. Shipboard cryogenic magnetometer analyses, Site 1257.

Section, cores	Approximate age range	Demagnetization
207-1257A-		
1H–4H	Miocene–lower Oligocene	NRM; 10, 15, and 20 mT
5H, 6X–20X	Oligocene–Santonian	NRM; 10 and 15 mT
26X–31X	Albian	NRM; 10 and 15 mT
207-1257B-		
1R–14R	Eocene–Campanian	NRM; 10, 15, and 20 mT
17R–27R	Santonian–Albian	NRM; 10, 15, and 20 mT
207-1257C-		
1R–10R	Eocene–Campanian	NRM; 10, 15, and 20 mT
15R and 16R	Cenomanian–Albian	NRM; 10, 15, and 20 mT

Note: NRM = natural remanent magnetization.

Table T10. Characteristic directions of minicores, Holes 1257A, 1257B, and 1257C. (See table notes. Continued on next two pages.)

Core, section, interval (cm)	PMAG code	Depth (mcd)	Polarity Label	Polarity Code	Chron/ subchron	Declination (°)	Inclination (°)	Intensity (mA/m)	MAD (°)	N	Temperature steps used in least square analysis (°C) 1	2	3	4	5	6	7	8	9
207-1257A-																			
18X-1, 118	181.118	157.28	N?	1	C32n	165.6	74.7	1.40E–02	4.5	7	200	240	270	300	330	360	400	Org	Tied
18X-3, 110	183.110	160.20	N?	1		215.2	62.0	4.04E–03	3.7	6	200	200	240	240	300	300	Org	Tied	
18X-5, 133	185.133	163.39	NPP	2		123.2	46.5	6.40E–03	3.9	4	240	240	270	270	Org	Tied			
18X-7, 24	187.024	165.30	N	4		129.5	23.4	1.41E–02	2.0	3	200	240	300	Org	Tied				
19X-1, 136	191.136	166.86	INT	0	C32r	190.0	–64.7	1.19E–02	4.9	4	300	330	360	400	Org	Tied			
20X-1, 26	201.026	175.46	N	4	C33n	339.0	37.0	5.13E–02	2.0	3	200	240	300	Org	Tied				
207-1257B-																			
1R-1, 29	11.029	41.66	NPP	2	C15n?	106.3	–8.1	6.80E–03	5.6	4	200	200	240	240	Org	Tied			
1R-2, 47	12.047	43.34	NP	3		266.6	0.5	8.67E–03	4.5	6	50	150	200	250	250	300	Org	Tied	
					Hiatus														
1R-3, 48	13.048	44.85	N	4	C17n?	241.2	4.6	1.43E–02	2.5	5	50	150	200	250	300	Org	Tied		
2R-1, 74	21.074	48.91	RP	–3	C17r?	121.7	–5.9	4.18E–03	3.9	4	200	200	240	240	Org	Tied			
2R-2, 71	22.071	50.38	NP	3	C18n	317.3	24.3	7.24E–03	4.7	5	250	250	300	300	350	Org	Tied		
2R-3, 87	23.087	52.04	NP	3		304.4	10.2	9.62E–03	3.9	4	300	330	360	360	Org	Tied			
3R-1, 72	31.072	53.89	NP	3		58.4	3.7	1.03E–02	3.7	2	150	200	Org	Tied					
3R-2, 133	32.133	56.00	N	4		357.6	11.6	1.10E–02	3.2	4	200	250	300	350	Org	Tied			
3R-3, 134	33.134	57.51	RP	–3	C18r?	331.8	–8.5	8.01E–03	5.9	4	300	300	330	330	Org	Tied			
3R-4, 36	34.036	57.99	RP	–3		225.9	4.4	9.64E–03	6.4	4	300	350	400	400	Org	Tied			
					Gap in coverage														
4R-1, 67	41.067	67.18	NP	3	C20n?	330.9	–13.9	2.55E–02	3.3	6	240	270	300	330	360	400	Org	Tied	
4R-2, 109	42.109	69.09	RP	–3	C20r?	254.6	–13.8	1.25E–02	6.5	6	200	250	300	350	400	400	Org	Tied	
4R-3, 39	43.039	69.89	RP	–3		241.6	–19.0	2.88E–02	3.7	5	200	250	300	350	400	Org	Tied		
					Hiatus														
4R-4, 84	44.084	71.84	RP	–3	C23r?	243.7	20.7	7.55E–01	3.4	6	270	300	330	360	400	450	Org	Tied	
4R-5, 14	45.014	72.64	N	4	C24n?	3.1	21.6	1.30E+00	2.2	6	250	300	350	400	400	450	Org	Tied	
5R-1, 106	51.106	73.11	RP	–3		246.7	13.4	2.55E–01	3.1	4	250	300	350	450	Org	Tied			
5R-3, 117	53.117	75.97	N	4		39.5	–11.1	1.37E–01	4.4	6	270	300	330	360	400	450	Org	Tied	
5R-4, 49	54.049	76.77	R?	–1		81.9	4.5	4.45E–02	3.4	7	150	200	250	300	350	400	450	Org	Tied
6R-1, 118	61.118	84.25	NP	3	C24n?	345.3	–0.3	3.31E–02	4.2	5	150	200	250	300	350	Org	Tied		
7R-1, 14	71.014	92.81	N	4		8.3	–2.0	2.65E–02	2.9	7	150	200	240	270	300	330	360	Org	Tied
7R-2, 17	72.017	94.34	N	4		333.9	–13.0	2.40E–02	1.7	3	250	300	350	Org	Tied				
8R-1, 4	81.004	101.37	R	–4	C24r?	258.9	–11.6	1.84E–02	4.5	5	150	200	250	300	350	Org	Tied		
8R-2, 2	82.002	102.85	RP	–3		275.5	–16.9	1.58E–02	6.3	9	150	200	240	270	300	330	360	400	400
8R-3, 2	83.002	104.32	N	4	C25n	332.2	1.4	2.81E–02	3.8	5	150	200	250	300	350	Org	Tied		
8R-3, 63	83.063	104.93	INT	0		310.2	–9.8	1.70E–02	3.1	3	200	250	300	Org	Tied				
8R-3, 144	83.144	105.74	N?	1		304.9	–0.1	8.27E–03	2.9	3	250	300	300	Org	Tied				
8R-4, 49	84.049	106.29	NP	3		358.6	11.0	4.45E–02	1.3	3	200	250	300	Org	Tied				
8R-4, 84	84.084	106.64	N	4		2.4	24.1	2.25E–02	3.0	4	50	200	250	300	Org	Tied			
8R-4, 138	84.138	107.18	N	4		358.1	30.0	3.85E–02	3.7	4	150	200	250	300	Org	Tied			
8R-5, 28	85.028	107.58	NP	3		323.0	23.1	6.11E–02	4.2	6	50	150	200	250	300	350	Org	Tied	
8R-5, 91	85.091	108.21	NP	3		39.4	0.3	2.72E–02	6.2	6	200	240	270	300	330	360	Org	Tied	
8R-5, 135	85.135	108.66	N	4		43.0	12.9	6.36E–02	3.0	5	200	250	300	350	400	Org	Tied		
8R-6, 25	86.025	109.05	N	4		13.7	27.7	3.39E–02	4.6	5	250	300	350	400	450	Org	Tied		
8R-6, 75	86.075	109.55	N	4		18.3	21.0	3.83E–02	2.9	4	250	300	350	400	Org	Tied			
8R-CC, 17	89.017	109.93	N?	1		320.8	16.2	5.70E–02	4.7	4	200	250	300	350	Org	Tied			
9R-1, 42	91.042	109.79	NP	3		65.1	26.5	4.12E–02	5.3	3	150	200	250	Org	Tied				
9R-1, 80	91.080	110.17	NP	3	C25n	54.8	12.8	4.67E–02	18.2	4	330	360	400	450					

Table T10 (continued).

Core, section, interval (cm)	PMAG code	Depth (mcd)	Polarity Label	Polarity Code	Chron/ subchron	Declination (°)	Inclination (°)	Intensity (mA/m)	MAD (°)	N	Temperature steps used in least square analysis (°C) 1	2	3	4	5	6	7	8	9
9R-2, 47	92.047	111.34	N	4		346.6	15.9	8.25E–02	3.0	9	50	150	200	240	270	300	330	360	400
9R-3, 54	93.054	112.93	NP	3		271.8	31.2	2.57E–02	2.9	3	200	250	300	Org	Tied				
9R-3, 99	93.099	113.38	INT	0		269.6	53.6	3.34E–02	4.6	5	150	200	250	300	350	Org	Tied		
9R-3, 137	93.137	113.76	INT	0		283.1	72.2	6.61E–03	1.4	2	350	350	Org	Tied					
9R-4, 14	94.014	114.03	NP	3		349.5	12.3	1.95E–02	9.8	2	250	300	Org	Tied					
9R-4, 74	94.074	114.63	NP	3		345.4	14.1	1.90E–02	7.1	3	200	250	300	Org	Tied				
9R-4, 118	94.118	115.07	NPP	2		43.9	34.9	4.39E–03	0.8	2	350	350	Org	Tied					
9R-5, 2	95.002	115.41	RPP	–2	C25r	31.4	–6.8	2.56E–02	0.0	1	350	Org	Tied						
9R-5, 68	95.068	116.07	R?	–1		336.5	4.0	7.92E–02	2.2	4	200	250	300	350	Org	Tied			
9R-5, 133	95.133	116.72	RPP	–2		112.9	5.5	8.64E–03	2.5	1	300	Org	Tied						
9R-6, 37	96.037	117.26	RP	–3		238.5	–4.9	2.72E–02	9.8	4	270	300	330	360	Org	Tied			
9R-7, 6	97.006	118.45	RPP	–2		33.5	–1.7	6.03E–03	5.8	3	350	400	400	Org	Tied				
10R-1, 69	101.069	120.47	NPP	2		292.4	25.1	2.27E–02	4.9	5	150	200	250	300	350	Org	Tied		
10R-2, 75	102.075	122.03	RPP	–2	C25r?	207.4	–19.8	1.17E–02	14.6	5	300	330	360	400	400	Org	Tied		
10R-3, 21	103.021	122.99	RPP	–2		145.8	8.6	1.70E–02	0.9	3	250	300	350	Org	Tied				
10R-4, 17	104.017	124.45	NP	3		274.8	6.6	1.32E–02	6.0	3	350	400	400	Org	Tied				
10R-5, 3	105.003	125.81	RPP	–2		275.8	–10.0	1.68E–02	0.0	2	400	Org	Tied						
10R-6, 4	106.004	127.32	NP	3	C26n	338.2	24.5	2.58E–02	1.7	2	350	400	Org	Tied					
10R-7, 61	107.061	129.39	NP	3		16.9	3.2	1.41E–02	6.3	3	330	360	400	Org	Tied				
11R-1, 29	111.029	129.67	N	4		97.1	–4.8	5.25E–02	3.1	6	200	250	300	350	400	450	Org	Tied	
11R-2, 27	112.027	131.15	N	4		242.2	10.1	9.35E–02	3.1	5	270	300	330	360	400	Org	Tied		
11R-3, 30	113.030	132.68	N	4		201.6	11.1	1.05E–01	2.4	5	250	300	350	400	450	Org	Tied		
11R-4, 33	114.033	134.19	NP	3		178.2	22.8	3.59E–02	7.2	3	300	350	400	Org	Tied				
11R-5, 84	115.084	136.22	INT	0		273.4	41.3	2.60E–02	6.5	6	200	250	300	350	400	450	Org	Tied	
11R-7, 1	117.001	137.89	N	4		283.6	–9.8	3.86E–02	3.2	9	150	200	240	270	300	330	360	400	400
					Hiatus														
12R-1, 40	121.040	139.27	R?	–1	C31r	62.6	44.4	2.74E–03	5.8	2	200	200	Org	Tied					
12R-2, 58	122.058	140.95	RP	–3		193.3	–3.1	8.34E–03	1.6	3	250	300	300	Org	Tied				
12R-3, 26	123.026	142.13	R	–4		163.8	10.2	4.22E–02	6.7	6	240	270	300	330	360	400	Org	Tied	
12R-4, 54	124.054	143.91	RPP	–2		166.9	21.3	4.00E–03	1.1	2	200	200	Org	Tied					
12R-6, 56	126.056	146.94	RPP	–2		263.3	0.0	1.19E–02	14.5	4	250	300	350	350	Org	Tied			
12R-7, 2	127.002	147.90	N?	1		46.4	5.1	4.99E–03	5.0	4	250	250	300	300	Org	Tied			
12R-CC, 1	129.001	148.49	RPP	–2		16.3	27.2	6.49E–03	3.4	4	300	300	350	350	Org	Tied			
13R-1, 26	131.026	149.26	N?	1		346.1	–2.4	4.45E–03	0.9	2	150	150	Org	Tied					
13R-2, 28	132.028	150.78	RPP	–2		331.3	28.6	6.63E–03	4.2	3	200	250	250	Org	Tied				
13R-3, 28	133.028	152.28	INT	0		30.4	36.2	2.87E–03	0.0	1	AF50	Org	Tied						
13R-4, 25	134.025	153.75	INT	0		91.3	62.5	3.79E–03	0.0	1	AF50	Org	Tied						
13R-5, 87	135.087	155.87	R?	–1		5.4	21.7	4.09E–03	8.4	4	200	200	240	240	Org	Tied			
13R-6, 52	136.052	157.02	NPP	2	C32n	2.3	46.8	3.79E–03	2.8	5	150	200	200	240	240	Org	Tied		
14R-1, 21	141.021	158.91	R?	–1		65.2	16.8	5.78E–03	1.0	2	50	50	Org	Tied					
17R-1, 12	171.012	177.72	N	4	C33n	134.1	8.3	3.79E–01	1.0	4	150	200	240	300	Org	Tied			
27R-2, 17	272.017	227.61	NP	1	C34n	102.3	15.7	2.34E–01	0.0	1	300	Org	Tied						
207-1257C-																			
7R-5, 130	75.130	148.76	RP	–3	C31r	139.3	26.2	4.52E–03	6.2	4	250	250	300	300	Org	Tied			
9R-1, 80	91.080	161.91	NP	3	C32n	52.2	19.5	8.93E–02	3.8	7	150	200	240	270	300	330	360	Org	Tied
9R-3, 84	93.084	164.95	NP	3		35.4	36.6	1.51E–02	3.0	5	200	240	240	300	300	Org	Tied		

Table T10 (continued).

Core, section, interval (cm)	PMAG code	Depth (mcd)	Polarity		Chron/ subchron	Declination (°)	Inclination (°)	Intensity (mA/m)	MAD (°)	*N*	Temperature steps used in least square analysis (°C)								
			Label	Code							1	2	3	4	5	6	7	8	9
9R-5, 41	95.041	167.46	RP	–3	C32r	237.8	1.0	5.61E–02	5.3	4	150	200	240	300	Org	Tied			
9R-6, 59	96.059	168.64	RP	–3		332.8	2.9	2.28E–02	5.0	3	330	360	400	Org	Tied				

Notes: PMAG = paleomagnetism, MAD = maximum angular deviation. Black = normal polarity, white = reversed polarity, gray = intermediate or questionable polarity, yellow = gap in coverage or hiatus. Examples of interpretation of progressive demagnetization plots and methods of computation of the characteristic directions are given in **"Paleomagnetism,"** p. 16, in the "Explanatory Notes" chapter.

Table T11. Composite depths, Site 1257.

Core	Depth (mbsf)	Offset (m)	Depth (mcd)	Depth shifted
207-1257A-				
1H	0.0	0.00	0.00	N
2H	2.6	0.00	2.60	N
3H	12.1	0.00	12.10	N
4H	21.6	0.00	21.60	N
5H	31.1	0.00	31.10	N
6X	40.6	0.00	40.60	N
7X	44.9	0.00	44.90	N
8X	54.1	0.00	54.10	N
9X	63.7	0.00	63.70	N
10X	73.3	0.00	73.30	N
11X	83.0	0.00	83.00	N
12X	92.6	0.00	92.60	N
13X	102.2	0.00	102.20	N
14X	111.8	0.00	111.80	N
15X	121.5	–0.41	121.09	Y
16X	131.1	3.63	134.73	Y
17X	140.7	5.47	146.17	Y
18X	150.3	5.80	156.10	Y
19X	159.7	5.80	165.50	N
20X	169.4	5.80	175.20	N
21X	179.0	5.80	184.80	N
22X	188.6	5.80	194.40	N
23X	198.2	5.80	204.00	N
24X	207.6	5.80	213.40	N
25X	217.2	5.80	223.00	N
26X	226.8	5.80	232.60	N
27X	236.5	5.80	242.30	N
28X	246.2	5.80	252.00	N
29X	255.8	5.80	261.60	N
30X	265.4	5.80	271.20	N
31X	275.1	5.80	280.90	N
207-1257B-				
1R	40.0	1.37	41.37	Y
2R	44.8	3.37	48.17	Y
3R	49.8	3.37	53.17	N
4R	59.4	7.11	66.51	Y
5R	69.0	3.05	72.05	Y
6R	78.7	4.37	83.07	Y
7R	88.3	4.37	92.67	N
8R	97.9	3.43	101.33	Y
9R	107.6	1.77	109.37	Y
10R	117.2	2.58	119.78	Y
11R	126.8	2.58	129.38	N
12R	136.2	2.67	138.87	Y
13R	145.8	3.20	149.00	Y
14R	155.5	3.20	158.70	N
19R	183.7	3.20	186.90	N
20R	188.7	6.13	194.83	Y
21R	193.3	6.13	199.43	N
22R	198.3	6.13	204.43	Y
23R	203.0	6.13	209.13	N
24R	208.0	5.44	213.44	Y
25R	212.6	5.44	218.04	N
26R	217.6	3.64	221.24	Y
27R	222.3	3.64	225.94	N
207-1257C-				
1R	82.0	0.00	82.00	N
2R	91.6	0.00	91.60	N
3R	101.2	2.00	103.20	Y
4R	110.8	2.40	113.20	Y
5R	120.5	2.67	123.17	Y
6R	130.1	1.20	131.30	Y
7R	139.5	2.45	141.95	Y
8R	149.1	2.45	151.55	N
9R	158.7	2.41	161.11	Y
10R	168.4	2.41	170.81	N
11R	178.0	2.55	180.55	Y
12R	187.7	2.55	190.25	N
13R	197.3	2.55	199.85	N
14R	207.0	2.55	209.55	N
15R	216.6	2.55	219.15	N
16R	226.2	1.16	227.36	Y

Note: N = no, Y = yes.

Table T12. Splice tie points, Holes 1257B and 1257C.

Hole, core, section, interval (cm)	Depth (mbsf)	Depth (mcd)		Hole, core, section, interval (cm)	Depth (mbsf)	Depth (mcd)
207-				207-		
1257B-8R-4, 135	103.72	107.15	Tie to	1257C-3R-3, 95	105.15	107.15
1257C-3R-6, 90	109.60	111.60	Tie to	1257B-9R-2, 72.5	109.83	111.60
1257B-9R-5, 60	114.22	115.99	Tie to	1257C-4R-2, 128.5	113.59	115.99
1257C-4R-6, 12.5	118.43	120.83	Tie to	1257B-10R-1, 105	118.25	120.83
1257B-10R-7, 72.5	126.93	129.51	Append to	1257B-11R-1, 0	126.80	129.38
1257B-11R-5, 92.5	133.73	136.31	Tie to	1257C-6R-4, 49.5	135.11	136.31
1257C-6R-6, 80	138.40	139.60	Tie to	1257B-12R-1, 72.5	136.93	139.60
1257B-12R-5, 7.5	142.28	144.95	Tie to	1257C-7R-2, 150	142.50	144.95
1257C-7R-7, 72.5	148.73	151.18				

Table T13. Calcareous nannofossil and planktonic foraminifer datums used in the preliminary age-depth model, Hole 1257A. (See table note. Continued on next page.)

Core, section, interval (cm)	Depth (mbsf)		Age (Ma)		Foraminifer zone	Nannofossil zone	Epoch
	Top	Base	Minimum	Maximum			
207-1257A-							
1H-1, 26	0.26		4.56	8.28		NN11	late Miocene
1H-1, 50–55	0.5	0.55	5.54	8.58	M14–M13b, reworked Miocene		Pliocene
1H-2, 4.5	1.54		5.54	8.28		NN11	late Miocene
1H-CC, 25–30	2.54	2.59	28.1	30.4		NP23	early Oligocene
1H-CC, 25–30	2.54	2.59	30.3	32	P19		late Oligocene
2H-1, 24	2.84		28.1	30.4		NP23	early Oligocene
2H-7, 23	11.83		28.1	30.4		NP23	early Oligocene
2H-CC, 24–29	12.44	12.49	31.7	32.9		NP22	early Oligocene
2H-CC, 24–29	12.44	12.49			P19		late Oligocene
3H-1, 50–54	12.6	21.64	30.3	32	P19		late Oligocene
3H-2, 50–54	14.1	14.14	32	33.8	P18		early Oligocene
3H-3, 50–54	15.6	15.64			P18		early Oligocene
3H-4, 50–54	17.1	17.15			P18		early Oligocene
3H-5, 50–54	18.6	18.65			P18		early Oligocene
3H-6, 50–54	20.1	20.14			P18		early Oligocene
3H-7, 25	21.35		31.7	32.9		NP22	early Oligocene
3H-7, 50–54	21.6	21.64			P18		early Oligocene
3H-CC, 35–39	22.08	22.12	32.9	34		NP21	earliest Oligocene
3H-CC, 35–39	22.08	22.12			P18		early Oligocene
4H-CC, 23–27	31.56	31.6	32.2	33.7		NP21	earliest Oligocene
4H-CC, 23–27	31.56	31.6			P18		early Oligocene
5H-CC, 46–51	40.95	41	32.9	34		NP21	earliest Oligocene
5H-CC, 46–51	40.95	41			P18		early Oligocene
6X-1, 46–48	41.06	41.08			P18		early Oligocene
6X-2, 50–52	42.6	42.62	32	33.8	P18		early Oligocene
6X-2, 65	42.75		32.9	34		NP21	earliest Oligocene
6X-2, 104	43.14		34.9	38.5		NP20	late Eocene
6X-3, 24	43.84		37.1	38.5		NP17	middle Eocene
6X-3, 50–52	44.1	44.12	38.4	40.1	P14		middle Eocene
7X-1, 52–54	45.42	45.44			P14		middle Eocene
6X-4, 46–48	45.56	45.58			P14		middle Eocene
6X-CC, 21–26	46.76	46.81	37.1	38.5		NP17	middle Eocene
6X-CC, 21–26	46.76	46.81			P14		middle Eocene
7X-2, 51–54	46.91	46.94			P14–P13		middle Eocene
7X-3, 49–52	48.39	48.42	38.4	40.1	P14		middle Eocene
7X-4, 47–51	49.87	49.91	40.1	40.5	P13		middle Eocene
7X-5, 51–55	51.41	51.45			P13		middle Eocene
7X-CC, 20–25	52.56	52.61	40.4	42.5		NP16	middle Eocene
8X-1, 46–49	54.56	54.59			P13		middle Eocene
8X-2, 47–48	56.07	56.08	40.1	40.5	P13		middle Eocene
8X-3, 51–53	57.61	57.63	40.5	43.6	P12		middle Eocene
8X-4, 49–52	59.09	59.12			P12		middle Eocene
8X-5, 50–53	60.6	60.63	40.5	43.6	P12		middle Eocene
8X-CC, 31–36	61.92	61.97	40.4	42.5		NP16	middle Eocene
9X-4, 50–54	68.7	68.74	43.6	45.8	P11		middle Eocene
9X-4, 95	69.15		40.4	42.5		NP16	middle Eocene
9X-5, 25	69.45		40.4	42.5		NP16	middle Eocene
9X-5, 50–54	69.7	69.74	45.8	49	P10		middle Eocene
9X-CC, 43–48	70.38	70.43	53	53.3		NP11	early Eocene
9X-CC, 43–48	70.38	70.43	52.3	54.7	P6		early Eocene
10X-1, 50–54	73.8	73.84	52.3	54	P6B		early Eocene
10X-2, 50–54	75.3	75.34			P6		early Eocene
10X-3, 26–30	76.56	76.6			P6		early Eocene
10X-4, 48–53	78.28	78.33			P6		early Eocene
10X-5, 40–45	79.7	79.75			P6		early Eocene
10X-6, 40–46	80.7	80.76			P6		early Eocene
10X-CC, 46–51	81.51	81.56	53	53.3		NP11	early Eocene
10X-CC, 46–51	81.51	81.56			P6		early Eocene
11X-1, 49–54	83.49	83.54	52.3	54.7	P6		early Eocene
11X-2, 27–32	84.61	84.66			P4 and P6		early Eocene
11X-2, 40	84.74		53	54.1		NP9/NP10	early Eocene
12X-1, 50–51	93.1	93.11	54.7	55.9	P5		late Paleocene
12X-2, 50–54	94.6	94.64	55.9	59.2	P4		late Paleocene
12X-3, 50–54	96.1	96.14			P4		late Paleocene
12X-CC, 47–52	98.32	98.37	53	54.1		NP9/NP10	early Eocene
12X-CC, 47–52	98.32	98.37			P4		late Paleocene

Table T13 (continued).

Core, section, interval (cm)	Depth (mbsf)		Age (Ma)		Foraminifer zone	Nannofossil zone	Epoch
	Top	Base	Minimum	Maximum			
13X-CC, 31–36	111.81	111.86	56.2	56.5		NP8	late Paleocene
13X-CC, 31–36	111.81	111.86			P4		late Paleocene
14X-CC, 12–17	120.83	120.88	57.3	57.5		NP7	late Paleocene
14X-CC, 12–17	120.83	120.88			P4		late Paleocene
15X-1, 51–54	122.01	122.04			P4		late Paleocene
15X-4, 47–52	126.47	126.52			P4		late Paleocene
15X-6, 47–51	129.47	129.51			P4		late Paleocene
15X-CC, 39–44	131.32	131.37	57.3	57.5		NP7	late Paleocene
15X-CC, 39–44	131.32	131.37			P4		late Paleocene
16X-1, 50–52	131.6	131.62			P4		late Paleocene
16X-3, 48–51	134.58	134.61			P4		late Paleocene
16X-4, 49–52	136.09	136.12			P4		late Paleocene
16X-5, 40–43	137.5	137.53	57.1	59.2	lower P4		late Paleocene
16X-CC, 58–63	138.37	138.42	58.2	59.3		NP5	late Paleocene
17X-1, 25	140.95		69.2	71.3		CC23	middle Maastrichtian
17X-1, 50–54	141.2	141.24					early Maastrichtian
17X-3, 50–54	144.16	144.2	68.6	72.8	KS30		late Campanian–early Maastrichtian
17X-4, 48–50	145.64	145.66	68.6	72.8	KS30		late Campanian–early Maastrichtian
17X-6, 25	148.11		69.2	71.3		CC23	middle Maastrichtian
17X-CC, 59–64	149.08	149.13	69.2	71.3		CC23	middle Maastrichtian
18X-CC, 27–32	159.98	160.03	69.2	71.3		CC23	middle Maastrichtian
18X-CC, 27–32	159.98	160.03	68.6	73.8	KS29-KS30		late Campanian–early Maastrichtian
20X-1, 26	169.66		75.3	76		CC22	middle Campanian
20X-2, 102	171.92		75.3	76		CC22	middle Campanian
20X-5, 0	175.4		80.6	84.8		CC18–CC16	early Campanian–late Santonian
21X-1, 0	179		84.7	88.8		CC16/CC17	Santonian
21X-CC, 0–5	179.9	179.95	83.5	85.8			Santonian
22X-CC, 15–20	190.88	190.93	84.7	88.8		CC16/CC17	Santonian
22X-CC, 15–20	190.88	190.93	83.5	89			Coniacian–Santonian
23X-CC, 19–24	206.67	206.72	84.7	88.8		CC16/CC17	Santonian
23X-CC, 19–24	206.67	206.72	85.8	89			Coniacian
24X-CC, 22–28	212.22	212.28	91				Turonian
24X-CC, 22–28	212.22	212.28	89	93.5			Turonian
25X-CC, 43–46	219.33	219.36	93.5				late Cenomanian
27X-4, 143	242.43		101.7	107.3		CC8	Albian
27X-CC, 46–51	244.08	244.13	99.1				late Albian
29X-CC, 0	265.25		101.7	107.3		CC8	Albian
30X-CC, 0	274.94		101.7	107.3		CC8	Albian
31X-CC, 0	275.91		107.3	112.5		CC8	Albian

Note: Both minimal and maximal assigned ages (Ma) are given for each sample analyzed.

Table T14. Magnetostratigraphic datums used in the preliminary age-depth model, Hole 1257A.

Core	Depth (mbsf)	Age (Ma)	Polarity chron/subchron	Epoch, stage
207-1257A-				
6X	45	40.13	C18n.2n (bottom)	Eocene, Bartonian
8X	56.5	41.257	C19n (top)	Eocene, Lutetian
8X	58.2	41.521	C19n (bottom)	Eocene, Lutetian
8X	63.7	42.536	C20n (top)	Eocene, Lutetian
9X	66.2	43.789	C20n (bottom)	Eocene, Lutetian
9X	67.6	52.663	C24n.1n (bottom)	Eocene, Ypresian
9X	71.9	53.347	C24n.3n (bottom)	Eocene, Ypresian
12X	96.3	55.904	C25n (top)	Paleocene, Thanetian
13X	103.8	56.391	C25n (bottom)	Paleocene, Thanetian
15X	129.5	57.554	C26n (top)	Paleocene, Thanetian
16X	137.4	57.911	C26n (bottom)	Paleocene, Thanetian
17X	141	71.338	C32n.1n (bottom)	Maastrichtian
17X	143	71.587	C32n.2n (top)	Campanian
18X	152	73.004	C32n.2n (bottom)	Campanian
18X	156	73.291	C32r.1n (top)	Campanian
18X	157	73.374	C32r.1n (bottom)	Campanian

Table T15. Linear sedimentation rates and mass accumulation rates, Hole 1257A.

Epoch	Core, section, interval (cm)	Top		Bottom		Thickness (m)	Duration (m.y.)	LSR		DBD (g/cm^3)	MAR (g/cm^2 k.y.)	Main lithology
		Depth (mbsf)	Age (Ma)	Depth (mbsf)	Age (Ma)			(m/m.y.)	(cm/k.y.)			
	207-1257A-											
Neogene	1H-1, 0, to 1H-2, 45	0	—	1.95	7	1.95	—	—	—	—	—	Nannofossil ooze
Oligocene	1H-CC, 25, to 6X-2, 104	2.54	29	43.14	37	40.60	8	5	0.5	0.95	0.5	Nannofossil chalk
middle Eocene	6X-3, 24, to 9X-5, 50	43.84	38	69.70	47	25.86	9	3	0.3	0.92	0.3	Nannofossil chalk
early Eocene–late Paleocene	9X-CC, 43, to 16X-CC, 58	70.38	53	138.37	59	67.99	6	11	1.1	1.17	1.3	Nannofossil chalk
Maastrichtian–Campanian	17X-1, 25, to 20X-2, 102	140.95	70	171.92	76	30.97	6	5	0.5	1.25	0.6	Nannofossil chalk
Santonian–Cenomanian	20X-5, 0, to 25X-CC, 43	175.40	83	219.33	94	43.93	11	4	0.4	1.60	0.6	Claystone (black shale)
Albian	27X-4, 143, to 31X-CC, 0	242.43	105	275.91	110	33.48	5	—	—	1.81	—	Carbonate siltstone

Notes: Averaged dry bulk densities (DBD) of major lithologies per studied interval were used (see **"Physical Properties,"** p. 27) to calculate mass accumulation rates (MAR) values. LSR = linear sedimentation rate. — = not assigned.

Table T16. Total carbon, inorganic carbon, carbonate, total organic carbon, and total nitrogen concentrations and carbon/nitrogen ratios, Site 1257. (See table notes. Continued on next two pages.)

Hole, core, section, interval (cm)	Depth (mbsf)	TC (wt%)	IC (wt%)	$CaCO_3$ (wt%)	TOC (wt%)	N (wt%)	C/N (atomic)
207-							
Unit I (nannofossil ooze):							
1257A-1H-1,42–43	0.42		1.47	12.2			
Unit II (foraminifer- and silica-bearing nannofossil chalk):							
1257A-1H-2, 48–49	1.98	10.00	9.90	82.5	0.10	0.02	5.8
1257A-2H-1, 45–46	3.05		9.05	75.4			
1257A-2H-3, 45–46	6.05	8.75	8.76	73.0		0.09	
1257A-2H-5, 45–46	9.05		7.04	58.6			
1257A-3H-1, 60–61	12.70		7.78	64.8			
1257A-3H-3, 58–59	15.68	8.57	8.54	71.1	0.03	0.03	1.3
1257A-3H-5, 60–61	18.70		7.96	66.3			
1257A-4H-1, 90–91	22.50		8.58	71.5			
1257A-4H-2, 17–18	23.27	9.72	9.71	80.9	0.01	0.02	0.6
1257A-4H-6, 80–81	29.70		7.18	59.8			
1257A-5H-1, 35–36	31.45		7.81	65.1			
1257A-5H-3, 35–36	34.45	7.36	7.25	60.4	0.11	0.03	4.8
1257A-5H-5, 35–36	37.45		6.69	55.7			
1257B-1R-1, 76–78	40.76		7.50	62.5			
1257A-6X-1, 19–20	40.79		8.04	67.0			
1257B-1R-2, 35–36	41.85	8.73	8.60	71.6	0.13		
1257B-1R-3, 74–75	43.74		9.12	76.0			
1257A-6X-3, 19–20	43.79	9.02	9.00	75.0	0.02	0.03	0.8
1257B-2R-1, 30–31	45.10		8.71	72.5			
1257A-7X-1, 79–80	45.69		9.33	77.7			
1257B-2R-2, 27–28	46.57	8.71	8.70	72.4	0.01		
1257A-6X-CC, 18–19	46.73		8.45	70.4			
1257A-7X-2, 108–109	47.48		8.31	69.2			
1257B-2R-3, 129–130	49.09		8.51	70.9			
1257B-3R-2, 51–52	51.81	9.15	9.05	75.4	0.10		
1257A-7X-5, 142–143	52.32	9.31	9.29	77.4	0.02	0.03	0.9
1257A-8X-1, 112–113	55.22		8.27	68.9			
1257A-8X-3, 92–93	58.02	8.07	8.01	66.7	0.06	0.03	2.7
1257B-4R-1, 93–94	60.33		8.24	68.7			
1257A-8X-5, 62–63	60.72		5.43	45.2			
1257B-4R-3, 57–58	62.96		8.95	74.6			
1257B-4R-4, 102–107	64.91	6.30	6.27	52.2	0.03		
1257B-4R-5, 33–34	65.72		5.93	49.4			
1257A-9X-4, 69–70	68.89	9.83	9.81	81.7	0.02	0.01	2.6
1257B-5R-1, 42–43	69.42		7.58	63.2			
1257B-5R-1, 132–133	70.32	5.87	5.69	47.4	0.18		
1257A-10X-2, 73–74	75.53		4.38	36.5			
1257A-10X-4, 30–31	78.10	7.44	7.43	61.9	0.01	0.03	1.3
1257B-6R-1, 90–91	79.60	6.89	6.74	56.2	0.15		
1257A-10X-6, 30–31	80.60		7.80	65.0			
Unit III (foraminifer-bearing nannofossil chalk):							
1257A-11X-1, 40–41	83.40		7.41	61.7			
1257A-11X-CC, 27–28	85.01	5.17	5.14	42.8	0.03	0.03	1.4
1257B-7R-2, 80–81	90.60	7.10	7.01	58.4	0.09	0.04	2.5
1257C-2R-1, 32–32	91.92		2.83	23.6			
1257C-2R-1, 103–103	92.63		7.32	61.0			
1257A-12X-1, 40–41	93.00		7.33	61.1			
1257A-12X-3, 40–41	96.00	7.10	7.06	58.8	0.04	0.02	2.0
1257B-8R-1, 60–61	98.50		7.52	62.7			
1257B-8R-3, 60–61	101.47	6.11	6.00	50.0	0.11		
1257A-13X-1, 75–76	102.95		5.93	49.4			
1257C-3R-2, 95–96	103.65		3.02	25.1			
1257B-8R-5, 60–61	104.47		5.79	48.2			
1257A-13X-3, 75–76	105.95	6.50	6.49	54.1	0.01	0.03	0.3
1257C-3R-4, 95–96	106.65		5.14	42.8			
1257B-9R-1, 64–65	108.24		5.85	48.7			
1257A-13X-5, 68–69	108.88		3.17	26.4			
1257C-3R-6, 95–96	109.65		5.65	47.1			
1257B-9R-3, 64–65	111.26		6.09	50.7			
1257A-14X-1, 74–75	112.54		5.57	46.4			

Table T16 (continued).

Hole, core, section, interval (cm)	Depth (mbsf)	TC (wt%)	IC (wt%)	$CaCO_3$ (wt%)	TOC (wt%)	N (wt%)	C/N (atomic)
1257B-9R-5, 64–65	114.26	5.53	5.43	45.2	0.10	0.01	14.0
1257A-14X-3, 69–70	115.49	5.57	5.49	45.7	0.08	0.05	1.8
1257B-9R-7, 49–50	117.11		4.68	39.0			
1257B-10R-1, 40–41	117.60		4.49	37.4			
1257A-14X-5, 69–70	118.49		4.59	38.2			
1257B-10R-2, 37–38	119.07		3.37	28.1			
1257B-10R-3, 42–43	120.62	4.48	4.25	35.4	0.23	0.02	11.4
1257A-15X-1, 70–71	122.20		5.51	45.9			
1257B-10R-5, 40–41	123.60		5.41	45.1			
1257A-15X-3, 68–69	125.18	5.40	5.35	44.6	0.05	0.10	0.6
1257B-10R-7, 40–41	126.60		4.61	38.4			
1257B-11R-1, 59–60	127.39		5.07	42.2			
1257A-15X-5, 70–71	128.20		6.80	56.6			
1257B-11R-3, 60–61	130.40	3.37	3.27	27.3	0.10	0.02	7.2
1257C-6R-1, 69–69	130.79		5.00	41.6			
1257A-16X-1, 120–121	132.30		6.63	55.2			
1257B-11R-5, 59–60	133.39		4.82	40.2			
1257C-6R-3, 69–69	133.79		4.71	39.2			
1257A-16X-3, 120–121	135.30	3.49	3.40	28.3	0.09	0.04	2.3
1257A-16X-4, 14–15	135.74		4.23	35.2			
1257B-11R-7, 49–50	135.79		4.26	35.5			
1257C-6R-5, 69–69	136.79		4.35	36.3			
1257C-6R-7, 55–55	139.65		4.62	38.5			
1257A-17X-1, 60–63	141.30		8.79	73.2			
1257A-17X-3, 42–43	144.08	7.23	7.20	60.0	0.03	0.03	1.2
1257A-17X-3, 98–99	144.64		6.99	58.2			
1257C-7R-4, 145–147	144.95		9.97	83.1			
1257A-17X-5, 48–50	147.14		6.49	54.1			
1257A-18X-2, 41–42	152.21		7.93	66.1			
1257B-14R-1, 29–30	155.79	8.05	7.93	66.1	0.12		
1257A-18X-4, 126–127	156.02	4.96	4.92	41.0	0.04	0.02	2.9
1257A-18X-6, 123–124	158.99		5.90	49.1			
1257A-19X-1, 24–25	159.94	5.61	5.62	46.8	0.00	0.01	
1257A-19X-CC, 25–26	161.45	6.23	6.23	51.9	0.00	0.02	
1257A-20X-1, 95–97	170.35	1.95	1.95	16.2	0.00	0.01	
1257A-20X-2, 131–132	172.21	6.38	6.02	50.1	0.36	0.02	20.4
1257A-20X-3, 145–146	173.85	5.72	5.73	47.7	0.00	0.03	
Unit IV (laminated calcareous claystone):							
1257A-20X-5, 73–74	176.13	8.14	5.41	45.1	2.73	0.16	20.2
1257A-20X-6, 35–36	177.25	10.82	4.89	40.7	5.93	0.28	16.2
1257A-21X-1, 83–84	179.83	14.05	5.50	45.8	8.55	0.36	28.0
1257B-19R-1, 105–106	184.75	9.18	3.52	29.4	5.66	0.29	23.1
1257B-19R-2, 31–32	185.51	9.98	4.68	39.0	5.30	0.27	22.5
1257B-20R-1, 12–13	188.82	7.26	5.68	47.3	1.58	0.11	16.3
1257A-22X-1, 80–83	189.40	14.99	5.48	45.6	9.51	0.42	26.3
1257B-20R-1, 77–78	189.47	15.62	5.97	49.8	9.65	0.34	33.0
1257A-22X-2, 19–20	190.29	14.63	6.01	50.1	8.62	0.38	26.2
1257B-21R-1, 95–96	194.25	12.34	11.66	97.2	0.68	0.02	32.7
1257B-21R-2, 16–17	194.96	12.14	10.57	88.1	1.57	0.12	15.3
1257B-21R-2, 27–28	195.07	19.00	7.93	66.1	11.07	0.33	39.1
1257B-21R-2, 47–48	195.27	20.75	4.99	41.6	15.76	0.54	34.1
1257A-23X-1, 23–24	198.43	12.40	11.46	95.5	0.94	0.04	30.8
1257B-22R-1, 36–37	198.66	14.32	6.53	54.4	7.79	0.28	32.5
1257B-22R-1, 44–45	198.74	10.65	0.93	7.7	9.72	0.38	30.1
1257B-22R-1, 83–84	199.13	14.29	5.89	49.0	8.40	0.29	33.5
1257A-23X-3, 78–79	201.98	11.73	9.41	78.4	2.32	0.17	15.9
1257B-23R-1, 40–41	203.40	12.96	0.68	5.7	12.28	0.49	29.4
1257B-23R-1, 50–51	203.50	12.40	6.78	56.5	5.62	0.27	24.3
1257B-23R-2, 8–9	203.99	11.77	10.25	85.4	1.52	0.09	19.2
1257A-23X-5, 85–86	205.05	15.09	4.44	37.0	10.65	0.40	31.1
1257A-24X-1, 62–63	208.22	17.27	8.64	72.0	8.63	0.27	37.3
1257B-24R-1, 49–50	208.49	14.34	6.76	56.3	7.58	0.31	28.4
1257B-24R-2, 74–75	210.24	13.42	6.30	52.5	7.12	0.29	28.3
1257A-24X-3, 45–46	211.05	14.83	5.70	47.5	9.13	0.36	29.6
1257B-24R-4, 32–33	212.28	13.58	4.96	41.3	8.62	0.31	32.7
1257B-25R-1, 31–31	212.91	12.56	5.00	41.6	7.56	0.25	35.0
1257B-25R-1, 45–46	213.05	12.86	8.59	71.5	4.27	0.23	22.0
1257B-25R-1, 128–129	213.88	11.52	5.17	43.0	6.35	0.29	25.4
1257B-25R-2, 33–33	214.43	12.21	11.85	98.7	0.36		

Table T16 (continued).

Hole, core, section, interval (cm)	Depth (mbsf)	TC (wt%)	IC (wt%)	$CaCO_3$ (wt%)	TOC (wt%)	N (wt%)	C/N (atomic)
1257B-25R-2, 113–114	215.23	7.96	6.31	52.6	1.65	0.10	19.2
1257C-15R-1, 70–71	217.30	14.95	6.74	56.2	8.21	0.30	32.3
1257A-25X-1, 104–105	218.24	14.68	6.27	52.2	8.41	0.35	28.0
1257C-15R-3, 14–15	218.95	14.28	8.64	72.0	5.64	0.23	28.5
Unit V (silty calcareous siltstone):							
1257B-26R-1, 125–126	218.85	3.82	3.35	27.9	0.47	0.07	8.0
1257B-26R-2, 32–33	219.42	3.44	3.06	25.5	0.38	0.05	8.2
1257B-27R-3, 72–73	226.02	3.88	3.51	29.3	0.37	0.05	8.7
1257A-26X-2, 71–72	229.01	4.37	3.98	33.2	0.39	0.05	9.6
1257A-26X-4, 67–68	231.97	3.84	3.31	27.6	0.53	0.06	11.2
1257A-26X-6, 73–74	235.03	3.90	3.41	28.4	0.49	0.07	8.2
1257A-27X-1, 72–73	237.22	4.48	4.26	35.5	0.22	0.04	6.3
1257A-27X-3, 71–72	240.21	4.87	4.17	34.7	0.70	0.09	9.1
1257A-27X-5, 72–73	243.22	3.56	2.88	24.0	0.68	0.05	16.0
1257A-28X-1, 63–64	246.83	4.64	3.93	32.7	0.71	0.11	7.5
1257A-28X-4, 60–61	251.30	1.88	1.09	9.1	0.79	0.11	8.4
1257A-29X-1, 70–71	256.50	5.46	5.03	41.9	0.43	0.05	9.8
1257A-29X-3, 71–72	259.51	6.03	5.39	44.9	0.64	0.04	19.1
1257A-29X-5, 71–72	262.51	4.67	4.01	33.4	0.66	0.10	7.8
1257A-30X-3, 32–33	268.72	5.54	4.83	40.2	0.71	0.06	14.8
1257A-31X-1, 65–66	275.75	5.78	5.02	41.8	0.76	0.11	8.1

Notes: TC = total carbon, IC = inorganic carbon, TOC = total organic carbon. Atomic C/N ratios are calculated from concentrations of organic carbon and total nitrogen.

Table T17. Rock-Eval pyrolysis analyses of sediment samples, Site 1257.

Hole, core, section, interval (cm)	Depth (mbsf)	TOC (wt%)	T_{max} (°C)	S_1	S_2	S_3	HI	OI
207-								
Unit IV (laminated calcareous claystone):								
1257A-20X-5, 73–74	176.13	2.73	410	0.64	13.40	2.04	490	74
1257A-20X-6, 35–36	177.25	5.93	402	1.97	36.74	2.43	620	41
1257A-21X-1, 83–84	179.83	8.55	401	1.69	46.59	2.78	544	32
1257B-19R-1, 105–106	184.75	5.66	411	0.94	33.96	1.58	600	27
1257B-19R-2, 31–32	185.51	5.30	409	1.08	30.03	1.36	566	25
1257B-20R-1, 12–13	188.82	1.58	418	0.21	3.37	0.63	213	39
1257A-22X-1, 80–83	189.40	9.51	395	3.77	58.42	3.17	614	33
1257B-20R-1, 77–78	189.47	9.65	385	3.88	66.29	3.37	686	34
1257A-22X-2, 19–20	190.29	8.62	400	2.61	53.87	3.11	624	36
1257B-21R-1, 95–96	194.25	0.68	406	0.17	3.31	0.37	486	54
1257B-21R-2, 16–17	194.96	1.57	401	0.33	8.95	0.55	570	35
1257B-21R-2, 27–28	195.07	11.07	387	3.30	79.19	1.79	715	16
1257B-21R-2, 47–48	195.27	15.76	387	5.76	115.04	2.55	729	16
1257A-23X-1, 23–24	198.43	0.94	408	0.20	5.21	0.57	554	60
1257B-22R-1, 36–37	198.66	7.79	397	2.07	54.91	1.83	704	23
1257B-22R-1, 44–45	198.74	9.72	402	1.91	60.55	1.80	622	18
1257B-22R-1, 83–84	199.13	8.40	398	2.08	59.00	2.07	702	24
1257A-23X-3, 78–79	201.98	2.32	412	0.39	12.55	0.89	540	38
1257B-23R-1, 40–41	203.40	12.28	401	2.16	78.48	2.18	639	17
1257B-23R-1, 50–51	203.50	5.62	400	1.10	35.54	1.65	632	29
1257B-23R-2, 8–9	203.99	1.52	407	0.37	8.16	0.82	536	53
1257A-23X-5, 85–86	205.05	10.65	401	3.00	62.89	3.49	590	32
1257A-24X-1, 62–63	208.22	8.63	399	2.00	58.64	2.50	679	28
1257B-24R-1, 49–50	208.49	7.58	398	1.67	50.77	3.09	669	40
1257B-24R-2, 74–75	210.24	7.12	398	2.08	46.54	2.02	653	28
1257A-24X-3, 45–46	211.05	9.13	406	1.99	54.81	3.21	600	35
1257B-24R-4, 32–33	212.28	8.62	402	1.72	58.60	2.26	679	26
1257B-25R-1, 31–31	212.91	7.56	397	2.20	50.88	3.57	673	47
1257B-25R-1, 45–46	213.05	4.27	404	0.57	28.08	2.66	657	62
1257B-25R-1, 128–129	213.88	6.35	400	1.44	41.86	2.79	659	43
1257B-25R-2, 113–114	215.23	1.65	403	0.28	7.48	1.00	453	60
1257C-15R-1, 70–71	217.30	8.21	397	1.86	56.27	3.36	685	40
1257A-25X-1, 104–105	218.24	8.41	404	1.83	53.14	2.82	631	33
1257C-15R-3, 14–15	218.95	5.64	403	1.06	38.74	2.50	686	44
Unit V (silty calcareous siltstone):								
1257A-27X-5, 72–73	243.22	0.68	421	0.04	0.80	1.07	117	157
1257A-28X-4, 60–61	251.30	0.79	416	0.06	0.68	1.03	86	130
1257A-31X-1, 65–66	275.75	0.76	425	0.27	1.12	0.92	147	121

Notes: TOC = total organic carbon. HI = milligrams of hydrocarbon-like material (S_2) per gram of organic carbon, OI = milligrams of CO_2 (S_3) per gram of organic carbon. See **"Organic Geochemistry,"** p. 27, in the "Explanatory Notes" chapter for definitions of T_{max}, S_1, S_2, and S_3.

Table T18. Headspace analyses of interstitial and microbial gases, Hole 1257A.

Core, section, interval (cm)	Depth (mbsf)	Routine safety monitoring				Microbial study					
		C_1 (ppmv)	C_2 (ppmv)	$C_{2=}$ (ppmv)	C_1/C_2	C_1 (ppmv)	C_2 (ppmv)	$C_{2=}$ (ppmv)	C_3 (ppmv)	$C_{3=}$ (ppmv)	C_1/C_2
207-1257A-											
Unit II (foraminifer- and silica-bearing nannofossil chalk):											
1H-2, 0–5	1.50	2	0	0		46	0	0	0	0	
2H-5, 0–5	8.60	3	0	0		6	0	0	0	0	
3H-5, 0–5	18.10	3	0	0		6	1	0	0	0	10
4H-4, 0–5	26.10	3	0	0		4	0	0	0	0	
5H-4, 0–5	35.60	2	0	0		6	0	0	0	0	
6X-3, 0–5	43.60	2	0	0		15	1	0	0	0	29
7X-4, 0–5	49.40	2	0	0		5	1	0	0	0	8
8X-4, 0–5	58.60	3	0	0		5	2	0	0	0	3
9X-3, 0–5	66.70	2	0	0		53	1	0	0	0	98
10X-3, 0–5	76.30	3	0	0		8	0	0	0	0	
Unit III (foraminifer-bearing nannofossil chalk):											
11X-2, 0–5	84.34	2	0	0		5	0	0	0	0	
12X-3, 0–5	95.60	5	0	0		8	1	0	0	0	
13X-4, 0–5	106.70	324	0	0		389	0	0	0	0	
14X-5, 0–5	117.80	2,498	1	0	2,082	1,990	1	0	0	0	1,951
15X-6, 0–5	129.00	3,378	2	0	2,252	3,976	2	0	0	0	2,455
16X-4, 0–5	135.60	8,296	3	0	2,440	2,897	1	0	0	0	2,195
17X-4, 0–5	145.16	4,999	3	0	2,000	5,511	2	0	0	0	2,325
18X-5, 0–5	156.26	11,227	5	0	2,245	5,130	3	0	0	0	1,865
19X-1, 0–5	159.70	4,841	3	0	1,936	1,575	1	0	0	0	1,175
Unit IV (laminated calcareous claystone):											
20X-5, 0–5	175.40	12,378	14	0	910	2,750	5	0	0	0	535
21X-1, 85–90	179.85	30,475	48	3	638	14,322	36	3	0	4	396
22X-2, 0–5	190.10	6,263	11	0	591	15,924	19	1	0	0	825
23X-4, 0–5	202.70	25,152	27	0	935	12,297	13	1	0	0	962
24X-2, 0–5	209.10	23,973	18	0	1,347	14,709	13	0	0	0	1,126
25X-1, 115–120	218.35	21,974	19	0	1,144	5,773	6	0	0	0	898
Unit V (silty calcareous siltstone):											
26X-4, 0–5	231.30	8,726	3	0	3,232	9,893	4	0	0	0	2,818
27X-4, 0–5	241.00	6,279	3	0	2,165	7,023	3	0	0	0	2,215
28X-3, 0–5	249.20	2,547	1	0	2,122	17	0	0	0	0	
29X-4, 0–5	260.30	4,300	3	0	1,720	6,172	3	0	0	0	1,810
30X-4, 0–5	269.90	3,933	3	0	1,356	5,704	5	1	4	0	1,103
31X-1, 66–71	275.76	1,473	2	0	866	NA					

Notes: C_1 = methane, C_2 = ethane, $C_{2=}$ = ethylene, C_3 = propane, $C_{3=}$ = propylene. NA = not analyzed.

Table T19. Interstitial water analyses, Site 1257.

Core, section, interval (cm)	Depth (mbsf)	Depth (mcd)	Salinity	Alkalinity (mM)	pH	Cl^- (mM)	$*SO_4^{2-}$ (mM)	NH_4^+ (μM)	$*H_4SiO_4$ (μM)	B (mM)	Li^+ (μM)	Sr^{2+} (μM)	Ca^{2+} (mM)	K^+ (mM)	Mg^{2+} (mM)	Ba^{2+} (μM)	Fe^{2+} (μM)	Mn^{2+} (μM)	Na^+ (mM)	Na^+ diff (mM)
207-1257A-																				
1H-1, 145–150	1.45	1.45	35.0	3.04	7.79	549	28.4	20	440	0.58	27	88	10.7	10.4	52.6	1.2	0.6	2.0	478	472
2H-4, 145–150	8.55	8.55	35.3	3.51	7.60	561	28.4	10	610	0.43	29	107	11.6	13.3	52.6	0.5	0.7	2.1	509	479
3H-4, 145–150	18.05	18.05	35.8	3.73	7.59	566	26.5	55	770	0.43	34	134	12.6	13.4	52.0	8.3	2.8	2.2	511	480
4H-3, 145–150	26.05	26.05	35.8	3.75	7.35	563	25.7	75	780	0.43	36	157	12.9	13.0	51.1	0.3	1.2	2.0	509	476
5H-3, 145–150	35.55	35.55	36.2	3.91	7.38	567	24.2	115	890	0.44	40	188	13.1	12.6	49.8	0.6	4.7	2.0	507	481
6X-3, 145–150	45.05	45.05	36.5	4.63	7.37	577	24.2	165	915	0.41	43	217	14.2	11.2	50.4	1.0	1.8	6.7	515	489
7X-3, 145–150	49.35	49.35	37.0	4.43	7.19	587	24.7	135	865	0.41	43	213	14.2	11.4	51.0	2.6	(72.1)	2.6	531	499
8X-3, 145–150	58.55	58.55	37.0	4.93	7.35	596	24.1	170	1090	0.40	47	256	14.4	11.1	49.5	0.4	7.2	1.3	527	510
14X-4, 140–150	117.70	117.70	38.0	4.34	7.26	659	9.8	420	700	0.41	66	507	14.7	11.2	45.7	1.5	2.4	2.2	569	549
15X-5, 140–150	128.90	128.49	39.0	4.31	7.32	672	7.6	460	625	0.47	73	573	14.9	10.7	43.3	1.7	1.3	1.9	563	562
18X-4, 140–150	156.16	161.96	40.5	6.05	7.15	705	1.6	480	775	0.72	98	802	18.1	8.8	43.5	7.6	(9.7)	9.1	585	580
31X-1, 71–81	275.81	281.61	42.0	ND	ND	749	4.4	775	95	0.20	107	1102	20.0	6.4	41.4	3.2	0.7	3.1	617	ND
207-1257B-																				
3R-2, 145–150	52.75	56.12	36.0	3.63	7.47	607	22.7	145	775	0.41	47	237	12.9	11.0	49.1	7.6	1.9	3.6	514	520
4R-3, 143–150	63.82	70.93	36.0	3.19	7.54	607	22.6	225	730	0.39	47	272	13.1	12.4	49.7	7.2	4.1	1.6	519	517
5R-4, 42–49	73.65	76.70	37.0	3.08	7.46	619	19.4	275	650	0.38	51	322	13.3	12.7	50.3	7.6	3.5	1.8	540	520
7R-2, 143–150	91.23	95.60	38.0	4.17	7.40	645	12.8	340	830	0.39	61	420	13.3	11.1	45.8	7.7	1.4	3.9	529	544
8R-4, 142–150	103.79	107.22	37.5	1.96	7.70	641	10.8	470	715	0.37	62	431	12.4	11.4	46.5	7.6	1.4	1.8	543	535
9R-3, 140–150	112.02	113.79	38.0	2.25	7.39	640	10.1	450	545	0.38	65	466	13.2	10.9	43.6	7.9	1.3	1.9	551	537
10R-4, 140–150	123.10	125.68	38.3	3.17	7.43	663	7.5	365	465	0.39	73	556	14.4	10.4	43.1	8.6	2.0	4.1	565	554
11R-4, 140–150	132.70	135.28	39.7	2.70	7.45	668	6.0	410	610	0.40	77	632	15.1	9.2	43.5	7.9	1.0	2.3	566	554
12R-3, 140–150	140.60	143.27	39.7	4.49	7.20	688	5.0	515	795	0.53	84	664	16.1	9.7	42.6	8.7	1.1	2.4	581	574
13R-4, 140–150	151.70	154.90	40.5	4.07	7.17	727	1.7	475	590	0.60	101	796	17.3	9.6	40.4	10.5	1.2	1.3	603	608
27R-3, 0–7	225.30	228.94	44.0	4.57	7.24	750	1.5	655	215	0.64	126	1041	21.8	6.3	39.4	13.9	1.7	1.6	608	626
207-1257C-																				
8R-6, 90–100	157.50	159.95	42.0	4.98	7.17	748	0.8	640	635	0.59	106	807	17.5	9.6	39.9	14.2	9.8	1.5	621	628
9R-6, 51–61	166.15	168.56	42.7	ND	ND	752	0.3	640	674	ND	ND	ND	18.7	9.2	39.6	ND	ND	ND	627	ND
10R-1, 140–150	169.80	172.21	43.0	5.11	7.13	769	0.5	590	790	0.70	122	841	19.6	9.1	39.5	158.9	17.8	1.1	620	646
12R-2, 90–100	190.10	192.65	44.3	3.75	7.07	772	3.2	905	665	0.88	138	948	23.5	9.1	37.6	40.3	1.6	0.9	634	648
13R-2, 140–150	200.20	202.75	46.5	4.82	6.89	823	0.2	900	675	0.82	157	1152	25.3	9.3	36.2	107.9	34.9	0.9	676	693
15R-3, 17–27	218.98	221.53	45.5	4.19	7.04	812	0.4	940	485	0.70	143	1132	23.8	8.2	39.8	51.4	4.7	0.8	660	679
16R-6, 20–30	233.87	235.03	44.0	ND	ND	748	1.6	575	180	0.50	126	1106	21.3	6.3	42.2	12.2	2.1	1.8	618	ND

Notes: * = ICP-AES. ND = not determined. Values in parentheses are regarded as doubtful.

Table T20. Index properties of discrete samples, Site 1257. (See table note. Continued on next two pages.)

Core, section, interval (cm)	Depth (mbsf)	Depth (mcd)	Water content (%) Wet	Water content (%) Dry	Density (g/cm^3) Bulk	Density (g/cm^3) Dry	Density (g/cm^3) Grain	Porosity (%)	Void ratio
207-1257A-									
1H-1, 70–72	0.70	0.70	42.2	73.0	1.589	0.918	2.660	65.5	1.896
1H-2, 45–47	1.95	1.95	43.6	77.4	1.574	0.887	2.693	67.1	2.035
2H-1, 74–76	3.34	3.34	43.6	77.2	1.573	0.888	2.684	66.9	2.024
2H-2, 74–76	4.84	4.84	41.7	71.6	1.578	0.920	2.577	64.3	1.801
2H-3, 70–72	6.30	6.30	41.9	72.0	1.595	0.928	2.666	65.2	1.875
2H-4, 70–72	7.80	7.80	41.0	69.4	1.602	0.946	2.634	64.1	1.786
2H-5, 70–72	9.30	9.30	44.7	80.8	1.550	0.857	2.647	67.6	2.088
2H-6, 68–70	10.78	10.78	38.5	62.5	1.651	1.016	2.675	62.0	1.633
2H-7, 30–32	11.90	11.90	44.8	81.3	1.552	0.856	2.670	68.0	2.121
3H-1, 70–72	12.80	12.80	42.2	72.9	1.593	0.921	2.677	65.6	1.906
3H-2, 70–72	14.30	14.30	40.8	68.9	1.605	0.951	2.636	63.9	1.773
3H-3, 70–72	15.80	15.80	41.8	71.9	1.588	0.924	2.628	64.9	1.845
3H-4, 70–72	17.30	17.30	40.2	67.1	1.615	0.966	2.637	63.3	1.728
3H-5, 70–72	18.80	18.80	43.4	76.6	1.549	0.878	2.552	65.6	1.908
3H-6, 70–72	20.30	20.30	40.5	68.1	1.624	0.966	2.703	64.3	1.799
3H-7, 40–42	21.50	21.50	41.4	70.7	1.597	0.935	2.643	64.6	1.826
4H-1, 70–72	22.30	22.30	42.0	72.5	1.590	0.922	2.654	65.2	1.878
4H-2, 70–72	23.80	23.80	41.0	69.4	1.610	0.951	2.670	64.4	1.808
4H-3, 70–72	25.30	25.30	42.6	74.1	1.562	0.897	2.560	64.9	1.853
4H-4, 70–72	26.80	26.80	40.0	66.7	1.622	0.973	2.656	63.4	1.729
4H-5, 70–72	28.10	28.10	38.9	63.6	1.651	1.010	2.705	62.7	1.679
4H-6, 70–72	29.60	29.60	39.6	65.6	1.626	0.982	2.645	62.9	1.693
4H-7, 60–62	31.00	31.00	39.6	65.5	1.629	0.984	2.660	63.0	1.702
5H-1, 80–82	31.90	31.90	39.7	65.8	1.628	0.982	2.658	63.1	1.708
5H-2, 70–72	33.30	33.30	41.0	69.5	1.614	0.952	2.693	64.6	1.828
5H-3, 70–72	34.80	34.80	38.7	63.1	1.632	1.001	2.611	61.7	1.609
5H-4, 70–72	36.30	36.30	39.2	64.5	1.639	0.996	2.675	62.8	1.686
5H-5, 90–92	38.00	38.00	39.2	64.6	1.628	0.989	2.630	62.4	1.659
5H-6, 55–57	39.15	39.15	35.6	55.3	1.688	1.086	2.631	58.7	1.422
6X-1, 26–28	40.86	40.86	41.4	70.6	1.628	0.954	2.789	65.8	1.924
6X-2, 56–58	42.66	42.66	42.3	73.3	1.615	0.932	2.801	66.7	2.005
6X-3, 45–47	44.05	44.05	43.7	77.6	1.554	0.875	2.599	66.3	1.971
6X-4, 46–48	45.56	45.56	43.1	75.8	1.580	0.899	2.684	66.5	1.988
7X-1, 54–56	45.44	45.44	39.7	65.9	1.671	1.007	2.861	64.8	1.840
7X-2, 104–106	47.44	47.44	44.8	81.3	1.566	0.864	2.751	68.6	2.183
7X-3, 54–56	48.44	48.44	46.2	85.8	1.516	0.816	2.581	68.4	2.163
7X-4, 46–48	49.86	49.86	42.9	75.0	1.621	0.926	2.881	67.9	2.111
7X-5, 41–43	51.31	51.31	45.7	84.3	1.516	0.823	2.549	67.7	2.099
8X-1, 117–119	55.27	55.27	44.3	79.5	1.543	0.860	2.585	66.7	2.006
8X-2, 67–69	56.27	56.27	44.4	80.0	1.521	0.845	2.485	66.0	1.941
8X-3, 69–71	57.79	57.79	43.2	76.0	1.577	0.896	2.675	66.5	1.985
8X-4, 78–80	59.38	59.38	45.2	82.4	1.543	0.846	2.651	68.1	2.133
8X-5, 103–105	61.13	61.13	47.7	91.0	1.491	0.780	2.549	69.4	2.266
9X-1, 70–72	64.40	64.40	36.9	58.4	1.677	1.059	2.672	60.4	1.524
9X-2, 103–105	66.23	66.23	41.0	69.4	1.586	0.936	2.564	63.5	1.739
9X-3, 88–90	67.58	67.58	42.6	74.1	1.560	0.896	2.548	64.8	1.844
9X-4, 52–54	68.72	68.72	36.2	56.8	1.673	1.067	2.613	59.2	1.449
9X-5, 60–62	69.80	69.80	29.7	42.2	1.797	1.264	2.638	52.1	1.087
10X-1, 62–64	73.92	73.92	30.1	43.0	1.749	1.223	2.513	51.3	1.055
10X-2, 70–72	75.50	75.50	36.9	58.6	1.625	1.025	2.477	58.6	1.416
10X-3, 70–72	77.00	77.00	36.6	57.6	1.659	1.052	2.582	59.2	1.454
10X-4, 70–72	78.50	78.50	40.7	68.7	1.594	0.944	2.580	63.4	1.731
10X-5, 70–72	80.00	80.00	42.4	73.5	1.564	0.901	2.554	64.7	1.834
10X-6, 60–62	80.90	80.90	38.7	63.0	1.613	0.989	2.529	60.9	1.557
11X-1, 63–65	83.63	83.63	40.7	68.7	1.643	0.974	2.808	65.3	1.884
11X-2, 25–27	84.59	84.59	43.3	76.4	1.588	0.901	2.742	67.2	2.045
12X-1, 70–72	93.30	93.30	39.4	65.0	1.642	0.995	2.699	63.1	1.712
12X-2, 70–72	94.80	94.80	39.7	65.9	1.626	0.980	2.653	63.1	1.708
12X-3, 69–71	96.29	96.29	38.2	61.9	1.652	1.020	2.663	61.7	1.610
12X-CC, 22–24	98.07	98.07	33.2	49.6	1.756	1.173	2.721	56.9	1.319
13X-1, 76–78	102.96	102.96	38.0	61.2	1.678	1.041	2.753	62.2	1.645
13X-2, 66–68	104.36	104.36	31.4	45.8	1.793	1.229	2.733	55.0	1.223
13X-3, 76–78	105.96	105.96	37.0	58.8	1.659	1.045	2.612	60.0	1.501
13X-4, 70–72	107.40	107.40	28.5	39.9	1.818	1.299	2.635	50.7	1.028
13X-5, 70–72	108.90	108.90	35.2	54.3	1.688	1.094	2.607	58.0	1.382
13X-6, 70–72	110.40	110.40	26.8	36.6	1.875	1.373	2.695	49.1	0.963

Table T20 (continued).

Core, section, interval (cm)	Depth (mbsf)	Depth (mcd)	Water content (%) Wet	Water content (%) Dry	Density (g/cm³) Bulk	Density (g/cm³) Dry	Density (g/cm³) Grain	Porosity (%)	Void ratio
13X-7, 35–37	111.25	111.25	29.6	42.1	1.811	1.275	2.678	52.4	1.101
14X-1, 75–77	112.55	112.55	35.4	54.7	1.703	1.100	2.671	58.8	1.427
14X-2, 70–72	114.00	114.00	31.5	46.0	1.765	1.209	2.644	54.3	1.187
14X-3, 70–72	115.50	115.50	31.9	46.8	1.746	1.190	2.605	54.3	1.190
14X-4, 70–72	117.00	117.00	31.7	46.4	1.755	1.199	2.624	54.3	1.189
14X-5, 70–72	118.50	118.50	30.6	44.0	1.814	1.259	2.747	54.2	1.182
14X-6, 68–70	119.98	119.98	30.2	43.3	1.790	1.249	2.645	52.8	1.117
15X-1, 70–72	122.20	121.79	28.5	39.8	1.816	1.298	2.624	50.5	1.021
15X-2, 67–69	123.67	123.26	29.3	41.5	1.773	1.253	2.545	50.8	1.032
15X-3, 68–70	125.18	124.77	31.3	45.5	1.768	1.215	2.641	54.0	1.173
15X-4, 70–72	126.70	126.29	25.9	34.9	1.881	1.395	2.657	47.5	0.905
15X-5, 81–83	128.31	127.90	32.6	48.3	1.714	1.156	2.541	54.5	1.198
15X-6, 72–74	129.72	129.31	26.4	35.8	1.876	1.381	2.673	48.3	0.935
15X-7, 24–26	130.74	130.33	28.9	40.6	1.814	1.290	2.641	51.2	1.048
16X-1, 73–75	131.83	135.46	26.7	36.4	1.848	1.356	2.613	48.1	0.928
16X-2, 75–77	133.35	136.98	27.4	37.7	1.834	1.332	2.612	49.0	0.961
16X-3, 71–73	134.81	138.44	31.7	46.3	1.764	1.206	2.653	54.5	1.200
16X-4, 75–77	136.35	139.98	27.0	37.0	1.873	1.368	2.700	49.4	0.974
16X-5, 46–48	137.56	141.19	28.6	40.1	1.794	1.280	2.569	50.2	1.006
17X-1, 58–60	141.28	146.75	34.4	52.3	1.739	1.141	2.741	58.3	1.401
17X-2, 48–50	142.64	148.11	34.5	52.7	1.710	1.120	2.642	57.6	1.360
17X-3, 43–45	144.09	149.56	30.2	43.2	1.785	1.247	2.628	52.6	1.108
17X-4, 80–82	145.96	151.43	30.2	43.2	1.790	1.251	2.645	52.7	1.115
17X-5, 52–54	147.18	152.65	29.8	42.5	1.758	1.234	2.530	51.2	1.051
17X-6, 24–26	148.10	153.57	29.3	41.4	1.794	1.268	2.604	51.3	1.053
18X-1, 42–44	150.72	156.52	28.0	38.9	1.831	1.318	2.639	50.0	1.002
18X-2, 86–88	152.66	158.46	30.1	43.1	1.775	1.241	2.596	52.2	1.092
18X-3, 54–56	153.84	159.64	29.6	42.1	1.788	1.258	2.607	51.7	1.072
18X-4, 60–62	155.36	161.16	27.1	37.1	1.814	1.323	2.542	48.0	0.922
18X-5, 53–55	156.79	162.59	29.4	41.6	1.759	1.243	2.508	50.4	1.018
18X-6, 70–72	158.46	164.26	26.5	36.0	1.837	1.351	2.572	47.5	0.905
19X-1, 100–102	160.70	166.50	31.2	45.4	1.739	1.196	2.548	53.0	1.129
20X-1, 50–52	169.90	175.70	29.7	42.3	1.757	1.234	2.520	51.0	1.042
20X-2, 60–62	171.50	177.30	25.2	33.7	1.876	1.403	2.606	46.2	0.858
20X-3, 77–79	173.17	178.97	21.7	27.7	1.974	1.546	2.657	41.8	0.719
26X-1, 70–72	227.50	233.30	17.6	21.4	2.120	1.746	2.750	36.5	0.575
26X-2, 73–75	229.03	234.83	18.2	22.2	2.114	1.729	2.769	37.6	0.601
26X-3, 72–74	230.52	236.32	22.5	29.1	1.988	1.540	2.739	43.8	0.778
26X-4, 70–72	232.00	237.80	17.5	21.1	2.086	1.722	2.673	35.6	0.552
26X-5, 70–72	233.50	239.30	17.8	21.6	2.083	1.712	2.683	36.2	0.567
26X-6, 70–72	235.00	240.80	19.2	23.7	2.060	1.666	2.711	38.6	0.628
26X-7, 22–25	236.02	241.82	16.0	19.1	2.138	1.796	2.698	33.4	0.502
27X-1, 72–74	237.22	243.02	16.5	19.7	2.124	1.775	2.695	34.2	0.519
27X-2, 69–72	238.69	244.49	16.7	20.0	2.106	1.755	2.671	34.3	0.522
27X-3, 71–73	240.21	246.01	16.3	19.5	2.113	1.768	2.667	33.7	0.508
27X-4, 66–68	241.66	247.46	15.6	18.4	2.154	1.819	2.703	32.7	0.486
27X-5, 70–72	243.20	249.00	14.5	17.0	2.188	1.870	2.713	31.0	0.450
28X-1, 72–74	246.92	252.72	15.1	17.8	2.221	1.886	2.805	32.8	0.487
28X-2, 70–72	248.40	254.20	13.4	15.5	2.215	1.918	2.703	29.0	0.409
28X-3, 70–72	249.90	255.70	16.0	19.1	2.144	1.801	2.709	33.5	0.504
28X-4, 71–73	251.41	257.21	17.5	21.1	2.106	1.739	2.712	35.9	0.560
29X-1, 69–71	256.49	262.29	14.5	17.0	2.197	1.878	2.726	31.1	0.452
29X-2, 69–71	257.99	263.79	15.7	18.7	2.153	1.815	2.710	33.1	0.494
29X-3, 70–72	259.50	265.30	14.2	16.6	2.151	1.844	2.632	29.9	0.427
29X-4, 71–73	261.01	266.81	16.0	19.1	2.139	1.797	2.700	33.5	0.503
29X-5, 70–72	262.50	268.30	17.0	20.4	2.104	1.747	2.682	34.9	0.535
29X-6, 70–72	264.00	269.80	15.0	17.7	2.172	1.846	2.708	31.8	0.467
30X-1, 71–73	266.11	271.91	12.9	14.7	2.222	1.937	2.686	27.9	0.387
30X-2, 70–72	267.60	273.40	14.5	17.0	2.186	1.869	2.707	31.0	0.448
30X-3, 70–72	269.10	274.90	15.5	18.4	2.160	1.825	2.713	32.7	0.487
30X-4, 71–73	270.61	276.41	14.5	17.0	2.216	1.894	2.764	31.5	0.459
30X-5, 70–72	272.10	277.90	15.0	17.7	2.194	1.864	2.749	32.2	0.475
30X-6, 71–73	273.61	279.41	17.1	20.6	2.113	1.752	2.706	35.3	0.545
31X-1, 32–34	275.42	281.22	14.1	16.5	2.177	1.869	2.673	30.1	0.430
207-1257B-									
1R-2, 75–77	42.25	43.62	39.8	66.2	1.638	0.985	2.715	63.7	1.756
2R-2, 90–92	47.20	50.57	43.9	78.3	1.561	0.875	2.648	66.9	2.025
3R-1, 73–75	50.53	53.90	40.5	68.0	1.616	0.962	2.665	63.9	1.770

Table T20 (continued).

Core, section, interval (cm)	Depth (mbsf)	Depth (mcd)	Water content (%) Wet	Water content (%) Dry	Density (g/cm³) Bulk	Density (g/cm³) Dry	Density (g/cm³) Grain	Porosity (%)	Void ratio
4R-2, 110–112	61.99	69.10	37.1	59.1	1.670	1.049	2.661	60.6	1.536
4R-4, 84–86	64.73	71.84	29.2	41.3	1.794	1.270	2.602	51.2	1.049
5R-3, 80–82	72.55	75.60	30.2	43.3	1.782	1.243	2.622	52.6	1.109
10R-1, 90–92	118.10	120.68	26.5	36.1	1.877	1.379	2.685	48.6	0.947
11R-1, 78–80	127.58	130.16	27.9	38.7	1.839	1.326	2.658	50.1	1.005
12R-3, 65–67	139.85	142.52	29.7	42.3	1.835	1.290	2.758	53.2	1.138
13R-3, 28–30	149.08	152.28	20.3	25.4	2.055	1.639	2.761	40.6	0.685
19R-1, 60–62	184.30	187.50	40.4	67.6	1.507	0.899	2.212	59.4	1.461
21R-2, 55–57	195.35	201.48	41.2	70.0	1.543	0.908	2.393	62.0	1.635
26R-1, 67–69	218.27	221.91	22.4	28.9	2.020	1.566	2.811	44.3	0.795
27R-3, 40–42	225.70	229.34	20.3	25.5	2.093	1.668	2.854	41.6	0.711
207-1257C-									
3R-1, 70–72	101.90	103.90	28.4	39.7	1.810	1.295	2.602	50.2	1.009
3R-2, 77–79	103.47	105.47	30.4	43.7	1.812	1.261	2.731	53.8	1.166
3R-3, 77–79	104.97	106.97	28.2	39.4	1.799	1.291	2.563	49.6	0.986
3R-4, 74–76	106.44	108.44	28.9	40.7	1.814	1.290	2.644	51.2	1.050
3R-5, 74–76	107.94	109.94	31.0	45.0	1.775	1.224	2.649	53.8	1.164
3R-6, 72–74	109.42	111.42	33.2	49.8	1.764	1.178	2.753	57.2	1.338
3R-7, 21–23	110.11	112.11	31.6	46.2	1.764	1.207	2.646	54.4	1.193
4R-1, 71–73	111.51	113.91	28.5	39.8	1.863	1.332	2.765	51.8	1.076
4R-2, 70–72	113.00	115.40	27.2	37.4	1.863	1.356	2.687	49.5	0.981
4R-3, 73–75	114.53	116.93	29.8	42.4	1.795	1.260	2.636	52.2	1.091
4R-4, 70–72	116.00	118.40	30.0	43.0	1.824	1.276	2.745	53.5	1.151
4R-5, 70–72	117.50	119.90	28.7	40.2	1.822	1.300	2.651	51.0	1.040
4R-6, 70–72	119.00	121.40	27.0	37.0	1.868	1.363	2.690	49.3	0.973
4R-7, 25–27	120.05	122.45	29.6	42.0	1.816	1.279	2.689	52.4	1.103
5R-1, 70–72	121.20	123.87	27.9	38.7	1.853	1.336	2.697	50.5	1.019
5R-2, 74–76	122.74	125.41	27.1	37.1	1.853	1.351	2.650	49.0	0.961
5R-3, 70–72	124.20	126.87	27.2	37.3	1.906	1.388	2.808	50.6	1.023
5R-4, 70–72	125.70	128.37	29.0	40.8	1.810	1.286	2.637	51.2	1.051
5R-5, 40–42	126.70	129.37	27.0	36.9	1.845	1.348	2.622	48.6	0.946
6R-1, 70–72	130.80	132.00	28.3	39.5	1.823	1.307	2.636	50.4	1.017
6R-2, 70–72	132.30	133.50	28.5	39.9	1.812	1.295	2.617	50.5	1.021
6R-3, 70–72	133.80	135.00	30.0	42.9	1.800	1.260	2.667	52.7	1.116
6R-4, 70–72	135.30	136.50	29.7	42.2	1.799	1.265	2.643	52.1	1.090
6R-5, 70–72	136.80	138.00	28.4	39.7	1.818	1.301	2.628	50.5	1.020
8R-2, 70–72	151.30	153.75	30.6	44.2	1.820	1.263	2.774	54.5	1.197
8R-3, 70–72	152.80	155.25	21.8	27.9	2.010	1.571	2.749	42.9	0.750
8R-4, 70–72	154.30	156.75	24.6	32.5	1.917	1.446	2.676	46.0	0.851
8R-5, 70–72	155.80	158.25	24.9	33.1	1.924	1.445	2.715	46.8	0.879
9R-1, 70–72	159.40	161.81	23.7	31.1	1.942	1.481	2.693	45.0	0.819
9R-2, 70–72	160.90	163.31	32.0	47.1	1.752	1.191	2.633	54.8	1.211
9R-3, 40–42	162.10	164.51	24.0	31.5	1.908	1.451	2.622	44.7	0.807
9R-4, 12–14	163.32	165.73	30.9	44.8	1.822	1.258	2.797	55.0	1.223
10R-1, 56–58	168.96	171.37	28.1	39.0	1.833	1.319	2.652	50.3	1.011
10R-2, 56–58	170.46	172.87	28.1	39.1	1.859	1.337	2.727	51.0	1.040
12R-2, 28–30	189.48	192.03	43.0	75.6	1.540	0.877	2.486	64.7	1.835
13R-1, 60–62	197.90	200.45	39.7	65.9	1.768	1.065	3.393	68.6	2.185
15R-1, 106–108	217.66	220.21	41.8	71.9	1.598	0.930	2.677	65.3	1.879
16R-1, 47–49	226.67	227.83	20.6	25.9	2.049	1.628	2.768	41.2	0.701
16R-2, 57–59	228.27	229.43	21.3	27.1	2.057	1.618	2.832	42.9	0.750
16R-3, 72–74	229.92	231.08	21.9	28.0	2.044	1.596	2.834	43.7	0.776
16R-4, 85–87	231.55	232.71	18.2	22.2	2.112	1.727	2.764	37.5	0.600
16R-6, 50–52	234.17	235.33	20.3	25.5	2.049	1.632	2.753	40.7	0.687

Note: This table is also available in **ASCII.**

Table T21. Discrete measurements of *P*-wave velocity, Site 1257.

Core, section, interval (cm)	Depth (mbsf)	Depth (mcd)	Velocity (m/s) x	Velocity (m/s) y	Velocity (m/s) z
207-1257A-					
1H-1, 41	0.41	0.41	1527.9		
1H-1, 129	1.29	1.29	1544.9		
1H-2, 23.2	1.73	1.73	1550.9		
1H-2, 62	2.12	2.12	1559.5		
2H-1, 20.1	2.8	2.8	1580.7		
2H-1, 60.1	3.2	3.2	1571.9		
2H-1, 122.5	3.83	3.83	1576.0		
2H-2, 29.3	4.39	4.39	1610.8		
2H-2, 120.7	5.31	5.31	1569.0		
2H-3, 30	5.9	5.9	1582.9		
2H-3, 124	6.84	6.84	1569.1		
2H-4, 22.1	7.32	7.32	1582.9		
2H-4, 120.2	8.3	8.3	1584.1		
2H-5, 21.3	8.81	8.81	1584.0		
2H-5, 120	9.8	9.8	1609.7		
2H-6, 20.1	10.3	10.3	1595.8		
2H-6, 123.3	11.33	11.33	1587.9		
2H-7, 22.5	11.82	11.82	1567.1		
3H-1, 13.4	12.23	12.23	1639.0		
3H-1, 56.3	12.66	12.66	1598.8		
3H-1, 121	13.31	13.31	1603.8		
3H-2, 15.1	13.75	13.75	1594.2		
3H-2, 56	14.16	14.16	1610.2		
3H-2, 121.3	14.81	14.81	1592.0		
3H-3, 16	15.26	15.26	1566.8		
3H-3, 56	15.66	15.66	1590.2		
3H-3, 121	16.31	16.31	1595.9		
3H-4, 17.2	16.77	16.77	1613.0		
3H-4, 55	17.15	17.15	1642.0		
3H-4, 120.3	17.8	17.8	1571.3		
3H-5, 13.9	18.24	18.24	1565.1		
3H-5, 51.9	18.62	18.62	1605.6		
3H-5, 119.9	19.3	19.3	1622.1		
3H-6, 15.2	19.75	19.75	1580.1		
3H-6, 56.3	20.16	20.16	1630.3		
3H-6, 120.1	20.8	20.8	1588.9		
3H-7, 10.6	21.21	21.21	1595.6		
3H-7, 48.1	21.58	21.58	1587.7		
4H-1, 48.5	22.08	22.08	1598.3		
4H-1, 79.1	22.39	22.39	1606.8		
4H-1, 131.6	22.92	22.92	1621.9		
4H-2, 63.5	23.74	23.74	1622.3		
4H-2, 103.5	24.14	24.14	1582.6		
4H-2, 141.1	24.51	24.51	1603.2		
4H-3, 24.6	24.85	24.85	1590.4		
4H-3, 64.4	25.24	25.24	1557.3		
4H-3, 111.5	25.72	25.72	1599.1		
4H-4, 120.9	27.31	27.31	1622.9		
4H-5, 21.2	27.61	27.61	1641.8		
4H-5, 63.8	28.04	28.04	1644.7		
4H-5, 141.4	28.81	28.81	1651.8		
4H-6, 12.1	29.02	29.02	1690.4		
4H-6, 145.6	30.36	30.36	1685.5		
4H-7, 77.3	31.17	31.17	1663.6		
5H-1, 16.8	31.27	31.27	1605.0		
5H-1, 140	32.5	32.5	1593.9		
5H-2, 83.6	33.44	33.44	1611.7		
5H-3, 64.7	34.75	34.75	1632.6		
5H-3, 106.5	35.17	35.17	1587.3		
5H-4, 22	35.82	35.82	1631.8		
5H-4, 66.8	36.27	36.27	1618.3		
5H-4, 111.8	36.72	36.72	1630.7		
5H-5, 42.9	37.53	37.53	1618.9		
5H-5, 71.4	37.81	37.81	1576.6		
5H-5, 97.2	38.07	38.07	1628.3		
5H-5, 134.6	38.45	38.45	1580.4		
5H-6, 13.2	38.73	38.73	1648.5		
5H-6, 44.6	39.05	39.05	1633.4		
5H-6, 84.1	39.44	39.44	1628.5		
6X-1, 102	41.62	41.62	1684.0		
6X-2, 54	42.64	42.64	1684.7		
6X-3, 8	43.68	43.68	1724.8		
6X-3, 54	44.14	44.14	1689.8		
6X-3, 110	44.7	44.7	1705.2		
6X-4, 110	46.2	46.2	1716.6		
7X-1, 50	45.4	45.4	1660.2		
7X-1, 116	46.06	46.06	1575.3		
7X-2, 72.2	47.12	47.12	1654.9		
7X-2, 107.2	47.47	47.47	1615.7		
7X-2, 136.2	47.76	47.76	1605.2		
7X-3, 8.1	47.98	47.98	1654.3		
7X-3, 50	48.4	48.4	1689.5		
7X-3, 84.8	48.75	48.75	1679.4		
7X-3, 119.6	49.1	49.1	1693.1		
7X-4, 26.1	49.66	49.66	1641.5		
7X-4, 87.6	50.28	50.28	1668.8		
7X-4, 122.5	50.62	50.62	1675.0		
7X-5, 23	51.13	51.13	1653.6		
7X-5, 64.5	51.54	51.54	1657.7		
8X-1, 11	54.21	54.21	1654.9		
8X-1, 33.8	54.44	54.44	1622.0		
8X-1, 120.5	55.31	55.31	1696.5		
8X-2, 34.1	55.94	55.94	1675.9		
8X-2, 90.2	56.5	56.5	1697.0		
8X-3, 6	57.16	57.16	1647.9		
8X-3, 35.5	57.46	57.46	1675.4		
8X-3, 83.7	57.94	57.94	1641.6		
8X-4, 63.8	59.24	59.24	1644.3		
8X-4, 96.5	59.56	59.56	1646.1		
8X-5, 23.7	60.34	60.34	1663.7		
8X-5, 136	61.46	61.46	1646.2		
9X-1, 10.4	63.8	63.8	1752.8		
9X-1, 37.5	64.07	64.07	1720.0		
9X-1, 78.4	64.48	64.48	1751.8		
9X-2, 11.3	65.31	65.31	1672.5		
9X-2, 71.6	65.92	65.92	1666.4		
9X-2, 106.6	66.27	66.27	1662.1		
9X-2, 135.6	66.56	66.56	1691.6		
9X-3, 8.7	66.79	66.79	1676.6		
9X-3, 99.4	67.69	67.69	1653.5		
9X-4, 42.7	68.63	68.63	1692.1		
9X-5, 42.1	69.62	69.62	1696.9		
9X-5, 65.4	69.85	69.85	2969.4		
9X-CC, 4.1	69.99	69.99	2719.5		
9X-CC, 6	70.01	70.01	3208.2		
9X-CC, 18.2	70.13	70.13	2494.3		
10X-1, 26.1	73.56	73.56	1857.6		
10X-1, 50.3	73.8	73.8	1678.4		
10X-2, 53	75.33	75.33	1841.1		
10X-2, 71.6	75.52	75.52	1849.6		
10X-2, 74.8	75.55	75.55	1644.1		
10X-2, 141.9	76.22	76.22	1750.2		
10X-3, 19.6	76.5	76.5	1629.1		
10X-3, 39.9	76.7	76.7	3609.6		
10X-3, 107	77.37	77.37	1607.1		
10X-4, 25.1	78.05	78.05	1621.8		
10X-4, 91.5	78.71	78.71	1602.9		
10X-5, 20.1	79.5	79.5	1592.4		
10X-5, 89.5	80.19	80.19	1652.7		

Note: Multiple axis measurements were performed on 2-cm^3 samples. X-direction is perpendicular to the surface of a split core, y-direction is parallel to the surface of a split core, and z-direction is perpendicular to the top of the core. Only a portion of this table appears here. The complete table is available in **ASCII.**

Table T22. Checkshot survey data, Site 1257.

Checkshot station	Depth (mbrf)	Depth (mbsf)	Traveltime (s one way)	Traveltime (sbsf 2 way)	Interval time (s)	RMS velocity (m/s)	Interval velocity (m/s)
Seafloor							
1	2962.3	0.0	1.973	0.000	1.973	1495.0	1495.0
2	3056.0	91.7	2.025	0.053	0.053	1746.5	1746.5
3	3066.0	101.7	2.031	0.059	0.006	1733.3	1616.4
4	3096.0	131.7	2.048	0.075	0.017	1749.4	1805.0
5	3126.0	161.7	2.064	0.091	0.016	1778.2	1910.9
6	3156.0	191.7	2.081	0.108	0.017	1773.6	1749.1
7	3186.0	221.7	2.097	0.125	0.017	1779.5	1817.7
8	3216.0	251.7	2.112	0.140	0.015	1804.1	1997.6
	3251.0	286.7	2.127	0.154	0.015	1857.5	2300.1

Notes: sbsf = seconds below seafloor. RMS = root mean square. Rig floor (including Kelly bushing) to sea level = 11.2 m. Air gun depth = 2 mbsl.